BERICHTE
aus dem
INSTITUT FÜR MEERESKUNDE
an der
CHRISTIAN-ALBRECHTS-UNIVERSITÄT · KIEL

Nr. 194

1990

INSTABILITIES AND MULTIPLE EQUILIBRIA OF THE THERMOHALINE CIRCULATION

von

Jochem Marotzke

Kopien dieser Arbeit können bezogen werden von:
Institut für Meereskunde an der Universität Kiel
Abt. Theoretische Ozeanographie
Düsternbrooker Weg 20
2300 Kiel 1 - FRG -

ISSN 0341 - 8561 -

Diese Arbeit wurde von der Mathematisch-
Naturwissenschaftlichen Fakultät der
Universität Kiel als Dissertation angenommen.

ZUSAMMENFASSUNG

Um die Ursachen interhemisphärischen Wärmetransports im Ozean zu verstehen, untersuche ich die Existenz mehrfacher Gleichgewichtszustände der thermohalinen Zirkulation sowie Instabilitäten, die zu Übergängen zwischen verschiedenen Gleichgewichten führen können. Es werden idealisierte Ozeanmodelle benutzt, dabei ist die entscheidende Eigenschaft aller Modelle die unterschiedliche Kopplung von Temperatur und Salzgehalt an die Atmosphäre.

In dem Boxmodell eines Ozeanbeckens bewirkt ein positiver Rückkopplungsmechanismus bei infinitesimalen Störungen den Übergang von einer bezüglich des Äquators symmetrischen Zirkulation zu interhemisphärischem Transport. Die Reaktion eines globalen Boxmodells auf Salzgehaltsstörungen endlicher Amplitude zeigt, daß die Zustände ohne Symmetrieeigenschaften bezüglich des Äquators bevorzugt eingenommen werden.

Das zweidimensionale Modell eines Ozeanbeckens geht ebenfalls unter sehr kleinen Salzgehaltsstörungen aus einem symmetrischen in einen unsymmetrischen Zustand über. Die Beseitigung statischer Instabilität durch Konvektion verstärkt die Sensitivität des Modells gegenüber Salzgehaltsstörungen beträchtlich.

Das dreidimensionale GFDL-Modell einer idealisierten Hemisphäre mit thermohalinem und Windantrieb hat zwei Gleichgewichtszustände, von denen einer stabil ist. Beide Zustände weisen polwärtige Oberflächenströmung und Absinken in hohen Breiten auf, aber Tiefenwasserbildung ist in dem stabilen Zustand auf kleinere Gebiete beschränkt. Ohne Windschub wurde kein stabiles Gleichgewicht gefunden, die meiste Zeit über befindet sich das Modell in einem Zustand mit Absinken in niederen Breiten und langsamer, im zonalen Mittel äquatorwärts gerichteter Oberflächenströmung.

Das globale GFDL-Modell in idealisierter Geometrie (zwei gleich große Ozeanbecken) besitzt drei fundamental unterschiedliche Gleichgewichte, bei identischen, in beiden Ozeanen jeweils gleichen Randbedingungen. Absinken geschieht in beiden Nordhemisphären, in beiden Südhemisphären oder in einer der beiden Nordhemisphären und nicht in der anderen. Der letzte Zustand entspricht dem beobachteten Muster der globalen thermohalinen Zirkulation.

Welches der drei verschiedenen Gleichgewichte bevorzugt eingenommen wird, hängt stark von kleinen Veränderungen im Süßwassereintrag an der Oberfläche ab. Ein Übergang zwischen zwei Zuständen ist unter Störungen der Süßwasserzufuhr möglich, die der Größenordnung des beobachteten Unterschieds zwischen Nordatlantik und Nordpazifik entspricht.

ABSTRACT

In order to understand the causes of cross-equatorial heat transport in the ocean I investigate the existence of multiple equilibria of the thermohaline circulation and instabilities leading to transitions between different steady states. Idealized ocean models are used, the crucial feature common to all models is the different coupling of temperature and salinity to the atmosphere.

A feedback mechanism which under infinitesimal perturbations leads from a state symmetric about the equator to cross-equatorial flow is demonstrated to exist in a box model of one ocean basin. The reaction of a global box model to finite-amplitude anomalies of the salinity field shows that states asymmetric about the equator are preferred to symmetric ones.

A two-dimensional model of one ocean basin also shows a transition from a symmetric to an asymmetric steady state, under very small salinity perturbations. Introduction of convective adjustment (removal of static instability) in the 2-D model greatly enhances the sensitivity to perturbations in the salinity field.

The three-dimensional GFDL model of one idealized hemisphere, with thermohaline and wind forcing, has two steady states, one of which is stable. Both states have poleward surface flow and sinking at high latitudes, but deep water formation is confined to smaller areas in the stable equilibrium. Without wind stress, no stable steady state has been found, for most of the time, the model is in a state with sinking at low latitudes and sluggish, on zonal average equatorward surface flow.

The global GFDL model with idealized geometry (two ocean basins of equal size) has three fundamentally different equilibria, under identical boundary conditions which for each state are equal in the two oceans. Sinking occurs in both Northern Hemispheres, or in both Southern Hemispheres, or in either one of the Northern Hemispheres but not in the other. The latter state corresponds to the observed global thermohaline circulation pattern.

Preference of the three different steady states depends strongly on small variations of the surface freshwater fluxes. A transition from one state to another can be accomplished by anomalies in the freshwater fluxes that have the observed order of magnitude of the differences between North Atlantic and North Pacific.

CONTENTS

1. INTRODUCTION

1.1 Thermohaline Circulation and Global Climate

The possibility of anthropogenic climate change being under way or due in the near future makes it necessary to understand the climatic system as completely as possible. The crucial role of the oceans in the process of climatic change is obvious: For example, they may buffer the man-made additional greenhouse effect due to their capacity of storing heat and carbon dioxide. On the other hand, feedbacks in the oceanic system may exist that weaken the buffering effect substantially (BRYAN and SPELMAN, 1985; MITCHELL, 1989).

In this study I shall concentrate upon mechanisms associated with the large-scale thermohaline circulation, i.e., the part of the oceanic circulation that is driven by heat and salt induced density differences between high and low latitudes. The thermohaline circulation in turn is an important transport mechanism of heat and freshwater (BRYAN, 1962; HALL and BRYDEN, 1982) and thus has a large influence on the actual distribution of heat and salt. Since heat, salt and the associated meridional circulation interact in an obviously nonlinear fashion, predicting them is not a trivial matter. My aim is to present results from idealized ocean models, which, with growing complexity, help to understand some of the physical mechanisms that set up the observed state of the global thermohaline circulation, and that may be important for changing the large-scale patterns.

The most striking feature of the global circulation is the pronounced asymmetry between the Atlantic and the Pacific Oceans. The northern North Atlantic forms North Atlantic Deep Water (NADW) at a rate of about 15-20 Sverdrups (GORDON, 1986), which spreads southward as a deep western boundary current, crosses the equator at a rate that has the order of magnitude of 10 Sv (WARREN, 1981) and spreads into the Indian and Pacific Oceans by the Antarctic Circumpolar Current (ACC). Nothing corresponding to NADW formation occurs in the North Pacific: Surface salinities are so low that even water cooled down to the freezing point cannot sink to greater depths (WARREN, 1983). Consequently, abyssal water in the North Pacific is the oldest in the world ocean, as can be determined from radiocarbon age measurements (ÖSTLUND and STUIVER, 1980; BROECKER and PENG, 1982).

Since Antarctic Bottom Watter (AABW) comprises only a small fraction of deep water flow (2 Sv across the equator in the Atlantic, WARREN, 1981) and thus may be neglected in a first approximation, a gross sketch of the global meridional circulation looks as follows: Deep water is formed in the North Atlantic, moves southward across the equator and into the other oceans, where it upwells, for then to return into the North Atlantic as thermocline water (the "conveyor belt", GORDON, 1986). It is not of great concern here whether or not Gordon's speculation is correct that the return flow of thermocline water is solely due to transport through the Indian Ocean and around Cape of Good Hope. The important point is that on annual average, warm near-surface water crosses the equator northward in the Atlantic, causing a cross-equatorial heat transport that is estimated to lie between 0.5 and 1.0 PW (e.g., WUNSCH, 1984; HSIUNG, 1985; ISEMER et al., 1989, 1 PW = 10^{15} W), with obvious impact on especially European climate.

The reason why the global circulation system works this way has been attributed mainly to different freshwater budgets in the Atlantic and the Pacific (WARREN, 1983; BROECKER, 1987): The density of sea water in the areas capable of deep water formation is controlled by its salinity. The observed higher salinities of the North Atlantic as compared to the North Pacific are maintained by the enhanced evaporation rate due to higher surface temperatures. These in turn are brought about by cross-equatorial heat transport in the Atlantic, which is due to thermocline water being imported to the North Atlantic and deep water being exported from it. The deep current again is driven by the formation of NADW, caused by high surface densities in the northern North Atlantic, which are due to the relatively high salinities. Thus the system is self-sustained in that it provides itself with high North Atlantic salinities necessary to form NADW. Looking for the causes one is faced with a "classic chicken and egg situation" (BROECKER, 1987).

Note that the most obvious hint, namely the different geometries of the Atlantic and Pacific basins, plus the existence of the ACC, does not really explain anything, because per se there is no reason why oceans of similar

meridional and different longitudinal extension must show different behaviour in deep water formation.

1.2 Paleoclimatic Evidence for Changes in the Thermohaline Circulation

To understand the present day situation is certainly a prerequisite for being able to predict possible future changes. Especially, one has to consider under what circumstances the thermohaline circulation might undergo major changes in its patterns. There is ample evidence from paleoclimatic records that the deep circulation of the world ocean varied drastically in the past. A short discussion of some methods and conclusions is given now.

The ^{13}C content of the total carbon dioxide dissolved in seawater decreases after the last contact with the surface, due to oxidation of organic matter settling from the surface. This happens because under photosynthesis a substantial isotope fractionation takes place and consequently plants are depleted of ^{13}C (DUPLESSY et al., 1988). The relative ^{13}C content of paleoceanic surface and deep waters is determined from the values found in planktonic and benthic foraminifera, respectively, both taken from deep-sea cores. DUPLESSY et al. (1988) assume that the more similar benthic and planktonic carbon isotope time series are, the closer the cores were to the sites of deep water formation. They conclude that strong convection persisted in the Southern Ocean throughout the last 150,000 years. The same applies to the Norwegian Sea except between 25,000 years and 11,000 years before present (b.p.), when no benthic foraminifera at all were found in the Norwegian Sea. DUPLESSY et al. (1988) attribute this to lack of oxygen due to cessation of deep water formation in the Norwegian Sea during the last glaciation.

From cores taken at different locations and at different depths throughout the Atlantic, DUPLESSY et al. (1988) also deduce that during the Last Glacial Maximum (LGM) NADW was formed, but only extended to $40^{0}N$. The rest of the deep ocean water had Southern Ocean origin. At mid-depths, Glacial North Atlantic Intermediate Water (GNAIW) resided between $15^{0}S$ and $45^{0}N$.

Another measure for nutrient content, and thus ventilation rate, is Cadmium, which is strongly correlated to phosphorus (BOYLE and KEIGWIN, 1987). A core taken at 4450 m depth shows that glacial deep water was Cd-enriched, meaning that NADW production was reduced. For the same time less Cd was found in a core from 2150m, indicating enhanced Intermediate Water formation (BOYLE and KEIGWIN, 1987). Along the same reasoning these authors find a shift toward stronger NADW formation at 14,000 years b.p., followed by a rapid (less than 500 years) transition to near-glacial values that lasted between 11,500 and 9,000 years b.p. This period coincided with the so-called Younger Dryas event, to be discussed below. After 9,000 years b.p., present day values persisted.

The above-mentioned shifts in the circulation coincide with climatic changes traced down in the ^{18}O content of Greenland ice cores, which reflects air temperature during the freezing process (BROECKER et al., 1985; BROECKER, 1987). 14,000 years b.p. the last glaciation came to an end, at about 11,000 years b.p. the warming process was interrupted by an 800 year-long cold period, the Younger Dryas. It also documented itself in pollen records in Europe and the very northeastern Canada. During the warm period, trees replaced the grasses and shrubs characteristic of glacial times, only to be replaced again by the glacial flora. After this, Holocene forests appeared. These climatic changes were coincidental with shifts of the polar front in the North Atlantic, which during the cold periods was situated much further south (BROECKER et al., 1985).

On a longer time scale, changes in the oceanic deep circulation have been reported by BRASS et al. (1982). The ^{18}O fraction in benthic foraminifera, which is a measure for (^{18}O depleted) total ice volume on earth, indicates that 70 Myr b.p. the deep ocean was warmer than today by about 12°C. BRASS et al. (1982) conclude that deep water to a great extent was fed by warm, saline sources, which were located at marginal seas in net evaporation areas, similar to today's Mediterranean Sea. During the following eras, the warm, saline sources disappeared along with the marginal seas.

BROECKER (1987) emphasizes that, in context of ocean circulation and climate change, one of the main lessons to be learned from paleoclimatic records is

the possibility of very rapid climate changes, like the onset and cessation of the Younger Dryas period. BROECKER et al. (1985) speculate that these changes reflect transitions between two quasi-stable equilibrium states of the oceanic circulation (Fig. 1.1). They propose that during the glaciation Atlantic and Pacific interchanged their roles, e.g., the Pacific formed Northern Deep Water and the Atlantic did not.

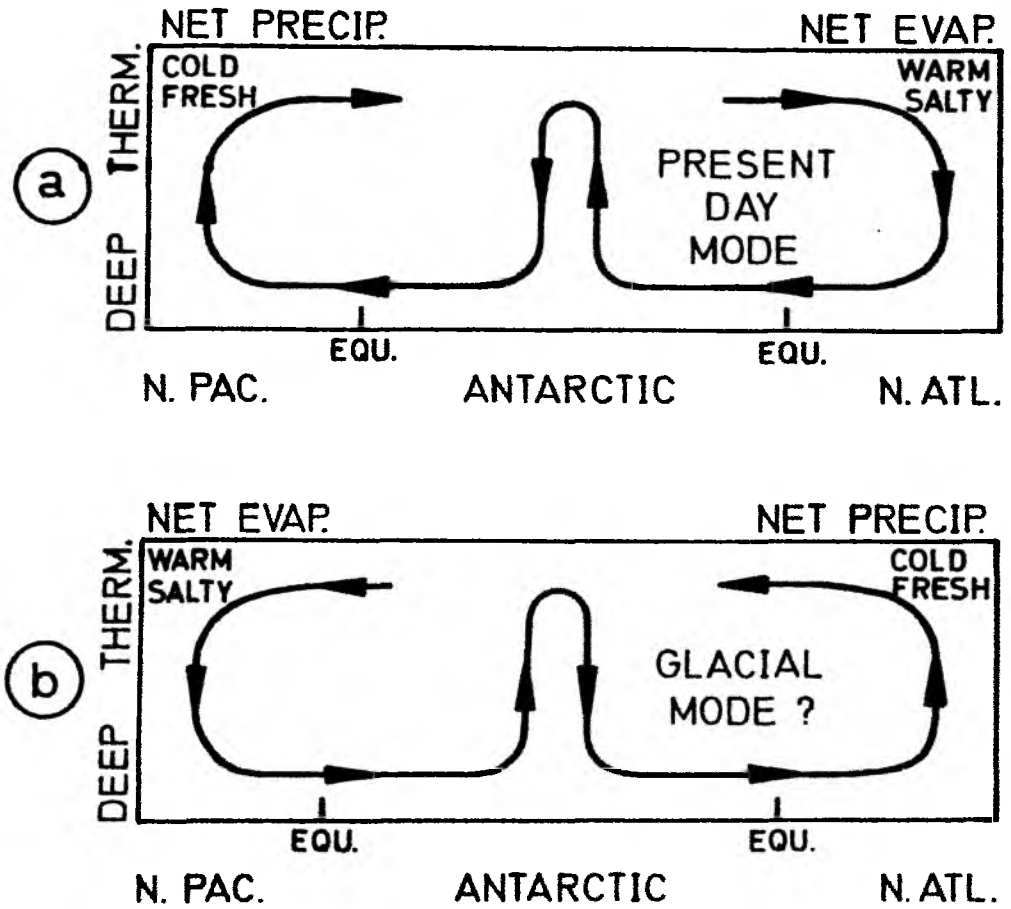

Fig. 1.1: Two possible extreme modes of oceanic circulation are displayed, corresponding to the state with deep water formation in the North Atlantic but not in the North Pacific (a), and vice versa (b). From BROECKER et al., 1985.

1.3 Thermohaline Boundary Conditions and Multiple Steady States

To date, there have been only few theoretical investigations as to why the ocean operates in the observed fashion and by what mechanisms changes may have occurred. The line of thought persued throughout this study is that the different coupling of the temperature and salinity fields to the atmosphere causes multiple equilibria of the thermohaline circulation to exist, i.e., under identical forcing there may be several steady states. Geometric and forcing differences may influence which states are preferred, but the mere possibility of several equilibria arises by the different interactions of temperature and salinity with the atmosphere.

Because sea surface temperature (SST) is strongly coupled to the surface heat flux, SST anomalies are rapidly removed by enhanced heat gain or loss (the time lag between seasonal radiative forcing and upper ocean response is 1 to 2 months). The surface salinity, however, has negligible influence on evaporation and precipitation rates, and consequently surface salinity anomalies should persist on much longer time scales.

According to the different atmospheric coupling, boundary conditions on temperature and salinity in ocean models should be different. Newtonian cooling, i.e., heat flux proportional to the difference between SST and a prescribed, "apparent" atmospheric temperature (HANEY, 1971), as commonly used in ocean models, appears to be a reasonable approximation. Note that for longer time scales this is equivalent to a prescription of SST. For salinity, however, fixed flux conditions are the crudest, physically based approximation, mirroring that evaporation minus precipitation (E-P) is independent of surface salinity. The next step would of course be to couple evaporation to the SST, but for a more detailed prescription of the precipitation an explicit atmospheric model would be needed.

Based on different boundary conditions for temperature and salinity ("mixed boundary conditions"), several models show multiple equilibria under identical forcing. STOMMEL (1961) constructed a simple box model consisting of one polar and one equatorial box, connected by pipes at the top and the bottom. He showed that the model has two stable solutions, with opposite flow

directions, if the time scales by which temperature and salinity are restored to prescribed values, are sufficiently distinct. ROOTH (1982) investigated the stability of a three-box model comprising one equatorial box and two polar boxes. Using a Newtonian-cooling condition for temperature and prescribed freshwater fluxes he suggested that a symmetric solution would become unstable, and develop into a single pole-to-pole cell under sustained symmetric forcing. WALIN (1985) discusses an advective feedback mechanism that might lead to an asymmetric circulation. WELANDER (1986) showed that a three-box model, designed according to STOMMEL (1961), has four stable equilibria, i.e., the two Stommel-solutions for each "hemisphere" of the model.

Results from investigations using a three-dimensional general circulation model (GCM) support the box-model conclusions. In a GCM with wind and thermohaline forcing symmetric to the equator, F. BRYAN (1986a,b) found that the symmetric solution was indeed unstable to a finite amplitude perturbation. An instability developed that eventually produced a single pole-to-pole cell, as suggested by ROOTH (1982).

Inadvertently, hints at the existence of multiple equilibria were found by BRYAN et al. (1975) in the first global coupled ocean-atmosphere model from the Geophysical Fluid Dynamics Laboratory (GFDL). High-latitude salinities in the North Atlantic and the North Pacific turned out to be just the opposite of the observed ones, with a very fresh North Atlantic and a relatively salty North Pacific. Recently, MANABE and STOUFFER (1988) confirmed this with a new version of the coupled GFDL model. Dependent on the initial conditions, they found two different steady states, one with a warm and salty northern North Atlantic and one with a cold and fresh one. Apparently, the solutions did not differ very much in the Pacific, besides, the (E-P) rates were very similar in the two cases.

Whereas, under proper boundary conditions, the existence of multiple equilibria of the thermohaline circulation is well established by now (and was so rather well at the beginning of this study), several questions have remained unanswered. The full range of possible equilibria of the global

circulation has not yet been explored. Furthermore, the stability of the steady states and the processes leading to a transition from one state to another have not yet been investigated systematically. In this thesis, I wish to give answers to these two sets of questions. The strategy is as follows: Using models of growing complexity, it is tested if inclusion of more realistic physics alters the solution space, and if some of the solutions exist at all stages of complexity. All the time emphasis is placed on differences brought about by the flow field in connection with the mixed boundary conditions, so the highest degree of symmetry possible was applied as regards geometry and external forcing.

In Chapter 2, a careful re-examination of the feedback processes present in box models of the STOMMEL (1961) type reveals mechanisms that may also be active in larger models. Extending the model to a two-basin ("Atlantic" + "Pacific") system, an ensemble of equilibria is found, the stability of which is analysed.

Some of the ideas are tested using a two-dimensional, meridional-plane model of the thermohaline circulation with thermohaline forcing only (Chapter 3).

The next step of complexity is the employment of the GFDL general circulation model, in a coarse-resolution version for a one-hemisphere basin. The processes leading to changes in circulation patterns are investigated in detail (Chapter 4).

In Chapter 5, the GCM is extended to comprise an idealized version of the system Atlantic-Pacific-Circumpolar Current. The aim is to find different solutions for this model, under identical forcing. It is also investigated how sensitive the model circulation reacts to perturbations in the salinity field and to variations in the freshwater fluxes.

Chapter 6 contains several more technical aspects of the GCM. It describes the interplay between surface boundary conditions and convective overturning, which is shown to be related to various oscillations in the system.

2. BOX MODELS OF THE THERMOHALINE CIRCULATION

2.1 Introduction

STOMMEL (1961) showed that a box model of thermohaline flow, comprising one polar and one equatorial box, may have three different equilibria, two of which are stable, with opposite flow directions. WELANDER (1986) extended this model by adding a second polar box (for the other hemisphere) and demonstrated that four stable steady states exist. ROOTH (1982) and WALIN (1985) use feedbacks present in box models to suggest why a symmetric thermohaline circulation in an ocean basin, with poleward surface flow in both hemispheres and sinking at both high latitudes, should undergo a transition to an asymmetric, one-cell circulation with sinking in one hemisphere only and cross-equatorial flow.

The purpose of Chapter 2 is twofold. Firstly, I want to give a more complete discussion of the feedback processes that are present in box models. This became necessary because different models gave different answers concerning the stability of the symmetric steady state, described above. In order to reconcile the differing results, I shall first re-analyse STOMMEL's (1961) two-box model and then investigate the stability of a box model comprising two hemispheres.

The second purpose of Chapter 2 is to extend WELANDER's (1986) model to a model representing two ocean basins ("Atlantic" and "Pacific"). After the basic feedback mechanisms present in box models have been investigated using the simpler models, attention is focussed on the stability of the different equilibria to finite-amplitude perturbations. To this end, the model equations are integrated numerically.

2.2 Basic Principles

The simplest box model of the ocean (STOMMEL, 1961) consists of a polar and an equatorial box, which are both completely mixed and held at constant temperatures with difference ΔT. They are connected by pipes at the top and the bottom. The surface freshwater flux, modelled as an equivalent salinity

flux, is kept fixed at H_S and $-H_S$ for the equatorial and the polar boxes, respectively. The formulation of the atmospheric coupling means a further simplification compared to STOMMEL's model who used Newtonian laws for both T and S, with different time constants. The flow is proportional to the density difference $-\alpha\Delta T + \beta\Delta S$, where ΔS is the salinity difference and α, β are the thermal and haline expansion coefficients, respectively, assumed constant for simplicity. The surface flow q is toward the polar box ($q > 0$) for $\delta = \beta\Delta S/\alpha\Delta T < 1$ and reversed for $\delta > 1$ (temperature and salinity dominated, respectively, see Fig.2.1).

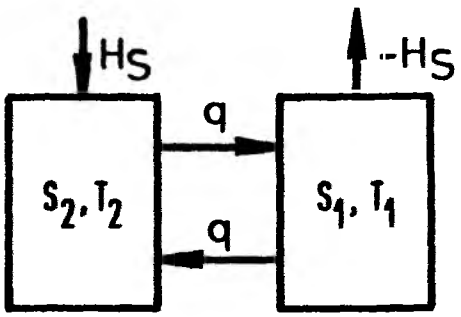

Fig. 2.1: Two-box model of the ocean. See text for definitions.

The equations for salt conservation and volume flow read:

$$\dot{S}_1 = -H_S + |q|\,(S_2 - S_1) \tag{2.1}$$

$$\dot{S}_2 = H_S - |q|\,(S_2 - S_1) \tag{2.2}$$

$$q = K\,[\alpha\Delta T - \beta(S_2 - S_1)] \tag{2.3}$$

Of course, $\dot{S}_1 + \dot{S}_2 = 0$, since total salt mass is conserved. The equilibrium condition $\dot{S}_1 = \dot{S}_2 = 0$ yields, after insertion of (2.3) in (2.1) or (2.2),

in non-dimensional form:

$$\bar{\delta} = \tfrac{1}{2} + (\tfrac{1}{4} + E)^{\frac{1}{2}} \qquad \text{for } \bar{q} < 0 \tag{2.4a}$$

$$\bar{\delta} = \tfrac{1}{2} \pm (\tfrac{1}{4} - E)^{\frac{1}{2}} \qquad \text{for } \bar{q} > 0 \tag{2.4b}$$

where the overbar marks an equilibrium value,

$$\bar{\delta} = \frac{\beta(\bar{S}_2 - \bar{S}_1)}{\alpha\Delta T}$$

is the dimensionless steady state salinity difference, and $E = \beta H_S/K(\alpha\Delta T)^2$ is a dimensionless water flux rate. For $E < 0.25$, three steady states exist, one salinity and two temperature dominated ones (the solution with $S_1 > S_2$ has been discarded). Beyond $E = 0.25$, only the salinity dominated circulation, called "inverse" circulation from now on, is a solution.

Physically, the existence of several steady states can be explained as follows: In equilibrium, the equivalent salt flux through the surface must be balanced by advection, which is the product of flow strength times salinity difference. For the same salt transport (i.e., H_S), there is the possibility of fast flow and small salinity difference, or sluggish flow and large ΔS, the latter with two flow directions.

To perform a linear stability analysis of the equilibria, write $S_1 = \bar{S}_1 + S_1'$ etc. to obtain after subtraction of the steady state condition, to first order:

$$\dot{S}_1' = \pm\, q'\Delta\bar{S} + |\,\bar{q}\,|\,(S_2' - S_1')$$

where the + sign at the first term of the r.h.s. applies for the case $\bar{q}>0$, the - sign for $\bar{q}<0$.

Using $S' = S_1' = -S_2'$ and $q' = 2k\beta S'$, one obtains:

$$\dot{S}' = \pm 2\, k\beta S' \Delta\bar{S} - 2\,|\bar{q}|\, S' \qquad (2.5)$$

There is one term providing a negative feedback, due to removal of a salinity anomaly by the mean flow. The advection of the mean salinity contrast by the flow anomaly is stabilizing or destabilizing, dependent on $\bar{\delta}$ being larger or less than 1. The inverse circulation is thus stable, for the "normal" or "positive" equilibrium the following consideration applies:

Generally, the temperature contrast ΔT can be considered as driving the circulation, the salinity contrast acts as a brake. Enhancing, say, the salinity difference by applying a negative salt anomaly to the polar box, the braking action is increased. The flow strength is reduced, a reduced amount of saline water is transported to higher latitudes (note that temperature is not affected), providing for a positive feedback. Of course, this is not the whole story: In reality, the changed heat flow may have an effect on density, and, more importantly, there exists the aforementioned negative feedback, the relative strength of which must be evaluated.

Inserting the steady state solution in (2.5) yields for the normal circulation:

$$\dot{S}' = -2k\alpha\Delta T\,(1 - 2\bar{\delta})S' \qquad (2.6)$$

The steady state with $\bar{\delta} < 0.5$ (the negative root in 2.4b) is seen to be stable, $0.5 < \bar{\delta} < 1$ (the positive root in 2.4b) is unstable. Once concludes that there exist two stable regimes of flow (STOMMEL, 1961), one of which is characterized by a strong circulation with the surface flow toward high latitudes ("positive", denoted by + from now on), the other being sluggish and reversed ("inverse", marked -). Fig 2.2 shows the equilibrium solutions in H_S - ΔS phase space. Points 1, 2 and 3 mark the steady states for fixed H_S. For prescribed δ, there exists a unique solution.

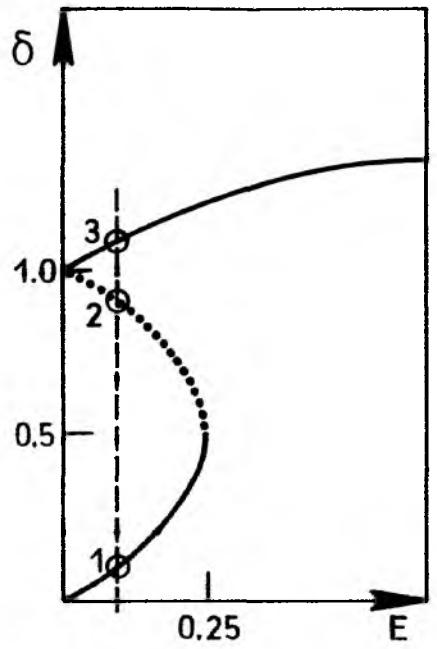

Fig. 2.2: Equilibrium states of the 2-box model from Fig. 2.1, in a ΔS - H_S phase space diagram. Axes are dimensionless salinity difference δ and dimensionless evaporation rate E, respectively. Points 1,2,3 denote the equilibria for an arbitrarily specified E. The dotted part of the curve marks the unstable regime.

With the aid of Fig 2.2, the stability behaviour of the model can be qualitatively summarized: H_S as a function of ΔS is obviously zero for $\Delta S = 0$, but also for $\delta = 1$, since then the flow vanishes. Thus, H_S must have an intermediate maximum, which in this simple case is at $\delta = 0.5$. In the range $0.5 < \delta < 1$, the steady states are unstable, since an enhancement (reduction) of the forcing H_S would lead to a decrease (increase) of the equilibrium response ΔS, in violation of Clausius' principle.

The advective feedback mechanisms involved have been discussed by WALIN (1985) and MAROTZKE et al. (1988). Nevertheless, I have performed the stability analysis in detail, because these authors draw some erroneous conclusions from it. The processes discussed here refer to only one hemisphere of an ocean basin, consequently the analysis is not valid to explain cross-equatorial instability, i.e., feedbacks leading from (symmetric) positive circulations in two hemispheres to a one-cell, pole-to-pole

circulation. Rather, the consideration may explain what F. BRYAN (1986a,b) termed "polar halocline catastrophe" in his GCM experiments with a one-hemisphere basin: He observed a spontaneous collapse of the thermohaline circulation, accompanied by a rapid shift of the polar halocline toward lower latitudes.

A detailed discussion is deferred until Chapter 4, but already now one should note the possibility of a GCM that has been run to equilibrium with essentially ΔS specified (as is usually the case), to end up in a state corresponding to point 2 in Fig. 2.2 rather than point 1. That is, the steady state might be thermally dominated but unstable, under mixed boundary conditions and exposed to very small perturbations.

2.3 Cross-Equatorial Flow and Associated Instabilities

WELANDER (1986) extended the ideas presented in Section 2.1 to the simplest model allowing for cross-equatorial flow by adding a polar box for the second hemisphere. The analysis of the possible equilibria and their stability can be performed for each hemisphere (i.e., pair of boxes) independently, yielding four stable equilibria. Two steady states are symmetric, with surface flow either poleward in both hemispheres or equatorward. In the notation introduced above, the former equilibrium has positive (thermally dominated) circulations in both hemispheres and is thus denoted ++. The latter steady state has inverse (salinity dominated) circulations in both hemispheres and is marked --. The two asymmetric equilibria, with surface flow poleward in one hemisphere and equatorward in the other (+- and -+), represent the one-cell, pole-to-pole circulation found e.g. by F. BRYAN (1986 a,b).

Using WELANDER's (1986) box model, however, leaves a gap in understanding the transition from the symmetric state to an asymmetric one. F. BRYAN (1986a) reports that adding a negative (-0.5 psu) salinity anomaly to the high latitudes of one hemisphere causes the halocline catastrophe there, followed by a rapid (about 50 years) transition to the one-cell state with sinking in the opposite hemisphere. Preventing the halocline catastrophe is achieved

by adding a large positive (+2 psu) anomaly to the high latitudes of both hemispheres. An additional anomaly of +0.5 psu in one hemisphere causes a transition to the state with sinking only there, but much more slowly (about 500 years). Omitting the asymmetric anomaly leaves the symmetric state essentially unchanged for 1300 years.

MAROTZKE et al. (1988, see chapter 3) performed similar experiments using a two-dimensional model and found that, with a δ-value of only 0.32, the symmetric equilibrium was unconditionally unstable, which is neither the case in WELANDER's (1986) model nor in F. BRYAN's (1986a,b). The transition period lasted several hundred years, and in the case of tiny anomalies (10^{-6} psu) was delayed by as much as 5000 years.

These seemingly different findings can be neatly reconciled by assuming that two different instability processes are present. One is the essentially intrahemispheric mechanism discussed in the preceding section, which is tied to the $\delta < 0.5$ or $\delta > 0.5$ criterion. The breakdown of the circulation in one hemisphere triggers the transition toward the state with sinking in the opposite hemisphere. The other process is based completely on interhemispheric connections and is presented below, via an extension of WELANDER's (1986) box model. Note that the concept of unconditional instability is unlikely to hold completely when applied to models with diffusion incorporated, which is important since transports by horizontal gyres in GCM's have to be represented as diffusion in box models. Thus, in more realistic configurations, finite amplitude perturbations may be necessary to initiate the transition described here.

As will become apparent later, the simplest box model exhibiting an independent, interhemispheric instability consists of six boxes and is displayed in Fig. 2.3. The equatorial box from WELANDER's (1986) model has been split into four, S_0 and S_2 marking the "warmwatersphere", and S_4 and S_5 the deep, low-latitude water. Furthermore, a cut was made at the equator. Temperature in the surface boxes is prescribed such that $T_0 = T_2$, $T_1 = T_3$. The flows are driven by the surface buoyancy differences, analogous to (2.3).

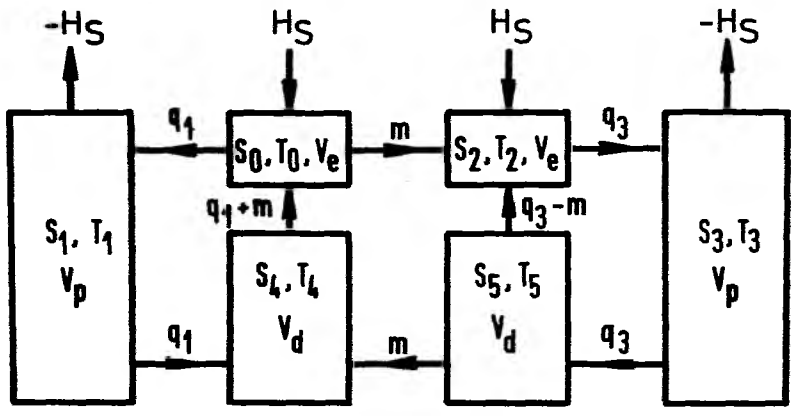

Fig. 2.3: Six-box model of one ocean basin. V_e, V_d and V_p denote the volumes of surface equatorial, deep equatorial and polar boxes, respectively.

A general observation is that, for each circulation loop to be constructed, several solutions are possible. Obviously, on increasing resolution, one has to introduce horizontal diffusion, which couples neighboured loops and reduces the number of equilibria. Since I only want to analyse the stability of the state $\bar{q}_1 > 0$, $\bar{q}_3 > 0$, $\bar{m} = 0$ with the six-box model, the additional steady states introduced by the equatorial split shall not concern us any further.

The conservation equations and the diagnostic equations for the flows read, for $m > 0$, and $\Delta T = T_0 - T_1$:

$$V_p \dot{S}_1 = - H_S + k[\alpha\Delta T - \beta(S_0-S_1)](S_0-S_1) \tag{2.7}$$

$$V_p \dot{S}_3 = -H_S + k[\alpha\Delta T - \beta(S_2-S_3)](S_2-S_3) \tag{2.8}$$

$$V_e \dot{S}_0 = H_S - k[\alpha\Delta T - \beta(S_0-S_1)](S_0-S_4) - k\beta(S_0-S_4)(S_2-S_0) \tag{2.9}$$

$$V_e \dot{S}_2 = H_S - k[\alpha\Delta T - \beta(S_2-S_3)](S_2-S_5) + k\beta(S_0-S_5)(S_2-S_0) \quad (2.10)$$

$$V_d \dot{S}_4 = k[\alpha\Delta T - \beta(S_0-S_1)](S_1-S_4) + k\beta(S_5-S_4)(S_2-S_0) \quad (2.11)$$

$$V_d \dot{S}_5 = k[\alpha\Delta T - \beta(S_2-S_3)](S_3-S_5) \quad (2.12)$$

$$q_1 = k[\alpha\Delta T - \beta(S_0-S_1)] \quad (2.13)$$

$$q_3 = k[\alpha\Delta T - \beta(S_2-S_3)] \quad (2.14)$$

$$m = k\beta(S_2-S_0) \quad (2.15)$$

Obviously, there exists a steady state with $\bar{S}_0 = \bar{S}_2$, $\bar{S}_1 = \bar{S}_4 = \bar{S}_5 = \bar{S}_3$, $\bar{q}_1, \bar{q}_3 > 0$, $\bar{m} = 0$ (compare equ. (2.1) - (2.4)). Its linear stability behaviour is analysed by writing $S_1 = \bar{S}_1 + S_1'$ etc., subtracting the equilibrium part from the conservation equations and retaining deviations from equilibrium only to first order. One obtains a set of coupled linear, constant-coefficient, first order differential equations in the S_i'. The eigenvalues of the coefficient matrix determine the stability of the equilibrium: If at least one of them has a real part larger than zero, the steady state is unstable, as small deviations will grow exponentially (see, e.g., BENDER and ORSZAG, 1978).

The procedure yields the linearized equations:

$$V_p \dot{S}_1' = c_\delta(S_0'-S_1') \quad (2.16)$$

$$V_p \dot{S}_3' = c_\delta(S_2'-S_3') \quad (2.17)$$

$$V_e \dot{S}_0' = -b_\delta(S_0'-S_4') + k\beta\Delta S(S_0'-S_1') - k\beta\Delta S(S_2'-S_0') \quad (2.18)$$

$$V_e \dot{S}'_2 = -b_\delta(S'_2-S'_5) + k\beta\Delta S(S'_2-S'_3) + k\beta\Delta S(S'_2-S'_0) \tag{2.19}$$

$$V_d \dot{S}'_4 = b_\delta(S'_1-S'_4) \tag{2.20}$$

$$V_d \dot{S}'_5 = b_\delta(S'_3-S'_5) \tag{2.21}$$

with $\Delta S = \bar{S}_0-\bar{S}_1$, $c_\delta = k\alpha\Delta T(1-2\delta)$, $b_\delta = k\alpha\Delta T(1-\delta)$, $\delta = \dfrac{\beta\Delta S}{\alpha\Delta T}$.

Now introduce a new set of variables that are, respectively, the symmetric and antisymmetric combinations of corresponding boxes in the two hemispheres:

$$U = S'_2 + S'_0 \qquad V = S'_3 + S'_1 \qquad W = S'_5 + S'_4$$

$$X = S'_2 - S'_0 \qquad Y = S'_3 - S'_1 \qquad Z = S'_5 - S'_4$$

(2.16) until (2.21) now decouple in that the symmetric and the antisymmetric variables each form an independent set of equations, which in matrix notation read:

$$\begin{pmatrix} \dot{U} \\ \dot{V} \\ \dot{W} \end{pmatrix} = \underline{\underline{A}} \begin{pmatrix} U \\ V \\ W \end{pmatrix} = \begin{pmatrix} -c_\delta/V_e & -\dfrac{k\beta}{V_e}\Delta S & b_\delta/V_e \\ c_\delta/V_p & -c_\delta/V_p & 0 \\ 0 & b_\delta/V_d & -b_\delta/V_d \end{pmatrix} \begin{pmatrix} U \\ V \\ W \end{pmatrix}$$

$$\begin{pmatrix} \dot{X} \\ \dot{Y} \\ \dot{Z} \end{pmatrix} = \underline{\underline{B}} \begin{pmatrix} X \\ Y \\ Z \end{pmatrix} = \begin{pmatrix} -c_\delta/V_e + \dfrac{2k\beta\Delta S}{V_e} & -\dfrac{k\beta}{V_e}\Delta S & b_\delta/V_e \\ c_\delta/V_p & -c_\delta/V_p & 0 \\ 0 & b_\delta/V_d & -b_\delta/V_d \end{pmatrix} \begin{pmatrix} X \\ Y \\ Z \end{pmatrix}$$

The only difference between the two matrices is the term describing a feedback of the difference between the surface equatorial boxes upon itself.

Using $c_\delta = b_\delta - k\beta\Delta s$, it is easily seen that $\det(\underline{\underline{A}}) = 0$, whereas

$$\det(\underline{\underline{B}}) = \frac{2k\beta\Delta S}{V_e} \cdot \frac{b_\delta}{V_d} \cdot \frac{c_\delta}{V_p} \tag{2.22}$$

The matrix describing the symmetric part thus has an eigenvalue 0 (which corresponds to total salt conservation), the other two are easily found and bring about the same $\delta > 0.5$ vs. $\delta < 0.5$ criterion as the one-hemisphere model.

For matrix $\underline{\underline{B}}$, we remember that $\det(\underline{\underline{B}})$ is the product of the three eigenvalues (see, e.g., LINGENBERG, 1976). We see from (2.22) that for $\delta < 0.5$, $\det(\underline{\underline{B}}) > 0$, meaning that at least one eigenvalue is larger than zero: The roots of a third order equation are either all real, or there is one real one and a complex conjugate pair. Assume the real parts of λ_2, λ_3 to be smaller than zero. Their product is real and positive, since $\lambda_2\lambda_3 = \lambda_2\lambda_2^* = (\mathrm{Re}\lambda_2)^2 + (\mathrm{Im}\lambda_2)^2 > 0$, if they are complex. Thus, λ_1 must be real and positive, meaning that the antisymmetric variables have at least one growing mode, due to the cross-equatorial feedback between the surface layers.

Thus, the cross-equatorial flow m will grow if once started: Assume m to to be positive initially, to be definite. It is driven by $S_2' - S_0'$, and directed toward box S_2 which has higher salinity (and thus density). The perturbation flow m transports salty water out of box S_0 and fresh water into it (out of S_4), thus decreasing its salinity further, compared to box S_2. Within each hemisphere, the stability criterion may be fulfilled, and the anomaly is spread over the whole hemisphere. The difference between the hemisphere-averaged salinities, however, grows due to the positive feedback, unless there is a diffusive, down-gradient salt flux between the equatorial

surface boxes. We see why the equatorial box had to be split in four: No horizontal subdivision means infinite horizontal diffusion, without vertical split m would simply have transported S_2-water back to S_0 (meaning zero transport, to first order).

Whereas allowing for low-latitude deep water is certainly realistic, the significance of the linearly growing interhemispheric mode is less clear, since north- and south-equatorial regions of the oceans are strongly coupled. On constructing box models it may be best to re-abandon the equatorial split after it helped understanding the differing model results, the more so since unconditionally unstable states are not the most interesting ones, being never realized in nature.

2.4 Stability of a Global Box Model under Finite-Amplitude Perturbations

As already stated at the end of the preceding section, the most adequate box model for one ocean basin consists of four boxes, with two polar and two equatorial ones, the latter representing the thermocline and deep water, respectively. This model is now extended to represent the global thermohaline circulation. The Indian Ocean is considered passive, so the global box model comprises the four hemispheres of the Atlantic and the Pacific (Fig. 2.4).

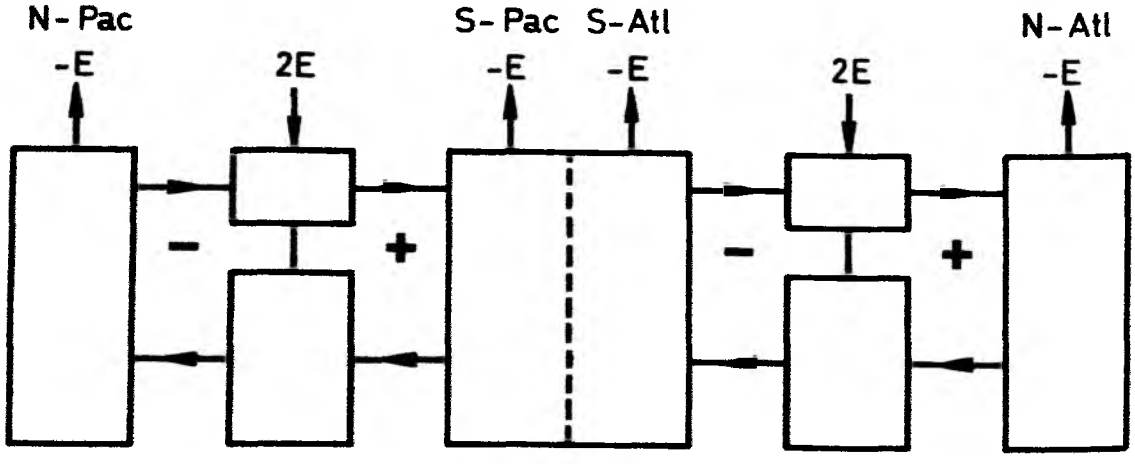

Fig. 2.4: "Global" box model, comprising North and Equatorial Pacific and Atlantic, plus the Southern Ocean. In each hemisphere two flow directions are possible, with surface flow either poleward (+) or equatorward (-). The state -+-+ thus corresponds to today's global thermohaline circulation.

The Southern Ocean is regarded as a single basin, since the Circumpolar Current efficiently provides for zonal homogenization. The sizes of the boxes are defined such as to reflect the approximate volumes of the cold and warm water masses in the ocean. The equations for the system are easily found by generalizing (2.7) - (2.15), note that they are equivalent to an upstream finite difference descretization for the continuous conservation equations (see MESINGER and ARAKAWA, 1976).

From the results of sections 2.2 and 2.3 it follows that in each of the four hemispheres of the global box model two stable equilibria exist, with different flow directions. Thus there is a total of 16 equilibria, the stability of which is analysed now (again, the different states are denoted by marking poleward surface flow + and equatorward surface flow - , for each hemisphere).

After the nature of unconditional instabilities has been clarified, attention shall be focussed now on the reaction of the stable solutions to finite-amplitude salinity perturbations. The general strategy is to add to every steady state a series (typically 1000 each) of randomly chosen surface salinity perturbations, integrate these initial states numerically and simply count how frequently the different equilibria are eventually obtained. This gives a measure of the various steady states' catchment area in phase space. The basic parameters are dimensionless equivalent salt flux E (see equ. 2.4), and the amplitude of the normally distributed initial perturbations.

Preliminary experiments were performed using one-hemisphere (3 boxes) or one-basin (4 boxes) versions. As expected, the three-box model shows a strong dependence on E: the closer it comes to the critical value of 0.25, the less likely the positive circulation (surface flow towards high latitudes) is obtained as a final state. Increasing the amplitude of the anomaly (i.e., its variance), a transition between two different states becomes more probable, but preference hardly changes. Since the dependence on E is almost trivial, I shall concentrate upon the other parameters.

The four-box model, which closely resembles WELANDER's (1986), shows a similar dependence on E, but enhancement of the initial perturbation leads

to a preference of the asymmetric states (+- and -+). This can be understood by noting that these states have rather large salinity contrast between the two high latitudes. Using equ. (2.4) which relates the dimensionless salinity difference

$$\bar{\delta} = \frac{\beta \Delta \bar{S}}{\alpha \Delta T}$$

between the boxes of one hemisphere to the dimensionless water flux rate E, one obtains for E = 0.15:

$\bar{\delta}_1 = 0.18$ positive branch (+)

$\bar{\delta}_2 = 1.13$ inverse branch (-).

Thus, the dimensionless salinities of the two polar boxes differ by 0.95, and it is plausible that the larger the variance of the initial perturbation, the larger is the probability of a flip from the catchment area of a symmetric state to the domain of an asymmetric one. Fig. 2.5 shows the frequency distribution of the final states, for two different amplitudes σ_δ of the initial perturbation. The salinity anomalies are given in dimensionless units, i.e., the same units as the $\bar{\delta}$-values mentioned above. One sees that the initial perturbation must be rather large in order to make flips to a different equilibrium likely.

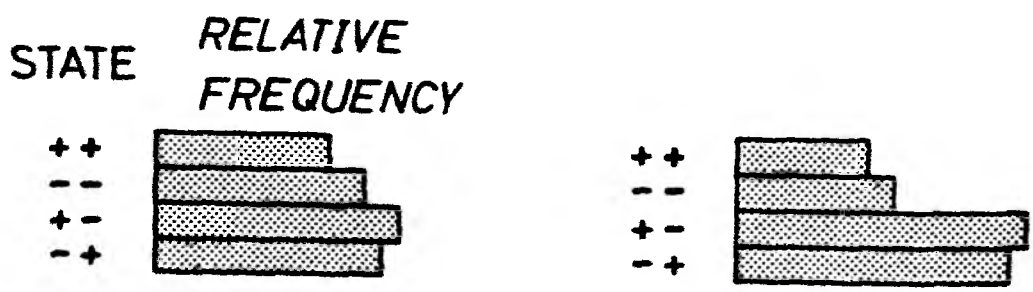

Fig. 2.5: 4-box model (one half of Fig. 2.4). Relative frequency distribution of the different equilibria as final states.
a) E = 0.15, σ_δ = 0.5, b) E = 0.15, σ_δ = 1.

Fig. 2.6 displays the experiments corresponding to Fig. 2.5, but for the full "global" model. The general tendencies, as inferred from the smaller models, are also present: The inverse branches are favoured more and more as E increases (not shown), and the totally symmetric states disappear as the anomalies get larger. However, the states with the largest global salinity difference (+-+- and -+-+ , $\delta = 2(\bar{\delta}_2 - \bar{\delta}_1) = 1.9$, see above) are not simply preferred, as might be expected from the 4-box model. Using truly huge anomalies ($\sigma_\delta = 100$) this is the case, but at moderate (O(1)) distances away in phase space, the solutions symmetric with respect to the two basins and antisymmetric about the equator are clearly favoured. Why the +--+ state again is preferred to -++- is not clear.

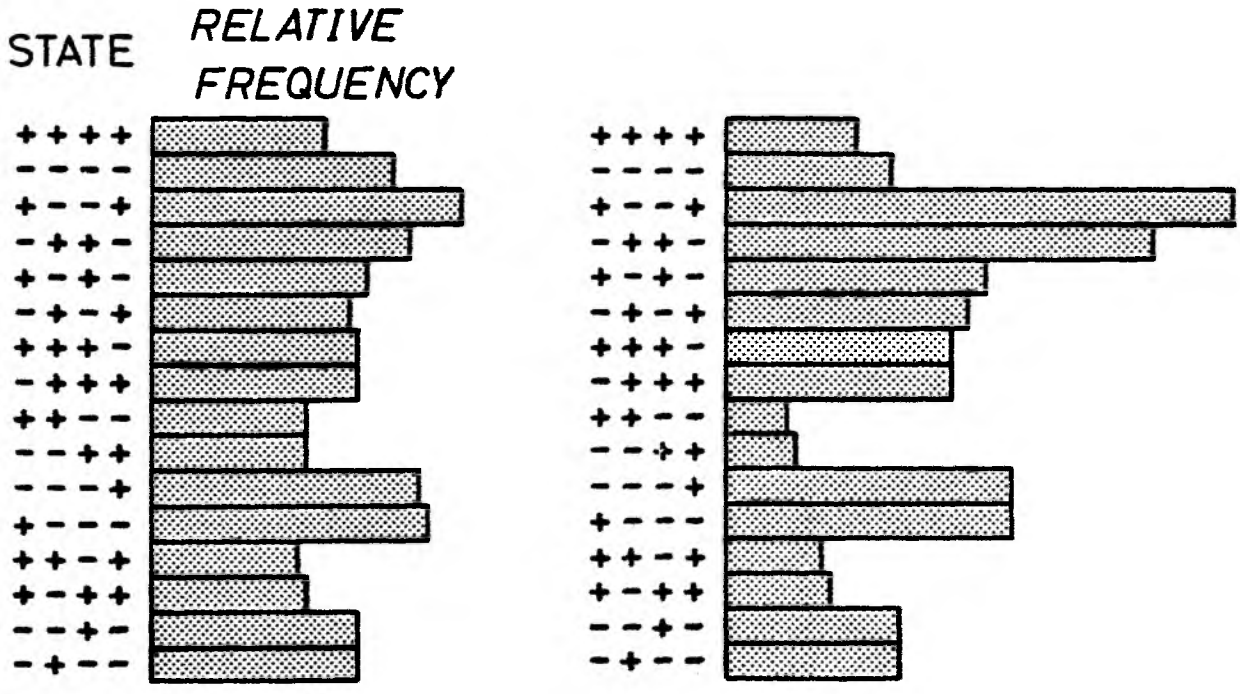

Fig. 2.6: Global box model. Relative frequency distribution of the different equilibria as final states.
a) E = 0.15, $\sigma_\delta = 0.5$, b) E = 0.15, $\sigma_\delta = 1$.

Generally, the states with flow directions different in the two Southern Hemispheres are strongly inhibited (Fig. 2.6). This can be understood using the following consideration: The Southern Ocean (SO) box provides a coupling between the two pairs of equatorial ocean boxes. When the integration is started far away from an equilibrium, and there are different flow directions in the two Southern Hemispheres, one loop (+ , surface flow toward SO) transfers salty water to the SO box and the other one (-) fresh water. These tendencies counteract each other in the attempt to maintain either high (by the " + "-loop) or low (by the " - "-loop) salinities in the SO box. If, on the other hand, the initial flow directions are equal, both loops transport either high salinity (in the ++ case) or low salinity (--) water to the SO box. Thus, there will be a clear tendency toward either high or low salinity in the SO box, and the larger catchment areas of the states with equal circulations in the Southern Hemispheres are plausible.

Introducing an anomaly ΔE in the freshwater forcing of the two northern boxes (positive in one box, negative in the other), not only brings about the trivial effect of selecting between the two oceans (e.g., one of +-+- and -+-+ is favoured), but also reduces the dominance of the +--+ and -++- states (Fig. 2.7, ΔE positive in NP). ΔE acts similar to a larger initial perturbation in that the states with the largest salinity difference between NA and NP are favoured more strongly.

Concluding we see that three main effects are influencing the behaviour of the global box model:

1) A stronger freshwater forcing favours the inverse circulation.

2) Higher initial salinity differences between the two northernmost boxes tend to bring about the circulation corresponding to the "conveyor belt" (GORDON, 1986).

3) The latter effect is counteracted by the homogenization of the Southern Ocean, leading to equal circulations in the Southern Hemispheres.

Clearly, the box model is too crude to predict what state the real ocean will take. Still, it catches some of the most important aspects determining

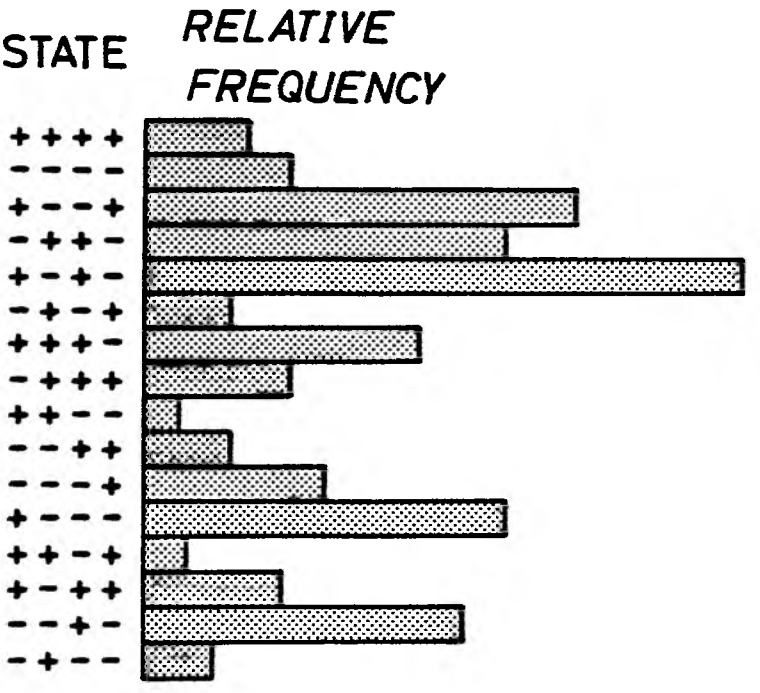

Fig. 2.7: Global box model. Relative frequency distribution of the different equilibria as final states.
$E = 0.15$, $\sigma_\delta = 1$, $\Delta E = 0.09$ (positive in NP, negative in NA).

the global circulation. The atmospheric coupling is correct to the lowest order. Heat and freshwater transport in the ocean is achieved mainly by the meridional overturning (BRYAN, 1962, HALL and BRYDEN, 1982) and is thus properly represented by the box model. The interplay of atmospheric forcing and meridional transports is seen to create the possibility of multiple equilibria and various instability processes that lead to transitions between the different steady states. Wind forcing is not explicitly included in the model, but the Ekman-part of heat and salt transport can be modelled by simply choosing a higher value of $\alpha\Delta T$, i.e., the constant part of the meridional flow. In this sense, $\overline{\delta}$ should be assumed lower than the value suggested by merely taking the pole-to-equator temperature and salinity contrasts.

Of course, in order to reach a higher degree of realism, diffusion has to be included to model gyre transports. Since its effect would be an overall stabilizing one, plus reduction of the number of equilibria, this is not essential when one is looking for basic properties of the thermohaline circulation. It may be more important that convective overturning is absent, i.e., rapid removal of static instability when it occurs. Especially the interruption of convection is a very fast process, and this short time scale is missing in the model.

Last but not least, in assessing the box model's value one should keep in mind their efficiency as regards computer time. The calculation for plotting a histogram like Fig. 2.7 took about one hour on a VAX 8550. Opposed to this, a single run to equilibrium of the next-simplest model, a version of the two-dimensional model discussed in Chapter 3, required one minute on a CRAY-XMP. This would mean about 250 hours on a CRAY-XMP for the 16,000 runs to equilibrium displayed in Fig. 2.7, rendering it completely impractical to systematically explore the phase space, even with the relatively simple two-dimensional model.

3. 2-DIMENSIONAL MODEL

3.1 Model Description

Box models give insight into the basic physical processes leading to multiple steady states of the thermohaline circulation, and help to gain a feeling for which of these states are more likely to be obtained than others. Of course, box models are only very crude representations of the real ocean, the main shortcomings being the inability to model small-scale processes, of which convective overturning is the most important in connection with deep water formation, and the absence of rotation, which makes it impossible to model the most fundamental dynamical balance, geostrophy. The two-dimensional, meridional-plane model presented here overcomes the first deficiency, but not the second. It has sufficient horizontal and vertical resolution to represent the ocean's meridional temperature and salinity distributions, but the presence of zonal boundaries renders any consistent dynamical description of the flow field difficult, if not impossible, because a 2-D model cannot simply be interpreted as representing a zonally averaged ocean.

The 2-D model is thus best regarded as a high-resolution box model, where still meridional flow strength is related to meridional density gradients by a very simple law. A detailed discussion of this assumption is given in MAROTZKE et al. (1988). Since most of the results described there can be explained with the even simpler box models (Chapter 2), or confirmed with the 3-dimensional model (Chapters 4 and 5), I shall in this chapter concentrate upon the topics where the 2-D model still has actuality. It serves as a link between the very primitive box models and the full blown GCM, helping to understand in how far concepts from the former can be transferred to the latter, and where they cannot, explain why.

The heat and salt budgets are given by

$$\partial_t T + v\partial_y T + w\partial_z T = k\partial_{zz} T + C_T \qquad (3.1a)$$

$$\partial_t S + v\partial_y S + w\partial_z S = k\partial_{zz} S + C_S \qquad (3.1b)$$

where C_T, C_S indicate convective adjustment which results in complete vertical mixing whenever the stratification is locally unstable. Some of the numerical experiments described below are performed without this adjustment mechanism. Horizontal diffusion has not been included explicitely in (3.1), since the numerical scheme used (upstream spatial differences, see below) has strong numerical diffusion (MESINGER and ARAKAWA, 1976).

Meridional flow is determined by a balance between vertical friction and meridional pressure gradient:

$$A\,\partial_{zz}v = \partial_y p \tag{3.2}$$

where A is chosen as to give realistic meridional transports for likewise realistic density gradients. Introducing a stream function according to $w = \partial_y\psi$, $v = -\partial_z\psi$, invoking the hydrostatic relation and assuming a linear equation of state yields:

$$\partial_{zzzz}\psi = \frac{g}{A}\,(-\alpha\partial_y T + \beta\partial_y S) \tag{3.3}$$

where α and β again are the thermal and haline expansion coefficients, respectively. The boundary condition $\psi = 0$ on all boundaries is employed, moreover $\partial_{zz}\psi = 0$ at the surface (no wind stress) and $\partial_z\psi = 0$ (no slip) at the bottom, which is assumed insulating ($\partial_z T = \partial_z S = 0$). A picture of the model domain and the boundary conditions is given in Fig. 3.1.

The thermohaline surface boundary conditions are of course the essential ones. Following F. BRYAN (1986a,b), a spin-up experiment is run where surface temperature and salinity are prescribed, obeying a cosine law in latitude

$$T_o = T_* \left(1 + \cos\frac{\pi y}{L}\right) \tag{3.4a}$$

$$S_o = S_* \left(1 + \cos\frac{\pi y}{L}\right) \tag{3.4b}$$

with amplitudes $2T_*$ and $2S_*$ of 25°C and 2 psu, respectively. From the spin-up steady state, the freshwater flux (or equivalent salinity flux Q_S) necessary to maintain the equilibrium, is diagnosed. The meridional structure of Q_S is also displayed in Fig. 3.1.

The most important model parameter is the relative influence of salinity on density, expressed as $\delta = \beta S_*/\alpha T_*$, as for the box models. The other model parameters are chosen such that the maximum stream function value is 1.6 m^2/s, which corresponds to 10 Sv meridional transport in a basin of 6000 km width (MAROTZKE et al., 1988).

The prognostic equations (3.1) for temperature and salinity are solved by finite difference methods, using forward time differences and upstream spatial differences on a rather coarse grid (16 levels vertical, 32 horizontal grid points for the two-hemisphere version shown in Fig. 3.1, 16 horizontal points for the one-hemisphere model).

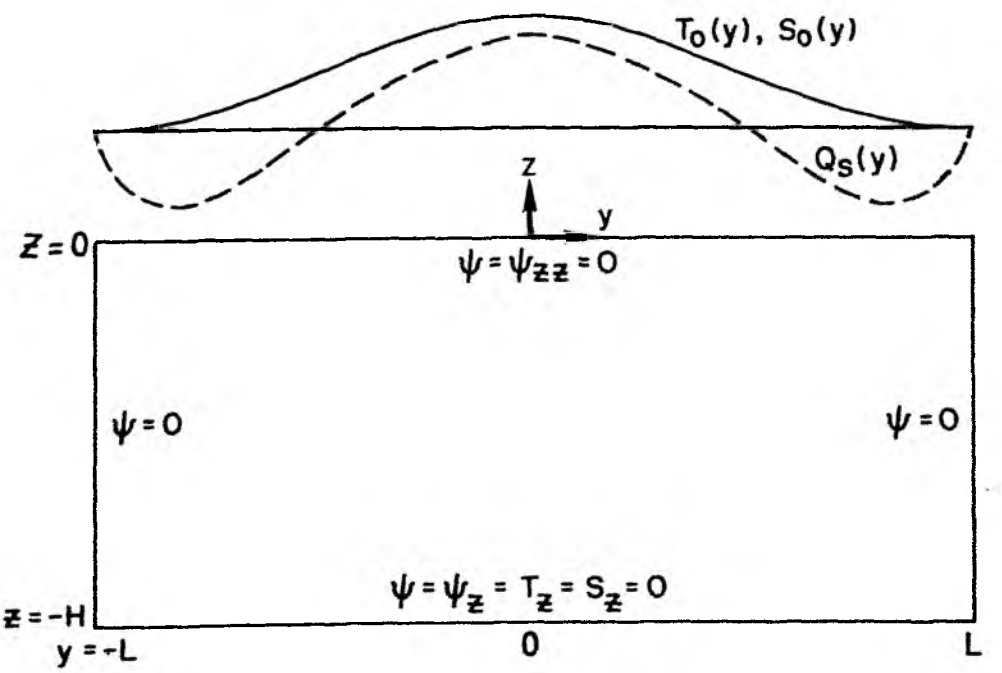

Fig. 3.1: The 2-D model ocean in a meridional plane, indicating boundary conditions for the stream function ψ, and bottom conditions for temperature T and salinity S. At the surface, $T_0(y)$, $S_0(y)$ (full drawn curve) are prescribed; after a symmetric steady state is obtained, the condition for surface salinity is changed, with the resulting freshwater flux $Q_S(y)$ (dashed curve) prescribed.

3.2 Experiments and Results

The box models suggest that two different instability mechanisms may cause transitions from one steady state of the thermohaline circulation to another. I want to show now that these distinct processes also are present in the 2-D model, besides, how convective adjustment influences the stability behaviour of the equilibria.

Assuming the thermal and haline expansion coefficients to be $2 \cdot 10^{-4} K^{-1}$ and $0.8 \cdot 10^{-3}$ gives a δ of 0.32, which is used as standard value. The spin-up for the two-hemisphere model including convective adjustment is shown in Figs. 3.2a,b. The fields are seen to be perfectly symmetric, the salient feature being the existence of two overturning cells, with strong downwelling in polar regions and weaker upwelling everywhere else. The pronounced boundary layers at the side boundaries are confined to one grid cell, as is to be expected due to the lack of explicit horizontal friction. Temperature and density distributions are identical to that of salinity in the symmetric case. Thermocline structure and overturning pattern show a satisfactory agreement with the results of F. BRYAN (1986a,b).

Using the surface salinity flux diagnosed from the spin-up, the state depicted in Fig. 3.2 should be unstable, if the results from the 6-box model (Section 2.3) hold. Actually, this is seen to be the case: A positive initial salinity anomaly as small as 10^{-6} psu, added to the top layer in the northern half of the northern (right) hemisphere, causes the spin-up to flip over to a strongly asymmetric state with sinking in the northern hemisphere only (Figs. 3.3a-c). Associated are very low surface salinities in the south, and also the interior temperature field shows asymmetries.

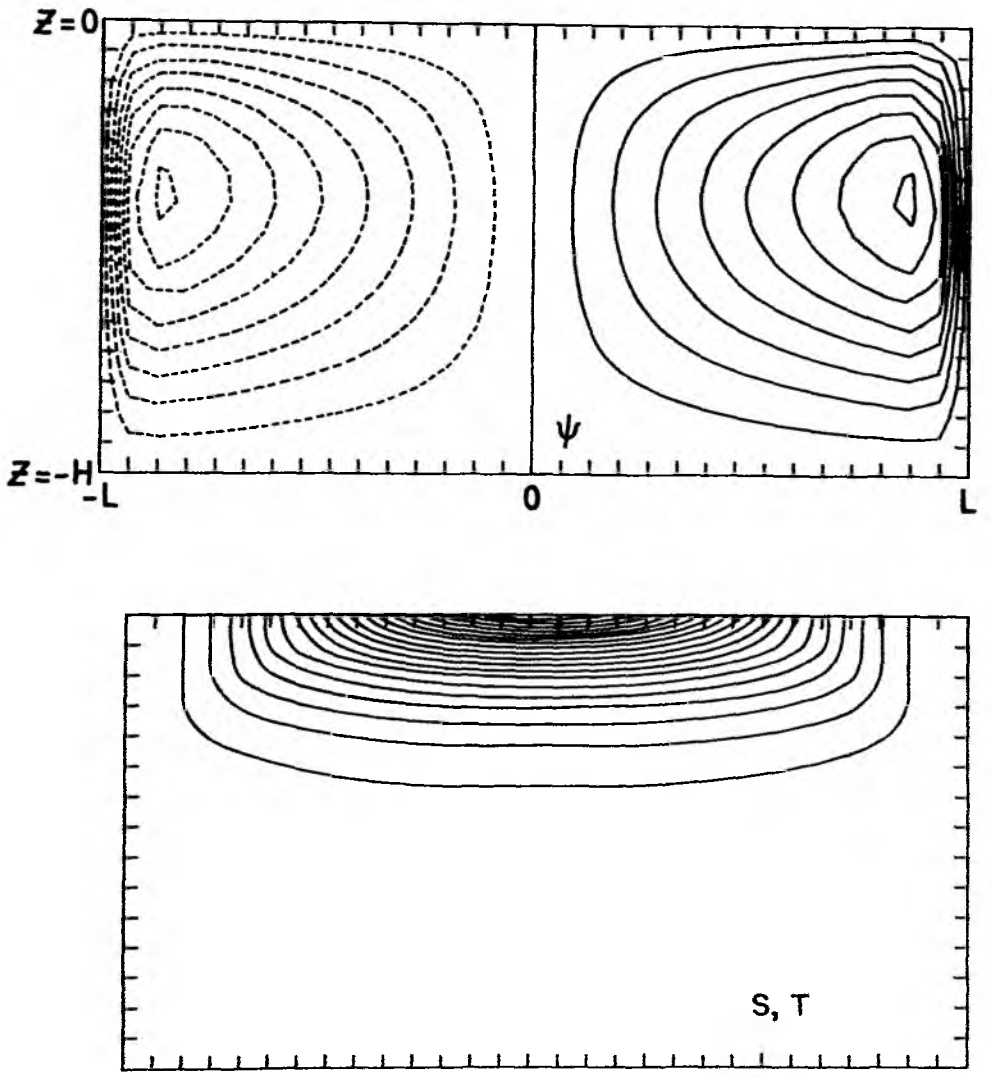

Fig. 3.2: 2-D model, fields of stream function (a) and salinity (b) in the symmetric steady state, with δ = 0.32. With the standard set of parameters, the maximum value of ψ is 1.6 m^2s^{-1}, which corresponds to a total transport of 10 Sv in a basin of 6000 km width. Contour intervals are 0.2 m^2s^{-1} (a) and 0.1 psu (b).

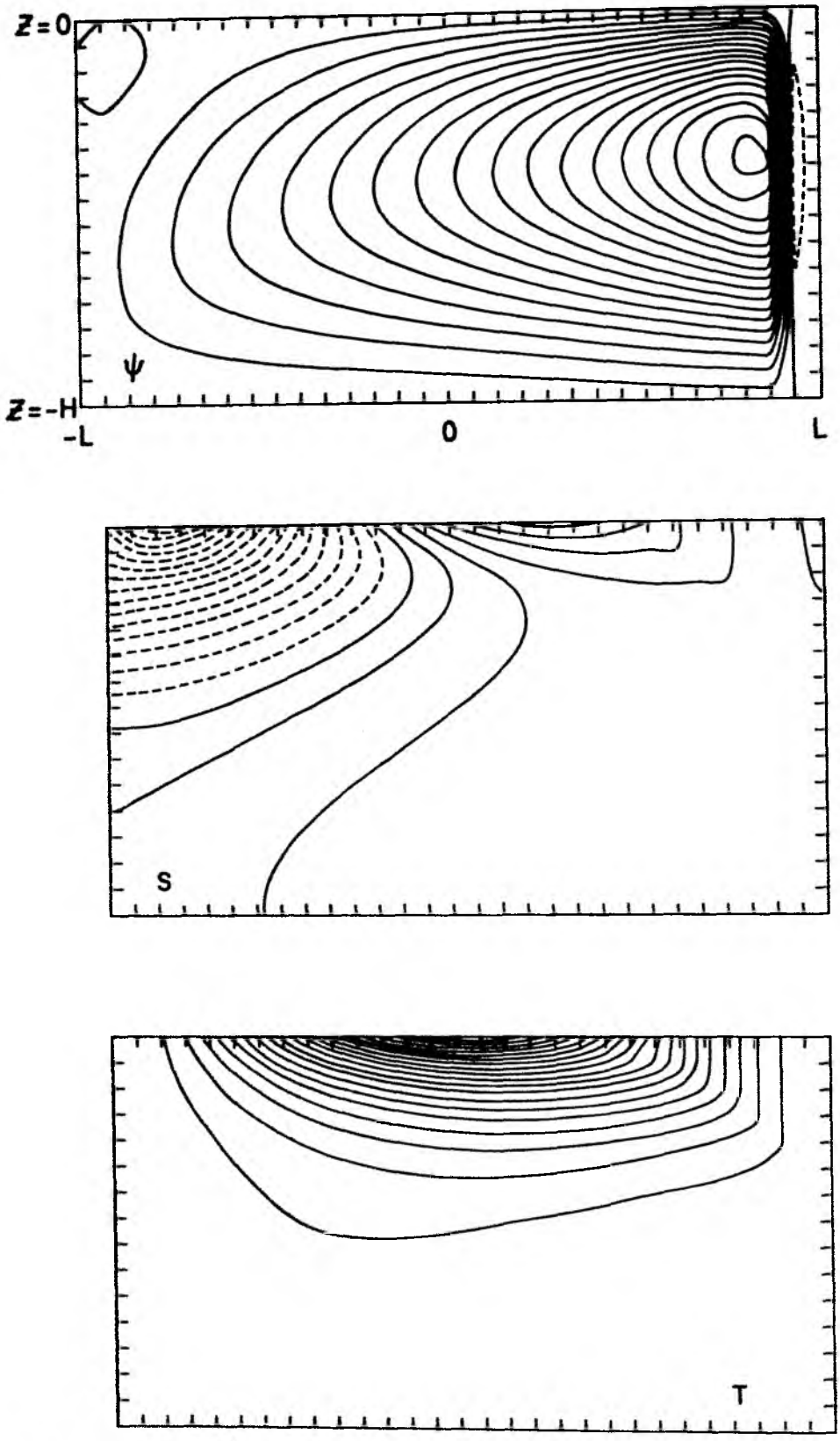

Fig. 3.3: 2-D model, stream function (a), salinity (b) and temperature (c) after a new steady state has been achieved in the perturbation experiment. The maximum value of ψ is increased to 2.6 m^2s^{-1}. Contour intervals are 0.15 m^2s^{-1} (a), 0.2 psu (b), and 1.25 ^0C (c).

Convective adjustment does not qualitatively influence this behaviour: In the experiments where static instability is not removed, the initial state is still unconditionally unstable, and again a 10^{-6} psu anomaly suffices to cause the transition. Both symmetric (spin-up) and asymmetric steady states are very similar to the ones displayed in Figs. 3.2 and 3.3, respectively. The meridional heat transports of the four different equilibria are shown in Fig. 3.4. In the cases including convective adjustment the transports are slightly higher than without. From Fig. 3.5 showing the time development of the basin averaged heat flux for the experiment with a 10^{-6} psu anomaly, with and without convective adjustment, it is seen that the former shows a more rapid and violent reaction, and stronger oscillatory behaviour. However, qualitatively the inclusion of convective adjustment does not have any influence on the transition from the symmetric to the asymmetric state. It should be mentioned that the curves in Fig. 3.5 are identical for small negative anomalies (-10^{-6} psu), applied to the same volume.

Convective adjustment should play a more important role for the stability of the equilibria exposed to finite amplitude anomalies. To be able to seperate distinct processes I shall investigate this for a one-hemisphere version of the model.

The spin-up looks just like the right half of Figs. 3.2a,b, and again different initial salinity anomalies are applied. With $\delta = 0.32$, the state proved stable to positive and relatively large negative anomalies (-0.5 psu in the top 500 m in the poleward one third of the basin). It required -0.5 psu in the upper 750 m, again in the northern one third, to cause a flip to an equilibrium that corresponds to the inverse state from the box models (point 3 in Fig. 2.2). It has large salinity contrasts (Fig. 3.6a) and a reversed circulation, with downwelling at the equator and about half the original strength (Fig. 3.6b). To qualitatively test the $\delta < 0.5$ vs. $\delta > 0.5$ stability criterion from the box models, a few experiments were performed with $\delta = 0.7$. Any anomaly caused a transition to the inverse state, so the 2-D model again confirms the box models.

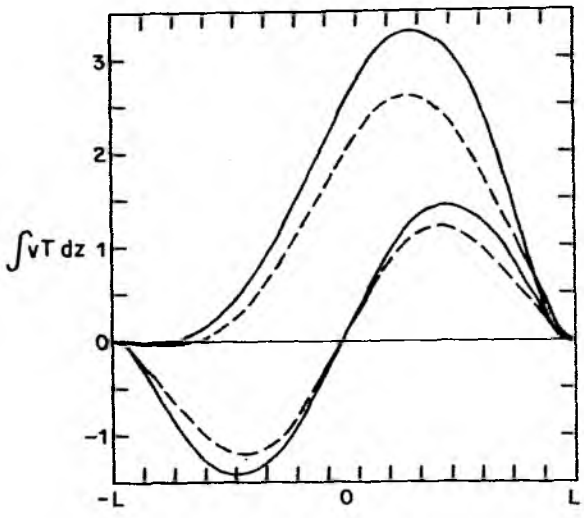

Fig. 3.4: 2-D model, meridional heat transport as function of y in the symmetric steady state (lower curves), and asymmetric steady state (upper curves). The full drawn curves show the result with and the dashed curves the result without convective adjustment. Units are dimensionless and correspond to 0.15 x 10^{15} W for the standard parameters and a basin of 6000 km zonal width.

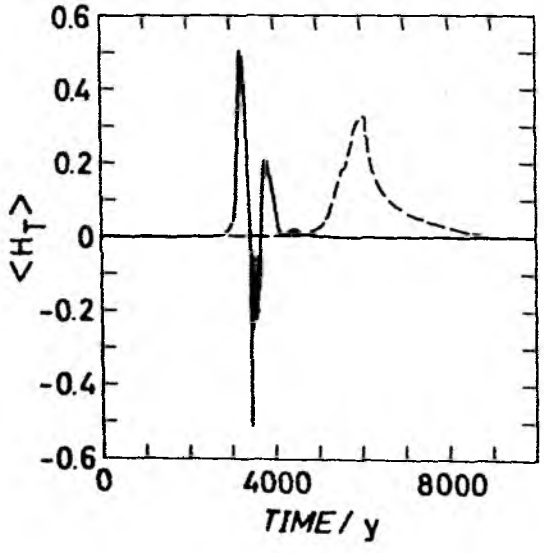

Fig. 3.5: 2-D model, basin averaged surface heat uptake as function of time with convective adjustment (full drawn curve) and without convective adjustment (dashed curve), for the perturbation experiment with the 10^{-6} salininity anomaly. Dimensionless units correspond to 0.22 W/m^2 for standard parameters.

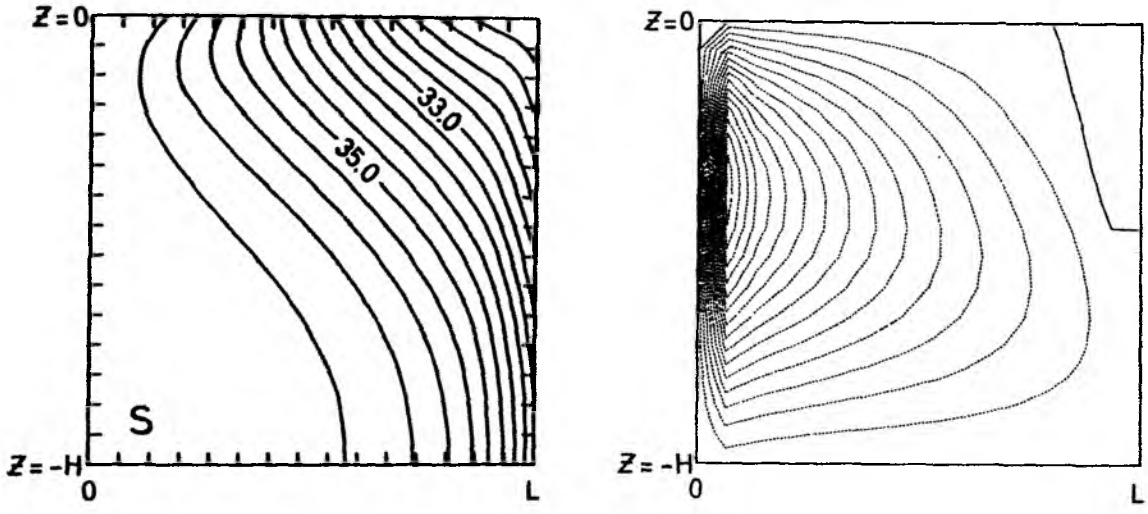

Fig. 3.6: One-hemisphere 2-D model, inverse steady state, without convective adjustment. a) salinity, contour interval 0.2 psu, b) stream function, minimum corresponding to 4.75 Sv, contour interval 0.3 Sv.

The situation changes dramatically, however, if convective adjustment is present. Firstly, a much smaller anomaly is sufficient to cause the transition, the threshold lying between -0.01 and -0.02 psu in the top layer (250 m) of the same area as before. This can be understood from a local self-amplification of a negative salinity anomaly, under mixed boundary conditions: Convection is interrupted, the water parcels are longer exposed to the (usually) net freshwater input at the surface, and salinity is further reduced. This local freshening can be a very efficient trigger for the advective instability causing the transition to a different equilibrium.

However, there is a second, more spectacular change due to convection, since the state depicted in Figs 3.6a,b shows static instability near the surface, at high latitudes, and thus cannot be obtained under more realistic conditions. Strong convective processes occur, causing a short period of extremely violent positive circulation, afterwards the system returns to

the reverse mode. As Fig. 3.7 shows, this happens periodically, with a period of approximately 16 times the travel time of a water particle around the basin. The discussion in Section 4.5 will show that this behaviour is not merely a peculiarity of the 2-D model. Moreover, the physical processes involved will be investigated.

As a final remark, note that if in the 2-hemisphere model a large enough negative anomaly is applied symmetrically about the equator, symmetry is maintained, i.e., both hemispheres behave like the 1-hemisphere model. The transition to the reverse state occurs in both hemispheres, including the oscillations in the case with convection. The unconditional interhemispheric instability is thus seen to be absent for the inverse (--) circulation.

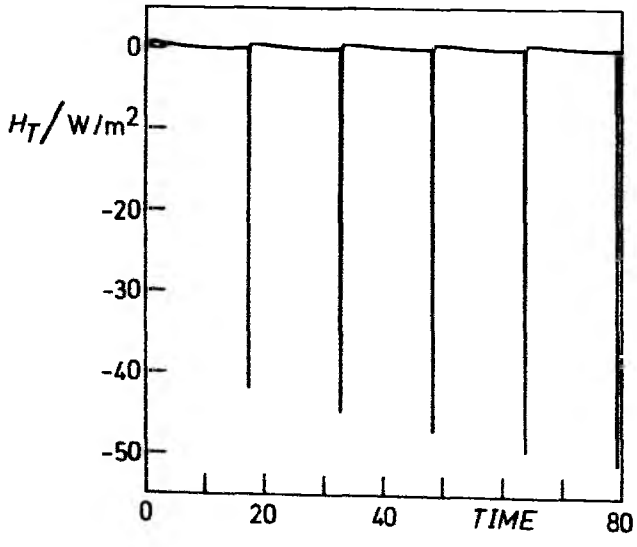

Fig. 3.7: One-hemisphere 2-D-model, including convective adjustment. Time series of basin averaged heat uptake H_T for anomaly experiment with a -0.02 psu anomaly in the top layer (250 m) of the right one third of the basin. Time unit is dimensionless overturning time for a water particle.

4. ONE-HEMISPHERE GFDL MODEL

4.1 Introduction

In the preceding chapters, the fundamental possibility of multiple equilibria of the thermohaline circulation has been demonstrated using simple models, and instabilities associated with the transition from one steady state to another have been analysed. I shall now investigate in how far the ideas developed in the preceding chapters carry over to more realistic models. According to the philosophy stated in the introduction, this means primarily inclusion of additional physical processes, and not in any sense an attempt to present an actual simulation of the oceanic circulation. The crucial step is of course to take account of the ocean's three-dimensionality, allowing to represent explicitly the geostrophic balance of the large-scale circulation.

The pioneering work was done by F. BRYAN (1986a,b) using a three-dimensional general circulation model (GCM) of a two-hemisphere ocean basin, with wind and thermohaline forcing symmetric about the equator. By effectively prescribing surface temperature and salinity he obtained a solution symmetric about the equator, with sinking at both high latitudes. Then he shifted over to a flux condition for salinity (*mixed boundary conditions*), and the circulation was found to be unstable to finite-amplitude perturbations of the salinity field. Eventually an asymmetric circulation emerged, with sinking in one hemisphere only.

Starting point for the work described in this chapter is another of F. BRYAN's (1986a,b) results: For a one-hemisphere version of his model, the thermohaline circulation spontaneously becomes unstable, 80 years after shifting over to mixed boundary conditions. The polar halocline spreads equatorward and the meridional circulation collapses within 20 years ("polar halocline catastrophe"). The onset of the collapse was traced to intermittency in convection, leading to the formation of a pool of low-salinity water which then rapidly expanded. However, the nature of the instability mechanism that was triggered by this event remained unclear, and the further time development was not documented.

The results I obtained using the simple models (Chapters 2 and 3) suggest that the "polar halocline catastrophy" might be the beginning of the transition to a different steady state of the one-hemisphere GCM. To test this hypothesis, I performed a series of numerical experiments in order to clarify under which conditions the "halocline catastrophe" occurs and how it leads to the collapse of the meridional circulation. Moreover, I investigated which state emerged as final solution after the breakdown.

4.2 Model Description

The model used is the GFDL GCM based on the method described by BRYAN (1969), in the version documented and distributed by COX (1984). Remembering that we are interested in qualitative, overall features of the thermohaline circulation and that the integration time spans several thousand years, some restrictions arise naturally: The model must have coarse resolution, no dependence on model parameters like mixing coefficients is investigated, and the model geometry and spatial structure of forcing functions are chosen as simple as possible in order to avoid any interference with regional effects. Since, with very few exceptions, the standard model was used, I keep the model description as terse as possible, for any further information see the two references cited.

The model is based on the primitive equations, which are derived from the conservation equations for momentum, mass, heat and salt, plus the equation of state, by invoking the Boussinesq and the thin shell approximations (the latter implying the hydrostatic approximation). For a more detailed derivation, see MÜLLER and WILLEBRAND (1989). Moreover, molecular and tidal effects are neglected. Using coarse resolution the Rossby number is of order 0.01 ($Ro = U/fL \sim 0.2/(10^{-4} \cdot 2 \cdot 10^5)$) even on gridsize length scale, so the nonlinear terms in the equations of motion are neglected. The remaining set of equations read (notation is standard, spherical coordinates are used):

$$\partial_t \underline{u} + \underline{f} \times \underline{u} = -\frac{1}{\rho_0} \underline{\nabla} p + A_{MH} \underline{\nabla}^2 \underline{u} + A_{MV} \partial_{zz} \underline{u} \tag{4.1}$$

$$\partial_t \theta + (\underline{u} \cdot \underline{\nabla}) \theta + w \partial_z \theta = A_{HH} \underline{\nabla}^2 \theta + A_{HV} \partial_{zz} \theta + C_\theta \tag{4.2}$$

$$\partial_t S + (\underline{u} \cdot \underline{\nabla}) S + w \partial_z S = A_{HH} \underline{\nabla}^2 S + A_{HV} \partial_{zz} S + C_S \tag{4.3}$$

$$\underline{\nabla} \cdot \underline{u} + \partial_z w = 0 \tag{4.4}$$

$$g\rho = -\partial_z p \tag{4.5}$$

$$\rho = \rho(S, \theta, p) \tag{4.6}$$

The standard closure assumptions about turbulent fluxes have been employed, i.e., mixing along coordinate surfaces and constant mixing coefficients. Potential temperature θ is used to allow for compressibility effects whereas sound waves are filtered out. For the equation of state, the polynomial approximation of BRYAN and COX (1972) is applied. C_θ and C_S in (4.2) and (4.3) represent, in a symbolic manner, removal of static instability by some convective adjustment process. The scheme used here differs from the standard one and guarantees complete vertical stability after the procedure. It was successfully applied in the 2-D model, a more detailed discussion is deferred until Chapter 6.

The bottom and the lateral walls are assumed insulating (zero heat and salt flux), at the lateral walls a "no slip" condition ($\underline{u} = 0$) is applied, at the bottom a "free slip" condition ($\partial_z \underline{u} = 0$). Wind stress, if present, is purely zonal and prescribed as a simple function of latitude only, reflecting the major features of the observed distribution (Fig. 4.1).

The "rigid lid" approximation, i.e., setting

$$w = 0 \quad \text{at} \quad z = 0 \tag{4.7},$$

neglects kinematic effects of surface displacement and eliminates external gravity waves (see, e.g., GILL, 1982), which otherwise would severely limit the time step of the integration. Instead of the surface elevation or the surface pressure, the stream function of the vertically integrated volume transport is now used as a prognostic variable. The stream function is defined by

$$a^{-1}\,\partial_\phi \psi = -\int_{-H}^{0} u\,dz = -H\bar{u} \tag{4.8a}$$

$$(a\cos\phi)^{-1}\,\partial_\lambda \psi = \int_{-H}^{0} v\,dz = H\bar{v} \tag{4.8b}$$

where a is the earth's radius. Integrating the equations of motion (4.1) vertically and taking the curl yields.

$$\begin{aligned}
&\partial_t \left[a^2 \cos\phi\, \underline{\nabla} \cdot (H^{-1}\, \underline{\nabla}\, \psi) \right] = \\
&\partial_\lambda \left(\overset{f}{\overline{H}} \right) \partial_\phi \psi - \partial_\phi \left(\overset{f}{\overline{H}} \right) \partial_\lambda \psi \\
&- \partial_\lambda \left[\frac{g}{\rho_0 H} \int_{-H}^{0} \int_{z}^{0} \partial_\phi \rho\, dz'\, dz \right] \\
&+ \partial_\phi \left[\frac{g}{\rho_0 H} \int_{-H}^{0} \int_{z}^{0} \partial_\lambda \rho\, dz'\, dz \right] \\
&+ \partial_\lambda \left[\frac{a}{H} \int_{-H}^{0} G^{(\phi)}\, dz \right] - \partial_\phi \left[\frac{a\cos\phi}{H} \int_{-H}^{0} G^{(\lambda)}\, dz \right]
\end{aligned} \tag{4.9}$$

where the $G^{(\phi,\lambda)}$ summarize the nonlinear (if present) and dissipative terms. The curl operation eliminates the surface pressure. (4.9) is a

prognostic equation for $\underline{\nabla} \cdot (H^{-1} \underline{\nabla} \psi)$. It can also be regarded as an elliptic equation for $\partial_t \psi$, which is solved at each timestep, using the kinematic boundary condition ψ = const and the "no-slip" condition $\partial_n \psi = 0$. In a model with flat bottom and linear momentum balance, the steady state stream function is solely determined by the wind stress curl (WILLEBRAND, 1989).

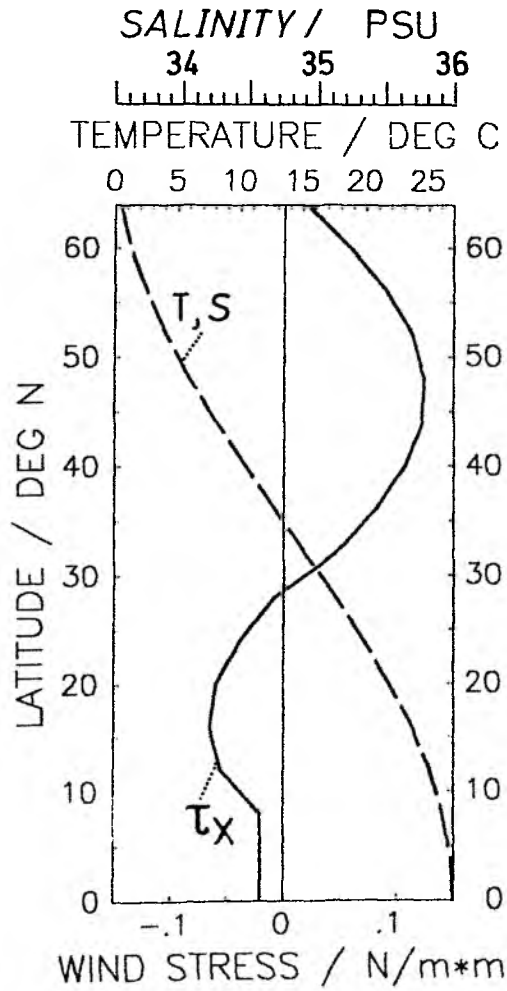

Fig. 4.1: Forcing fields of the one-hemisphere GFDL model: Zonal (eastward) wind stress τ_x in N/m^2 (solid curve), apparent atmospheric temperature T_a in $^{\circ}C$ and restoring salinity field S_a in psu (dashed curve), as functions of latitude.

The oceanic heat gain H_T at the surface is given as a Newtonian cooling law:

$$H_T = \rho_0 \, c \, D \, \lambda \, (T_a - T_S) \tag{4.10}$$

where c is specific heat, D the depth of the top layer, λ^{-1} a time constant and T_S surface temperature. T_a is a prescribed apparent atmospheric temperature (HANEY, 1971). Equ. (4.10) means that the SST is restored to the prescibed values T_a, with a time constant λ^{-1} chosen as 30 days. T_a follows a cosine law in latitude, with a difference of 27°C between high and low latitudes (Fig. 4.1), which closely resembles the observed, zonally averaged values (see F. BRYAN, 1987). Surface boundary conditions on salinity, which are the crucial ones, are discussed in Section 4.2.

The model domain is a 60° wide sector extending from the equator to 64°N, with a constant depth of 4500 m. The horizontal resolution is 3.75° longitude and 4° latitude. There are 15 levels in the vertical, with resolution varying from 50 m near the surface to 500 m near the bottom.

Although the choice of mixing coefficients is somewhat arbitrary there are some guidelines. BRYAN et al. (1975) report that a spatial computational mode is excited if the grid does not resolve the viscous western boundary layer. This means that, given a certain resolution, A_{MH} must be large enough to widen the boundary current beyond one gridpoint distance, i.e.:

$$\Delta x < L = \frac{\pi}{\sqrt{3}} \left(\frac{A_{MH}}{\beta}\right)^{1/3}$$

(BRYAN et al. 1975, the order of magnitude of the r.h.s. is easily found by balancing friction and planetary vorticity advection in the barotropic vorticity equation). F. BRYAN (1987) showed that thermocline depth, meridional overturning strength and thus meridional heat transport depend on vertical diffusivity of heat and salt (i.e., the intensity of diabatic processes), following a 1/3-power law.

In close accordance to F. BRYAN (1986a,b; 1987), I chose the parameters $A_{MH} = 2.5 \cdot 10^5\ m^2s^{-1}$, $A_{MV} = 10^{-4}\ m^2s^{-1}$, $A_{HH} = 10^3\ m^2s^{-1}$ and $A_{HV} = 0.5 \cdot 10^{-4}\ m^2s^{-1}$, the latter being in the middle of the range explored by F. BRYAN and used as his standard.

The time step is limited primarily by the Courant-Friedrichs-Levy (CFL) criterion stating that in one time step advective or phase propagation must not occur over a distance of more than one grid size (MESINGER and ARAKAWA, 1976). The fastest waves in the GFDL model are external Rossby waves with maximum phase speed of order 10 m/s, and internal inertia-gravity waves with phase speed of about 3 m/s. Temperature and salt are advected with much lower speeds, however (maximum about 15 cm/s in coarse resolution models), suggesting to use different time steps in the heat/salt and momentum/vorticity equations, respectively. As BRYAN (1984) shows, this technique, called asynchronous integration, leaves the equilibrium solution unchanged but slows down internal gravity waves by a factor of $\alpha^{\frac{1}{2}}$ and external Rossby waves by a factor of α, α being the ratio of temperature/salt to velocity time steps. Since I am mainly interested in processes of decadal time scales, improper representation of the fast waves is of no importance. Internal Rossby waves which accomplish the adjustment of the density field to changes in the forcing (e.g., changes in the deep water formation rate), are hardly affected, since their wavelengths are large compared to the internal radius of deformation (BRYAN, 1984).

Asynchronous integration thus makes an integration over thousands of oceanic years possible, while properly representing the processes of primary interest. Still, during periods of rapid variation in the circulation patterns, the integration is performed synchronously to obtain maximum accuracy. The choice of time step was two hours during the synchronous and five days for θ and S during the asynchronous integration. At times, one day had to be chosen to restrict salinity fluxes in regions of extreme salinity gradients. Since a semi-implicit treatment of the Coriolis-terms is applied, the inertial period need not be resolved.

4.3 Experimental Strategy and Initial Conditions

Among the boundary conditions specified in Section 4.2 the surface ones for salinity were missing. The most natural way to perform the experiments would of course be to specify evaporation minus precipitation (E-P) and start the integrations from some state which is either at rest or, alternatively, close to an observed one. However, E-P is one of the least well known quantities in oceanography, so any specification is subject to large uncertainties (see, however, SCHMITT et al., 1989).

To be more definite, I adopted the strategy used by F. BRYAN (1986a,b) and in the 2-D case: The model is spun up from a state of rest, applying Newton-type boundary conditions both on sea surface temperature and salinity with a time constant of 30 days. This means to impose an equivalent salinity flux which causes a change of surface salinity according to

$$\partial_t S = \lambda(S_a - S) \tag{4.11}$$

S_a is analogous to the apparent atmospheric temperature T_a of equ. (4.10). In order to transform the equivalent salinity flux into a physical quantity one observes that a given (E-P) rate (in m/s) brings about a surface salinity change of

$$\partial_t S = \frac{E - P}{D} S_0 \tag{4.12}$$

(STERN, 1975, p.187), where D is the depth of the top layer and S_0 a constant reference salinity. S_0 is approximated as a constant because then (4.12) implies total salinity conservation if the global (E-P) budget is balanced.

Three different spin-up states were produced, the characteristic properties of which are summarized in Table 1. Experiment S1 is forced by the zonal wind stress and the zonally invariant restoring salinity S_a displayed in Fig. 4.1. Analogous to the apparent atmospheric temperature, the latter follows a cosine-law in latitude, with an amplitude S_* of 2.5 psu. The spatial structure

of S_a means that the local minimum in E-P associated with the Intertropical Convergence Zone is neglected. For experiment S2 the same S_a field is used as for S1, but wind stress is absent. S3 includes the wind stress of Fig. 4.1, but the amplitude S_* of the restoring salinity field is reduced to 1.5 psu, while S_a still follows a cosine-law.

Table 1: Spin-up Experiments with the 1-Hemisphere GFDL Model

Experiment	Wind stress present?	S_*/psu	P-E
S1	yes	2.5	HS1
S2	no	2.5	HS2
S3	yes	1.5	HS3

S_* : Amplitude of the restoring salinity S_a.
P-E: Set of surface freshwater fluxes diagnosed from the experiment.

With these boundary conditions, the model is integrated asynchronously for 5476 years in the three cases. At this time an almost complete equilibrium is reached, the basin averaged heat uptake being less than 10^{-4} Wm^{-2}. To be sure, a 46 year period of synchronous integration is appended, from which a time-average of equivalent surface salinity fluxes is diagnosed. These fluxes are used as a fixed flux boundary condition for salinity in the sensitivity experiments described below.

The spin-up states not only provide for the required freshwater fluxes but also serve as initial states for most subsequent experiments. It is the instability of such a spin-up state that was called "polar halocline catastrophe" by F. BRYAN (1986a,b), and the causes of which are under investigation here.

The most characteristic properties of the states S1 (wind-driven) and S2 (no wind) are discussed now. Similar model results are analysed in detail

by COX and BRYAN (1984) and F. BRYAN (1986a, 1987), so I mention only briefly what is needed for the discussion following afterwards.

Generally the two steady states S1 and S2 show a close overall resemblance. The surface fields of temperature and salinity follow the restoring values very closely (see Fig. 4.1), reflecting the relative weakness of advective transports compared to the surface fluxes. Even in the western boundary currents the isotherms and isohalines deviate only slightly from the zonal means, because maximum surface velocities are only 14 cm/s in the wind-driven case (S1) and 6 cm/s in the no-wind case (S2).

The horizontal gyre structure is reflected by the surface heat flux (Figs. 4.2a,b), the main difference between the cases S1 and S2 lying in the larger intensities of the former. Even in the wind-driven case, there is no pronounced subpolar gyre, because at my choice of parameters the thermohaline influence on the thermocline structure dominates the wind influence (F. BRYAN, 1986a, 1987). Regions of major heat loss are the western boundary regions, where warm water is advected northward and forced to give off heat to the atmosphere, and the northeastern part of the basin. Convective activity is strongest there, since at high latitudes poleward movement is most pronounced in the eastern part, in accordance with the results by COX and BRYAN (1984).

Meridional volume transport is best displayed by the use of the meridional overturning stream function, which is defined by first integrating the continuity equation (4.4) zonally, yielding

$$(u - v\cos\phi\partial_\phi\lambda)\Big|_{\lambda_W}^{\lambda_E} + \partial_\phi \int_{\lambda_W}^{\lambda_E} v\cos\phi d\lambda + \partial_z \int_{\lambda_W}^{\lambda_E} w\, a\cos\phi d\lambda = 0 \qquad (4.13)$$

where a is the earth's radius and $\partial_\phi\lambda$ means the variation with latitude of the eastern or western boundary. If rigid walls are present at both λ_E and λ_W (i.e., no flow normal to the wall, $u = v\cos\phi\partial_\phi\lambda$ at the boundaries), or, alternatively, periodic boundary conditions are applied at the zonal boundaries, the meridional stream function can be defined according to

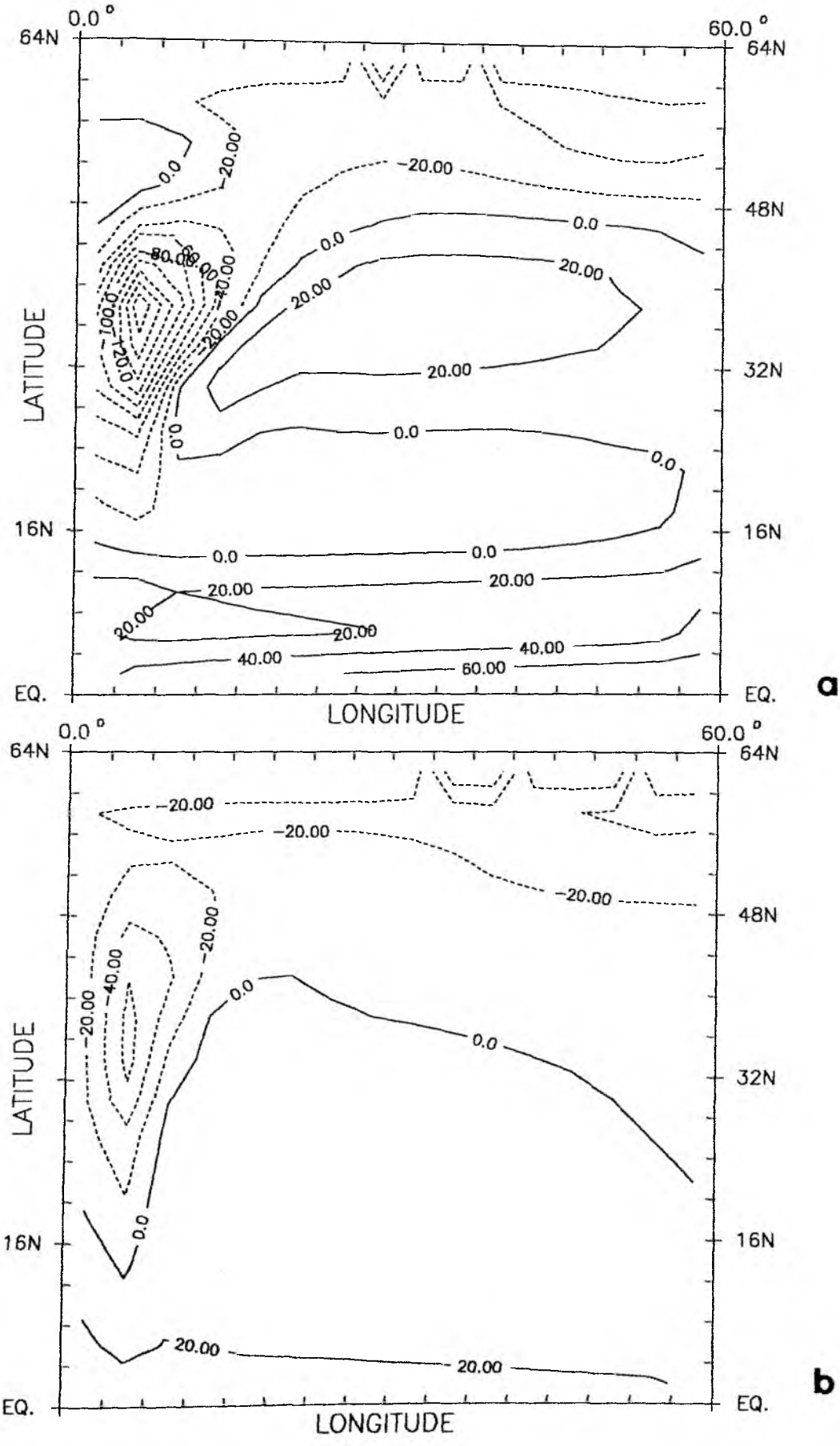

Fig. 4.2: Spin-up steady state of the one-hemisphere GFDL model. Surface heat flux in W/m^2 , positive values denote ocean heat uptake, for (a) experiment S1 (with wind) and (b) experiment S2 (no wind).

$$-\partial_z \Psi = \int_{\lambda_W}^{\lambda_E} v \cos\phi \, d\lambda$$

$$\partial_\phi \Psi = \int_{\lambda_W}^{\lambda_E} w \, a \cos\phi \, d\lambda$$

as cross-differentiation shows.

The meridional stream function is displayed in Figs. 4.3a,b. Sinking occurs north of 52°N and is weaker by 1 Sv in the case of no wind. The deep water moves equatorward in a deep western boundary current (not shown here). In Fig. 4.3a the wind-driven cells are clearly visible, wherein the Ekman transport is compensated by a return flow reaching down to 200 m. These cells can be visualized as being superimposed on top of the thermohaline circulation. As is the case for overturning strength as a whole (F. BRYAN, 1987), no scaling argument for the depth of the wind-driven cells has been found to date. This may be due to the fact that the meridional transport is the (small) residual of boundary current strength minus recirculation, i.e., is determined by at least two dynamically different regimes, rendering a detailed forecast difficult. One should note, however, how well the simple 2-D model is able to represent the overturning of the GCM.

The meridional heat transport can be split in an advective and a diffusive part. The advective part, which is $\rho_0 c v \theta$, integrated over a zonal section across the entire basin, can be partitioned further according to

$$\int_{-H}^{0} dz \, \rho_0 c \, L \, \langle v\theta \rangle = \int_{-H}^{0} dz \rho_0 c \, L \, \langle v \rangle \langle \theta \rangle + \int_{-H}^{0} dz \rho_0 c \, L \, \langle v'\theta' \rangle \qquad (4.14),$$

$\langle\ \rangle$ and $'$ denoting zonal average and deviation thereof, respectively. The first part on the r.h.s. of (4.14) is due to transport by meridional overturning, the second arises from the correlation of deviations from the

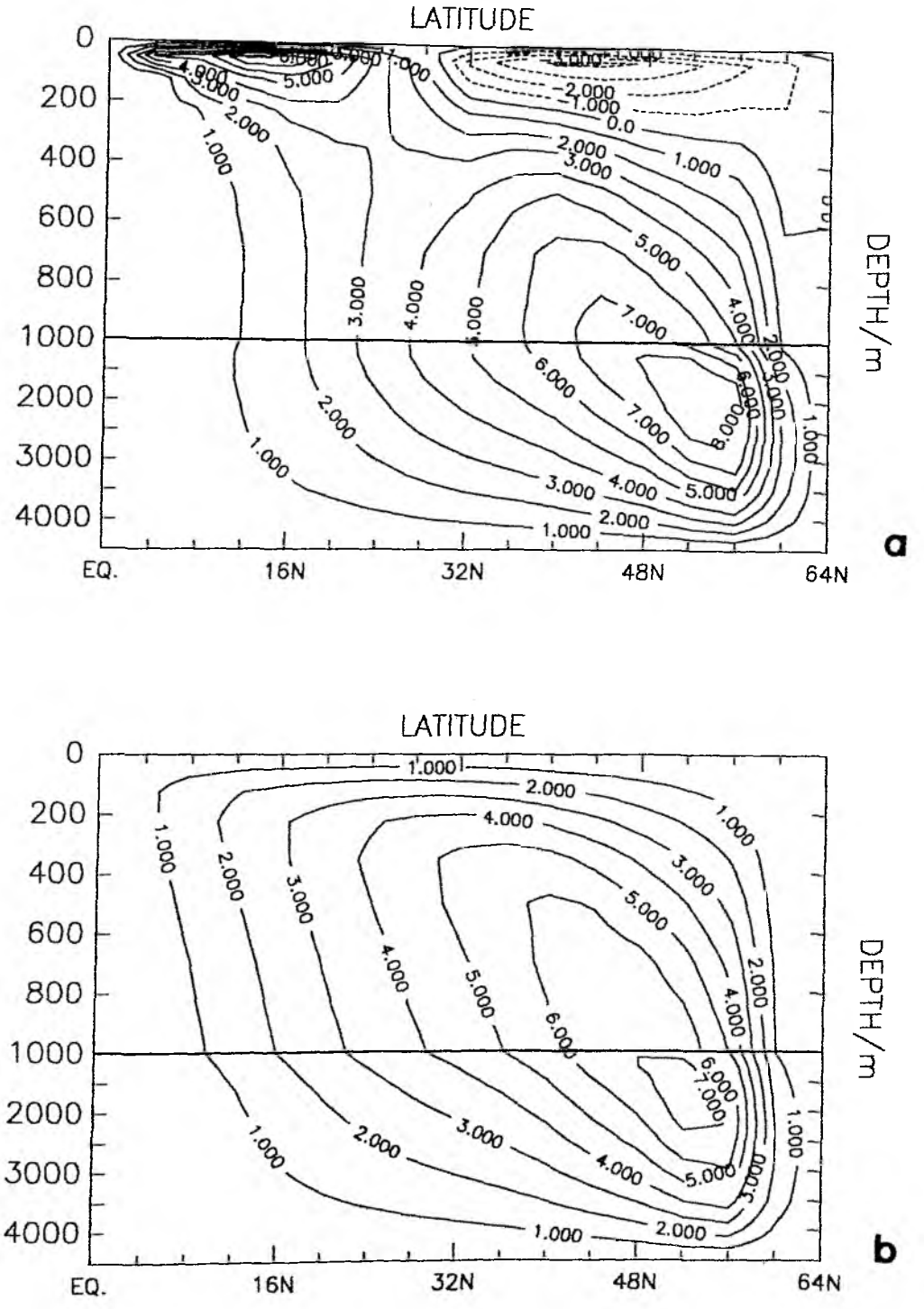

Fig. 4.3: Spin-up steady state of the one-hemisphere GFDL model. Meridional stream function in Sv, positive values denote clockwise circulation, for (a) experiment S1 (with wind) and (b) experiment S2 (no wind).

zonal mean and is associated with transport by horizontal gyres. Figs. 4.4a,b demonstrate that the overturning part (OVT) dominates the total heat transport (SUM) at almost all latitudes.

At high latitudes, there is little difference in total transport between the two cases. This is also visible in the surface heat fluxes (Figs. 4.2a,b), indicating very similar convective heat losses. At low latitudes, however, the wind influence substantially increases the overturning transport, via the aforementioned shallow Ekman-cells. The westerlies have little influence, since north of 32°N the zonally averaged temperature hardly varies in the top 200 m. The "trade winds", however, cause a return flow at a temperature that is about 7°C lower than at the surface, and attributing the shallow, purely wind-driven cell a strength of 5 Sv yields an associated heat transport of 0.15 PW, a value that qualitatively accounts for the difference between wind-driven (S1) and no-wind (S2) case at low latitudes.

The spatial structure of (P-E) as diagnosed from the steady states is opposite to that of the heat flux (see Figs. 4.2a,b). (P-E) has two maxima one of which is over the western boundary current, where salty water is advected northward and forced to receive freshwater because of the Newtonian flux condition. In reality, there is high evaporation in this area, so one would expect (P-E) to have a minimum there. The other maximum is in the northeastern part where convective activity is strongest. This is due to the fact that at high latitudes poleward movement is most pronounced in the eastern part of the basin, in accordance with the results by COX and BRYAN (1984). Despite the unrealistic spatial structure, the zonally averaged freshwater fluxes have reasonable values (Figs. 4.5a,b). (P-E) takes on larger absolute values in the wind-driven case, and the zone of net evaporation is more confined to the equatorial regions.

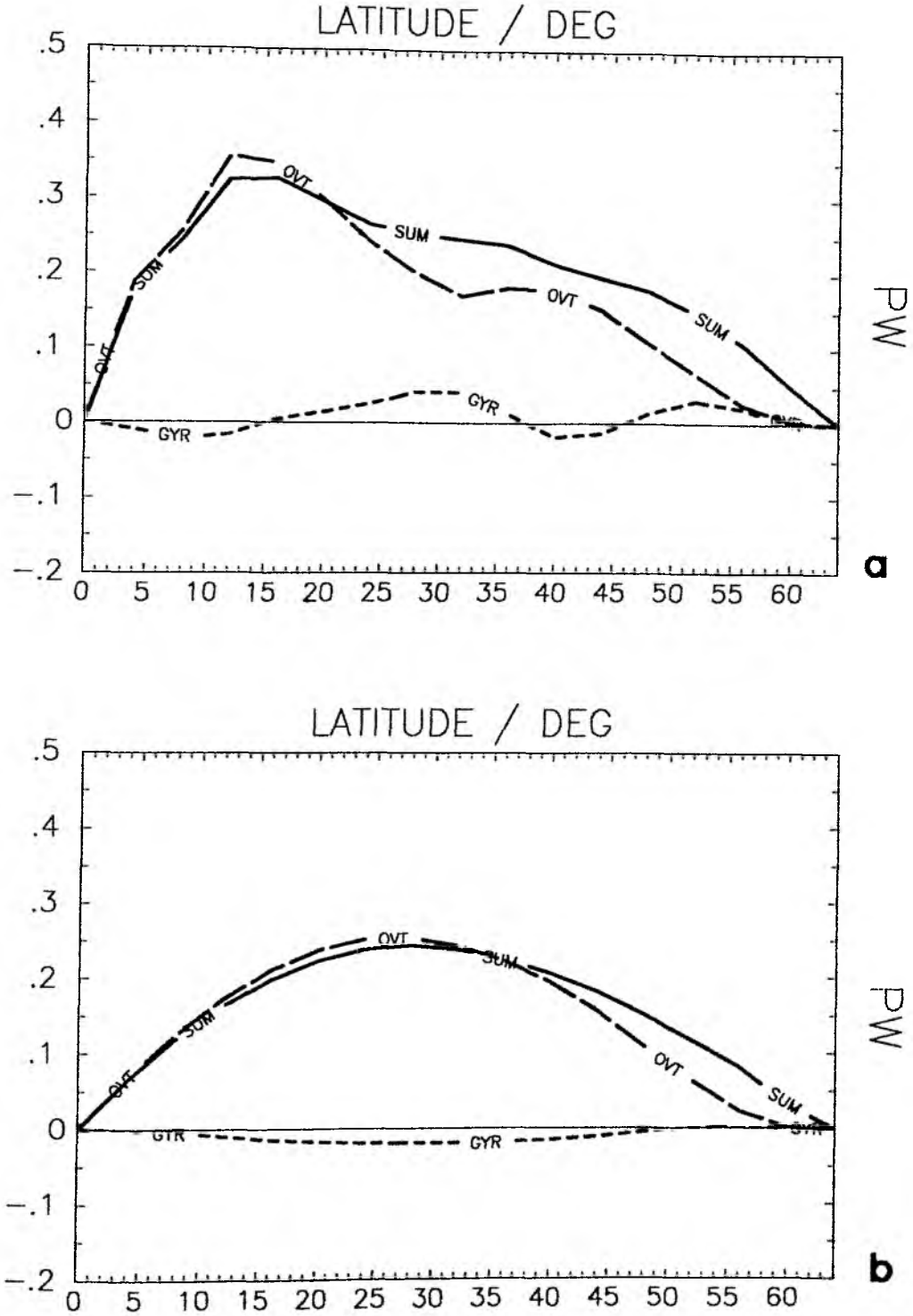

Fig. 4.4: Spin-up steady state of the one-hemisphere GFDL model. Northward heat transport in PW, SUM: total transport, OVT: overturning part, GYR: gyre part, for (a) experiment S1 (with wind) and (b) experiment S2 (no wind).

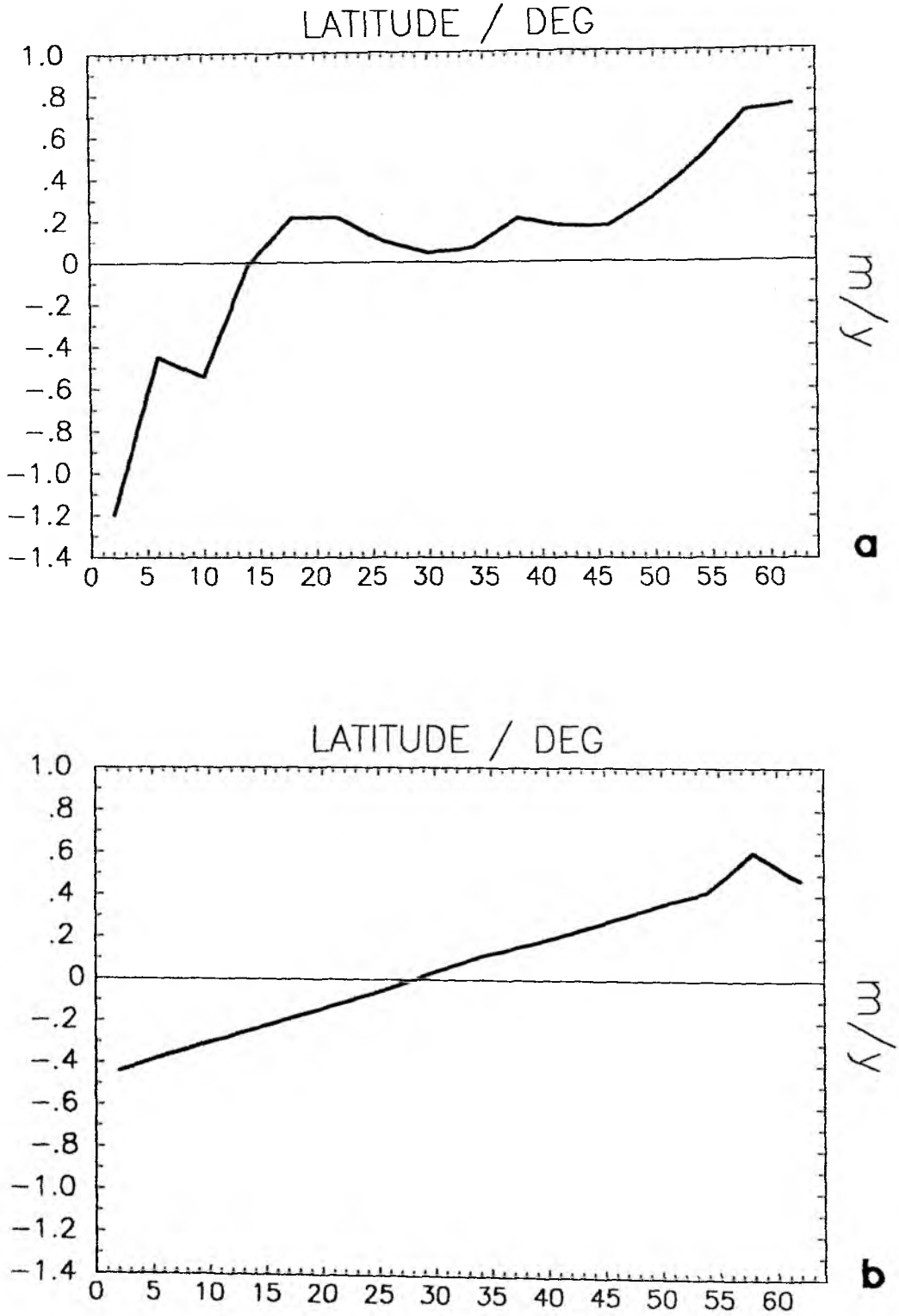

Fig. 4.5: Spin-up steady state of the one-hemisphere GFDL model. Zonally averaged freshwater flux (P-E), in m/y, for (a) experiment S1 (with wind) and (b) experiment S2 (no wind).

4.4 Instability of the Spin-up States

The results from the simple models suggest that the states obtained by the spin-up may be only marginally stable: assuming the thermal expansion coefficient α to be $(1.5 - 2) \cdot 10^{-4}\ K^{-1}$, a kind of mean value of the oceanic range, and the haline expansion coefficient β as $0.8 \cdot 10^{-3}$ one gets an estimate of $\delta = \frac{\beta \Delta S}{\alpha \Delta T}$ of 0.4 to 0.5, using as ΔT and ΔS the amplitudes of the restoring fields, which for experiments S1 and S2 are $27^{0}C$ and 2.5 psu, respectively. If we may classify the 3-D equilibria according to Fig. 2.2, there is thus a chance that it corresponds to the unstable point 2. Even if that is not the case the salinity flux is close to the critical value, and the positive circulation unlikely to be maintained even under modest perturbations, as the box model results from Section 2.4 show.

The stability of the equilibria S1, S2 and S3 (see Table 1) is tested in the following manner: They are used as initial conditions for a series of experiments, in which mixed boundary conditions are applied. Simultaneously with shifting over to mixed boundary conditions, an initial salinity anomaly S' is added to the spin-up.

The experiments are summarized in Table 2: Generally, the "W"-experiments include wind forcing and the "NW"-experiments do not. Initial states and freshwater fluxes are named according to Table 1. The anomalies S' for the different experiments are added to the top layer north of $32^{0}N$, in all cases. Integration time and the time step were chosen such that during rapid changes of the circulation patterns a synchronous integration (time step 2 hours) was performed to gain maximum accuracy. In several cases an asynchronous integration was subsequently employed to finally approach a steady state.

Table 2: Stability Experiments with the One-Hemisphere GFDL Model

Experiment	Initial State	P-E from:	S'/psu	Wind Stress Present?	Integration Time/years
W1	S1	HS1	0.0	yes	182
W2	S1	HS1	+0.01	yes	137 + 2738 a
W3	S1	HS1	-0.01	yes	274 + 5476 a
W4	S1	HS1	-10^{-4}	yes	44
W5	S1	HS1	-10^{-6}	yes	44
W6	S1	<HS1>	-0.01	yes	91 + 1369 a
W7	S3	HS3	-0.01	yes	91
NW1	S2	HS2	0.0	no	1369 a
NW2	S2	HS2	-0.01	no	91
NW3	S2	HS2+5%	-0.01	no	22000*
NW4	S2	HS2+5%	-0.01	no/yes	942*

<HS1> : zonal average of HS1
HS2+5% : P-E from HS2, multiplied by 1.05
S' : initial salinity perturbation, applied in the top layer north of 32°N
a : asynchronous integration, time step 5 days
* : several shifts between synchronous and asynchronous (time step 1 day) integration
no/yes : wind stress was switched on after 342 years

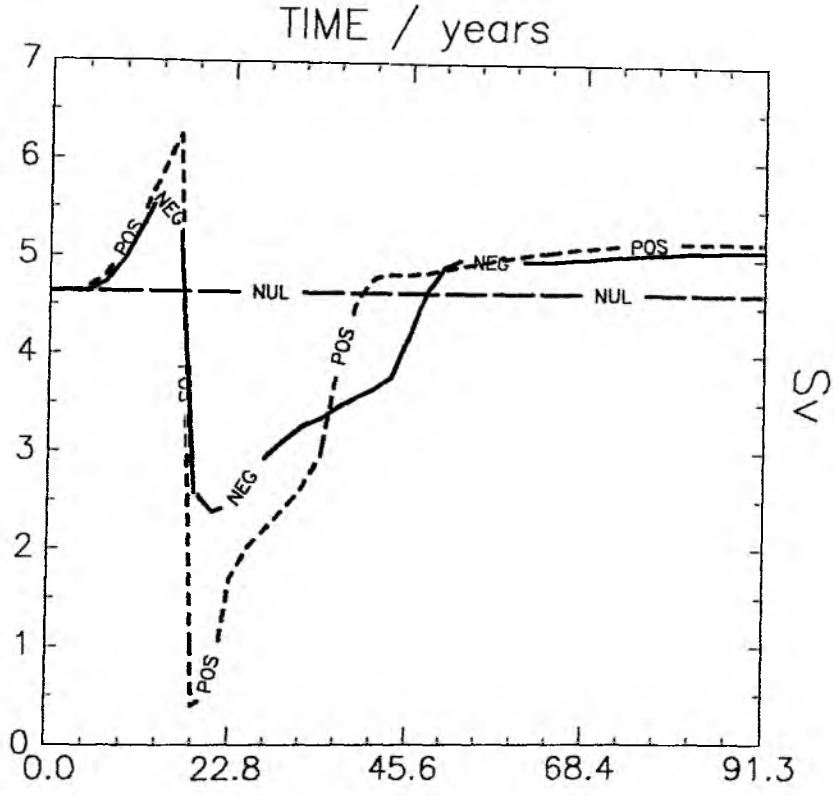

Fig. 4.6: Time series of the meridional stream function at 32°N, 700 m depth, for experiments W1 (NUL), W2 (POS) and W3 (NEG). The anomalies applied are: no anomaly (W1), +0.01 psu (W2) and -0.01 psu (W3).

Two experiments were performed in which the boundary conditions were merely shifted over to mixed ones, i.e., exactly the spin-up states were taken as initial conditions. The wind-driven case W1 was integrated synchronously for 182 years, the no-wind case NW1 asynchronously for 1369 years. In neither case any change occurred, which is due to the different convective adjustment scheme used, as compared to F. BRYAN (1986a,b), and which leads to a more regular convective activity (see Chapter 6), thereby removing the trigger for the halocline catastrophe.

However, the stability behaviour changes drastically if a small salinity anomaly is added to the spin-up, simultaneously with shifting to mixed

boundary conditions. Fig. 4.6 shows the time series of the meridional stream function value at 32°N latitude and 700 m depth. It comprises 91.3 years of synchronous integration, for three different experiments: no anomaly (W1), +0.01 and -0.01 psu anomaly in the top layer north of 32°N (W2 and W3, respectively). Without anomaly nothing happens, but both positive and negative anomalies first trigger an increase in overturning, followed by a rapid collapse occurring within two years, for both anomalies (note that in Fig. 4.6 the sampling rate is once in 2.3 years, so differences in the curves can be due to undersampling). Subsequently the circulation is re-established within about twenty years and settles at a value which is somewhat higher than the initial one.

What happens initially is that convection stops in the regions where surface salinity is reduced. Once this has started the residence time of water parcels at the surface of high latitudes is increased. Thus, they are longer exposed to the net surface freshwater input which further reduces their salinities, providing for a positive feedback. Initially, a positive anomaly causes increased convective activity, as identified from net heat loss of the whole basin in experiment W2, but soon convection is interrupted, accompanied by net heat gain which amounts to about 4-5 Wm^{-2} on average.

In the light of relating overturning strength to meridional density differences the initial intensification visible in Fig. 4.6 is counter-intuitive, since it is associated with a rapid increase of salinity contrast between high and low latitudes. A closer inspection of the time development of experiment W2 (small positive anomaly) reveals the cause for this behaviour. Fig. 4.7 shows that the freshening starts in the northeastern part of the basin, because (P-E) is maximum there. The sharp halocline causes a northwestward geostrophic surface current, tending to spread the halocline westward. A strong density difference exists between the eastern and western boundaries, leading to a simultaneous amplification and northward shift of the overturning maximum. The front reaches the western boundary after 11 years, surface densities become too low and deep water formation is closed off in the area adjacent to the northern boundary. Fig. 4.8 shows that the movement of the halocline is followed by changes in

overturning strength after about five years. The low salinity region spreads further south, mainly in the west, leading to cessation of deep water formation and a reduction in southward freshwater transport. This creates a halocline at about 44°N in the western part of the basin which causes an almost complete collapse of the thermohaline circulation (Fig. 4.9a).

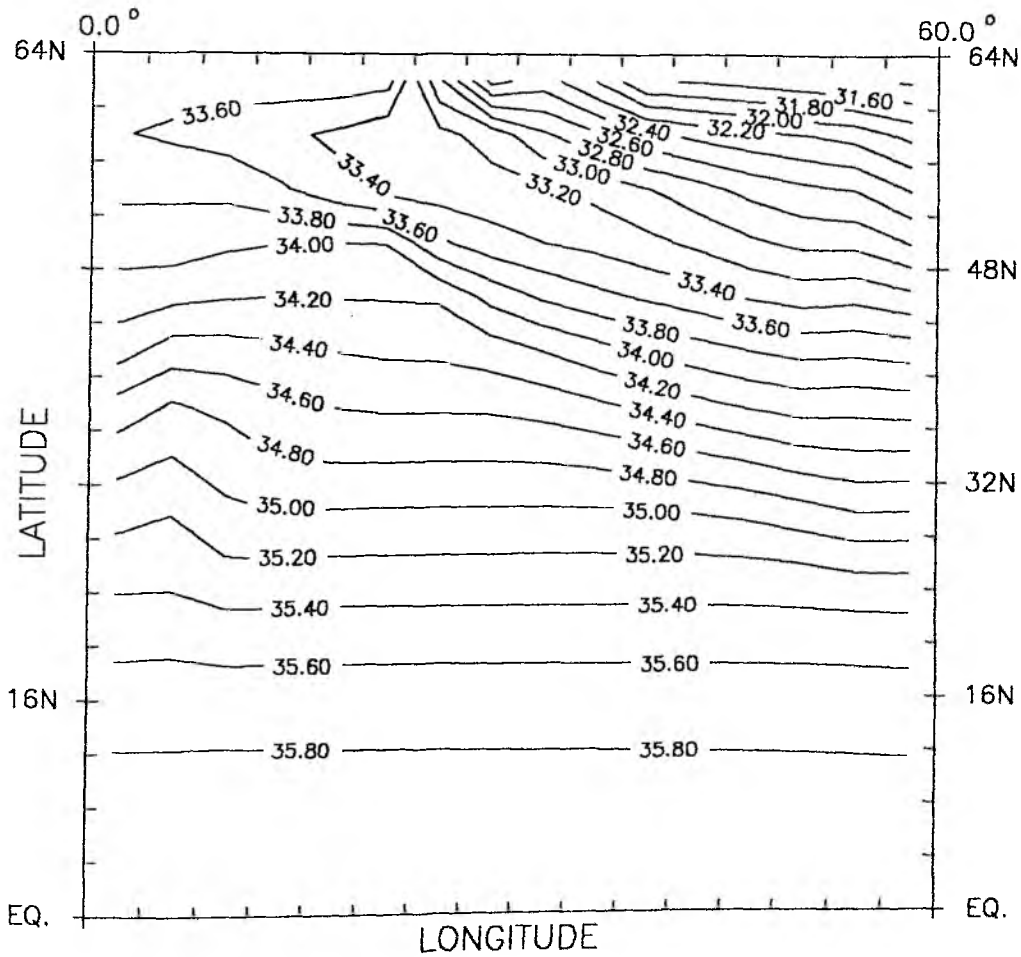

Fig. 4.7: Surface salinity in psu at year 9 of experiment W2 (+0.01 psu salinity anomaly).

To explain the re-establishment of the thermohaline circulation, evident from Fig. 4.8, we consider the meridional freshwater transport of the state depicted in Fig. 4.9a (experiment W2).

Due to wind influence the southward freshwater transport is maintained (Fig. 4.9b), although reduced to half its original strength. Both Ekman cells now provide for substantial transport, the northern one due to the southward movement of very fresh surface water. At mid-latitudes the gyre transport has doubled its intensity, as compared to the initial state. These transport mechanisms prevent an even more extreme freshening of the high latitude surface waters: Along the western boundary salty water is brought back to the north and the zonal salinity gradient at high latitudes is re-established, accompanied by increasing overturning strength (Year 30 in Fig. 4.8).

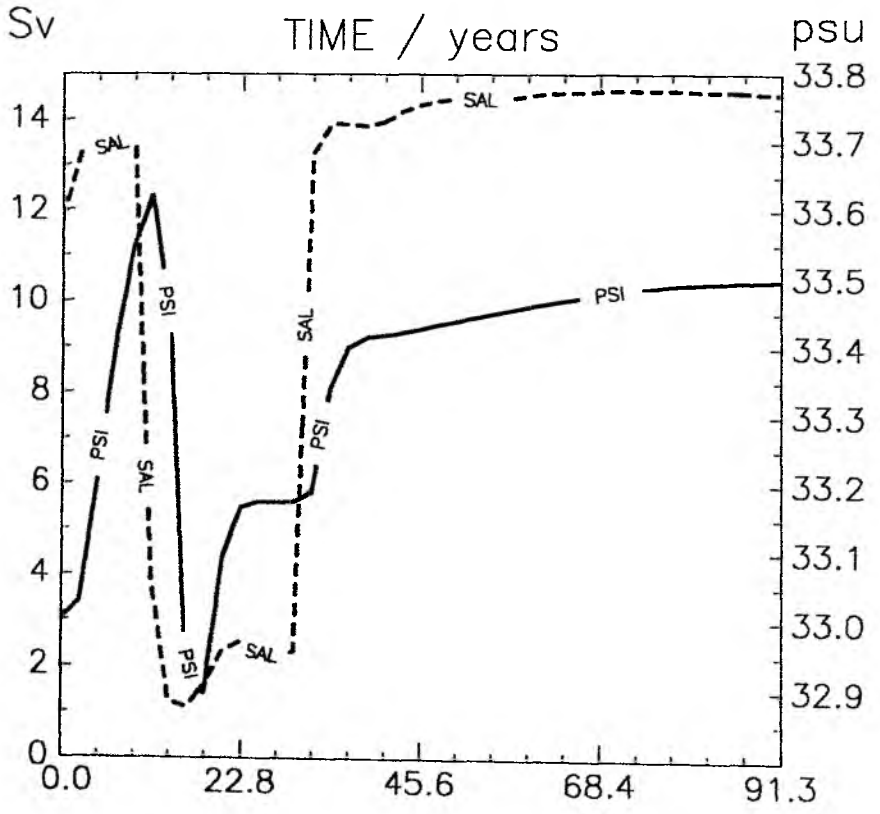

Fig. 4.8: Time series of the meridional stream function at 56°N, 700 m depth (solid curve) and surface salinity at 62°N, 13.1°E (dashed curve), for experiment W2 (+0.01 psu anomaly).

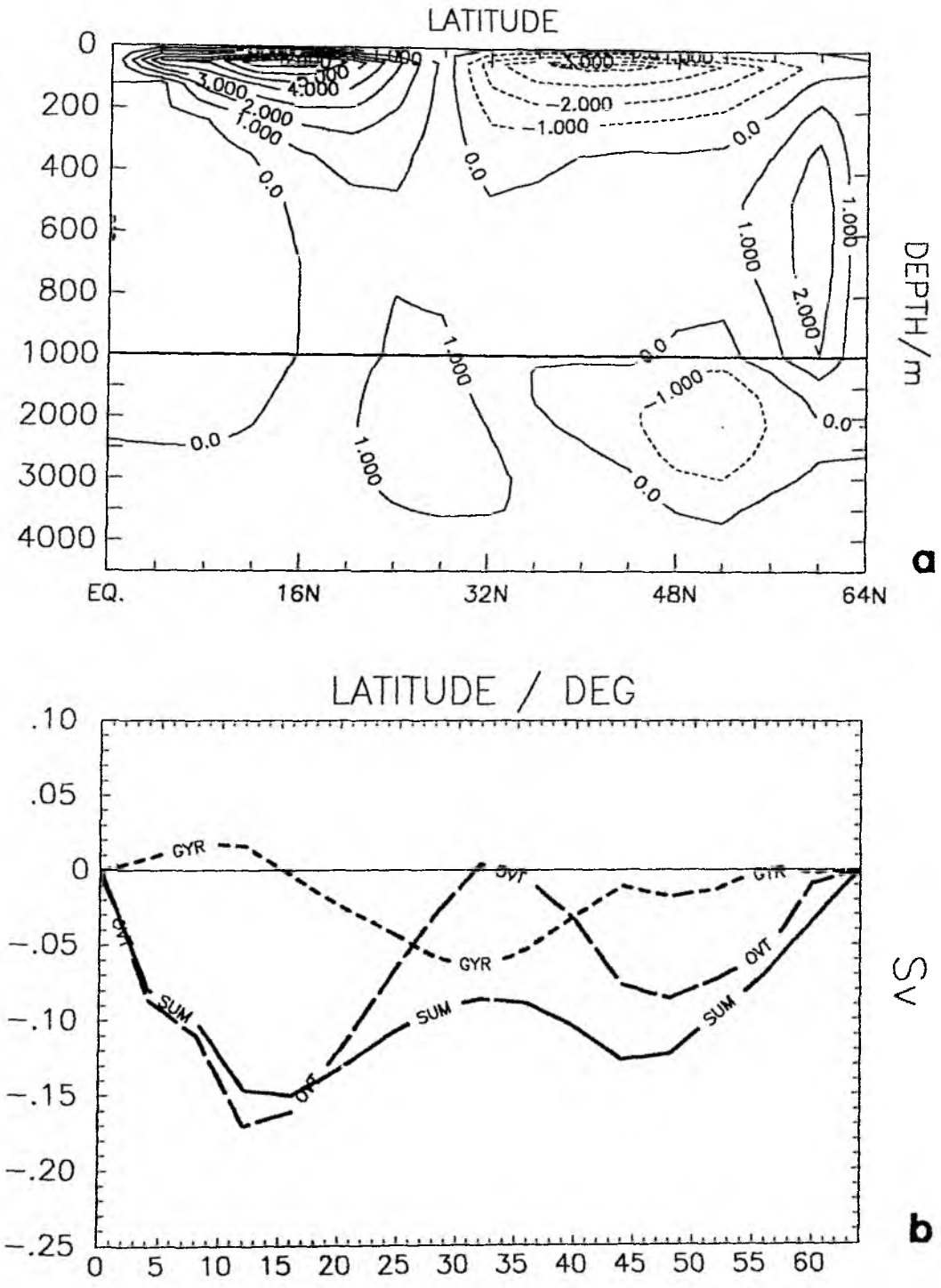

Fig. 4.9: Meridional stream function in Sv (a) and northward freshwater transport (b) at year 18 of experiment W2 (+0.01 psu anomaly). In (b) SUM denotes total freshwater transport, OVT and GYR overturning and gyre parts, respectively.

The adjustment of the interior density and thus flow fields to changes in the deep water production rate is explained as follows. KAWASE (1987) shows that the establishment of deep ocean circulation driven by deep water production occurs through a Kelvin wave propagating southward along the western boundary, then eastward along the equator, then northward, radiating off Rossby waves during the latter period. The resolution in my model exceeds the internal radius of deformation by almost an order of magnitude, nevertheless Kelvin waves are present, albeit very poorly represented (strongly damped, phase velocity reduced to one tenth, DAVEY et al., 1983; HSIEH et al., 1983; WAJSOWICZ and GILL, 1986). The reaction of the mid-latitude meridional overturning to changes in deep water production occurs on the time scale of first mode baroclinic Rossby waves, i.e., several years, as is visible from the time lag between the stream function at 32°N (Fig. 4.6) and the propagation of the halocline (Fig. 4.8).

During the subsequent time development, the experiments W2 and W3 which differ only by initial conditions converge to the same final state. For experiment W3, a long-term integration was performed, comprising a total of 274 years of synchronous and 5476 years of asynchronous integration. The final state is displayed in Figs. 4.10a,b. The surface salinity reflects the strong zonal dependence of the freshwater input. Deep water formation is confined to the northwestern corner, maximum overturning strength is about 12 Sv, an increase of 35% compared to the spin-up. However, the meridional heat transports are almost identical, differences are visible only in the partitioning between overturning and gyre parts at high latitudes.

A series of further experiments was performed to see if the collapse of the thermohaline circulation is a special feature of the experiments W2 and W3. In W4 and W5 (see Table 2), the amplitude of the initial salinity anomaly is reduced to 10^{-4} and 10^{-6} psu, respectively, applied in the top layer north of 32°N. The latter case remains stable, in the former the halocline catastrophe occurs.

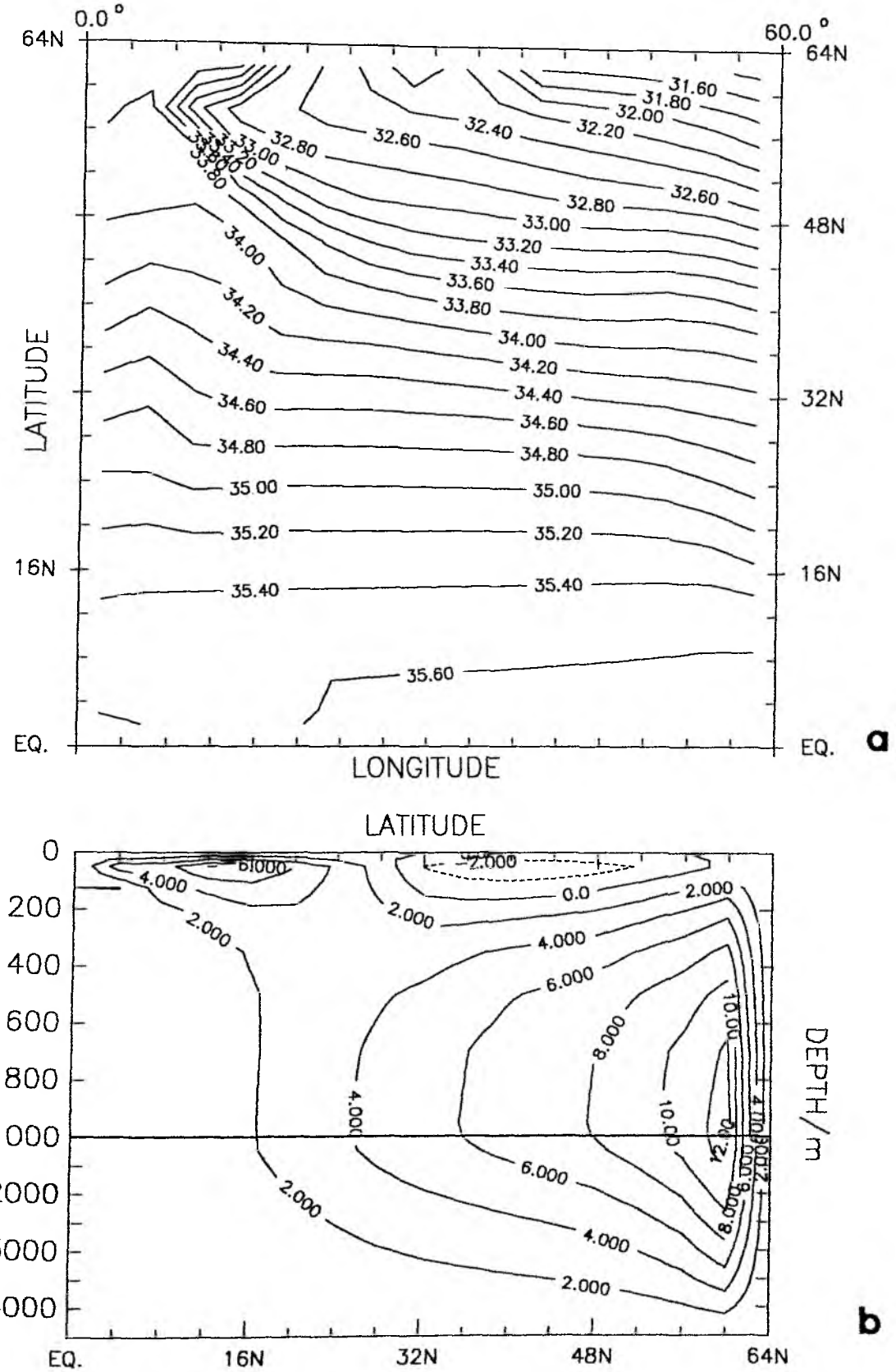

Fig. 4.10: Final state of experiment W3 (wind-driven, -0.01 anomaly). Surface salinity in psu (a) and meridional stream function in Sv (b), where positive values denote clockwise circulation.

The precise time development of the breakdown (e. amplification of the overturning) was shown to depend (E-P) forcing. To test this further, E-P was varied in e freshwater fluxes diagnosed from the spin-up are averaged prescribed as boundary conditions. Again, an anomaly of the circulation to collapse temporarily, then the re-established. The meridional stream function of the fir resembles the spin-up S1, but deep water production is northeastern region.

In experiments S3 and W7 it is tested if the stability box models can actually be applied. S3 is spun up with apparent atmospheric temperature as in S1 (see Fig. 4.1), S_* of the restoring salinity field is reduced to 1.5 p reduction of the parameter $\delta = \frac{\beta\Delta S}{\alpha\Delta T}$ to approximately 0.25 fluxes HS3 are diagnosed from S3, and an anomaly of -0. Again, the halocline catastrophe follows, meaning th considerations from the box models (see Fig. 2.2) are not model.

Wind stress is not important for the occurrence c catastrophe, as experiment NW2 shows. An anomaly of -0.01 spin-up S2, leads to the collapse of the meridional overt happens if (P-E) is multiplied by a factor of 1.05 (ex NW4).

We conclude that under salinity perturbations of amplit larger, the halocline catastrophe occurs in all cases, years. Convection eventually stops everywhere, the detail depend on the specific parameters of the experiment (f initial anomaly), likewise the extent of the breakdown, cases is as marked as in experiment W2 (Fig. 4.9a). For pr the anomalies applied are infinitesimally small, campared the "great salinity anomaly" of the mid-seventies (DICKSO

The precise time development of the breakdown (e.g., the initial amplification of the overturning) was shown to depend on details of the (E-P) forcing. To test this further, E-P was varied in experiment W6. The freshwater fluxes diagnosed from the spin-up are averaged zonally and then prescribed as boundary conditions. Again, an anomaly of -0.01 psu causes the circulation to collapse temporarily, then the overturning is re-established. The meridional stream function of the final state strongly resembles the spin-up S1, but deep water production is confined to the northeastern region.

In experiments S3 and W7 it is tested if the stability analysis from the box models can actually be applied. S3 is spun up with wind stress and apparent atmospheric temperature as in S1 (see Fig. 4.1), but the amplitude S_* of the restoring salinity field is reduced to 1.5 psu. This means a reduction of the parameter $\delta = \frac{\beta \Delta S}{\alpha \Delta T}$ to approximately 0.25 to 0.3. The (P-E) fluxes HS3 are diagnosed from S3, and an anomaly of -0.01 psu is added. Again, the halocline catastrophe follows, meaning that the stability considerations from the box models (see Fig. 2.2) are not valid for the 3-D model.

Wind stress is not important for the occurrence of the halocline catastrophe, as experiment NW2 shows. An anomaly of -0.01 psu, added to the spin-up S2, leads to the collapse of the meridional overturning. This also happens if (P-E) is multiplied by a factor of 1.05 (experiments NW3 and NW4).

We conclude that under salinity perturbations of amplitude 10^{-4} psu and larger, the halocline catastrophe occurs in all cases, within 20 to 30 years. Convection eventually stops everywhere, the details of the collapse depend on the specific parameters of the experiment (freshwater fluxes, initial anomaly), likewise the extent of the breakdown, which not in all cases is as marked as in experiment W2 (Fig. 4.9a). For practical purposes, the anomalies applied are infinitesimally small, campared to phenomena like the "great salinity anomaly" of the mid-seventies (DICKSON et al., 1988).

In all wind-driven cases, convective activity and the meridional circulation are re-established approximately 20 years after the collapse, due to wind-driven salt transport (see Fig. 4.9b). The final states qualitatively resemble the initial one.

Therefore, in the light of the classification according to the box model equilibria, initial and final states correspond to the same solution. The main difference lies in the much stronger confinement of convective activity to small areas, for the final states. Where these areas are depends on the details of the (E-P) forcing, but generally convective overturning in conjunction with mixed boundary conditions causes the surface fields to show much more small-scale structure. The collapse of the meridional overturning must thus be viewed as a feature marking the transition from large-scale to small-scale convective activity.

The crucial role of wind stress for convection to start again is confirmed by the time development of the no-wind case (NW3). Once the thermohaline circulation has collapsed the only efficient meridional transport mechanism is closed off. High-latitude surface salinities keep on decreasing, until a stage is reached which corresponds to the inverse circulation found in the box and 2-D models. The salinity contrast between high and low latitudes is almost 8 psu, the meridional overturning very sluggish (maximum 1.6 Sv) and directed towards the equator at the surface. However, this state does not remain stable, and its properties and further development will be discussed in detail in the next section. Turning on wind stress at an intermediate stage (after 342 years, NW4) results in the same steady state as for the wind-driven case, demonstrating that transports brought about by the inverse circulation are easily matched by the wind influence.

4.5 Instability of the Inverse Circulation

In the no-wind case, the thermohaline circulation is not re-established after the initial breakdown, since the surface freshwater input at high latitudes cannot be removed efficiently enough. Figs. 4.11a,b display the situation 6950 years after the begin of experiment NW3: Extremely large surface salinity gradients (almost 8 psu) cause an inverse thermohaline circulation, with surface flow directed southward, and very small intensities.

Sinking occurs at the equator, but only to shallow depths, the poleward flow at mid-depths (200 - 700m) transports heat and salt northward. Combined with diffusion this leads to a warm (about 14°C) and salty deep ocean. Horizontal density variations are smaller than 0.4 kg/m^3, surface densities are highest at the equator. Apart from variations at the surface, the tracer fields are almost zonally constant.

It shold be mentioned that the experiment described here is run with E-P enlarged by 5% compared to the spin-up, which is due to a code error in the diagnosis of the freshwater fluxes. The initial salinity anomaly was again -0.01 psu in the top layer north of 32°N. As the time step had to be reduced to one day due to the strong salinity gradients, total computer time used for experiment NW3 amounted to about 100 hours on a CRAY-XMP, for the 22,000 ocean years, and the experiment was not rerun after the error was detected. This is justified because the 5% difference did not cause any significant changes in the initial instabilities (see Section 4.4, experiment NW2).

The situation depicted in Figs. 4.11a,b appears like an equilibrium, the basin averaged heat uptake being 0.2 W/m^2, approximately. However, the steady warming of the deep ocean, manifesting itself in the warm, salty tongue at mid-depths, creates a preconditioning for the most bizarre phenomenon observed during this study. It is explored by performing a synchronous integration of this period, starting at year 6941.

There is still a surface western boundary current, though with only 2 cm/s speed, which advects salt northward and increases surface density with time. At about 40°N there is an intermediate maximum in surface density, because further north the thermal expansion coefficient has too low a value to compensate the effect of decreasing salinity. The density difference between the two uppermost layers is only 0.01 kg/m^3. Right there, convection starts shortly after the situation depicted in Figs. 4.11a,b, mixing the two uppermost layers. This small event gives rise to ever growing convective activity: The negative vertical salinity gradient at middle and high latitudes stabilizes the water column until convection homogenizes temperature and salinity vertically. Heat is rapidly given off to the atmosphere, whereas

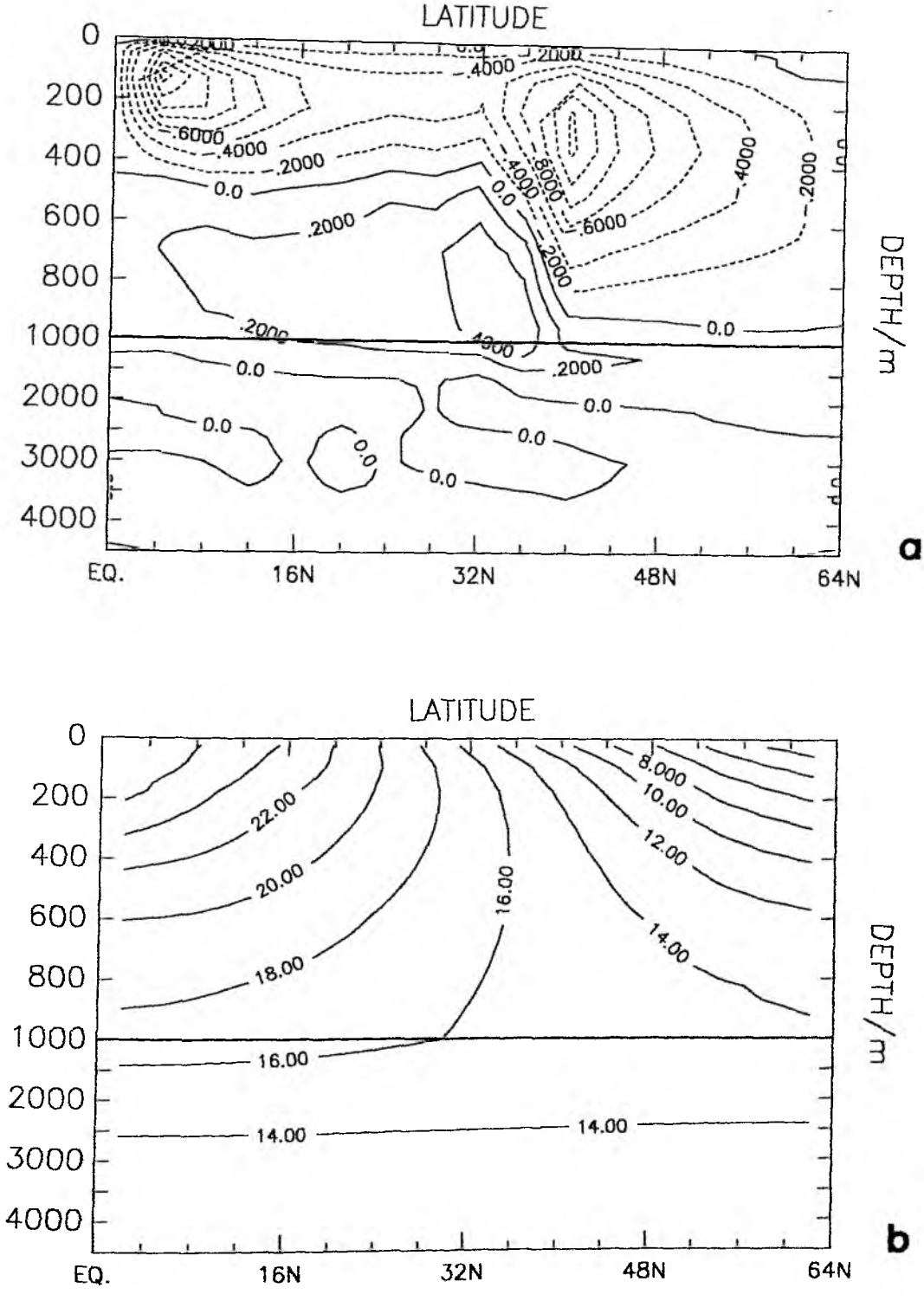

Fig. 4.11: Inverse circulation at year 6950 of experiment NW3 (no wind). (a) Meridional stream function in Sv, positive values denote clockwise circulation, (b) meridional section of temperature in °C, along the western boundary.

no fast process exists to lower surface salinities again. Resulting is a strong density input at the surface, convection will reach further down, until the column is completely homogenized.

Starting at 40°N at the western boundary, the convective area spreads northeastward (Fig. 4.12a). The sharp halocline (4 psu over 1000 km) in conjunction with vertical isopycnals west of it (meaning extreme horizontal density gradients) cause strong northward surface currents and an immensely violent thermohaline circulation (Fig. 4.12b). Fig. 4.13a shows that during this phase the spatially averaged heat loss reaches 130 W/m^2, overturning strength at 56°N, 1250 m depth is 150 Sv at its maximum.

The strongly convective phase lasts for about 100 years, during which time the deep ocean gives off all the heat it had accumulated in the 7000 years before. However, the process does not occur monotonously (Fig. 4.13a). The heat loss shows strong oscillations with a period of about 20 years, coherent with overturning variations of an amplitude of more than 80 Sv. The meridional stream function drops to -70 Sv, meaning extremely strong inverse circulation, with surface flow directed equatorwards.

Whereas the "Advent of the Strong Convection" resembles the phenomenon observed in the 2-D case (Section 3.2), and the explanations given here are in fact valid also for the 2-D model, the appearance of the strong oscillations is a novel feature and deserves closer consideration. Firstly one observes from Fig. 4.13b that not simply variations in high-latitude salinity are responsible for the oscillations, as assumed before (MAROTZKE, 1989). Zonally averaged salinity jumps from 30 to 34 psu, to remain almost constant for 700 years, whereas temperature strongly varies, despite the coupling to the surface heat flux. Initially it is in phase with the overturning strength, since rising zonally averaged SST is associated with the propagating halocline (remember that the stronger the convective activity, the higher is the SST). Opposed to this, the surface western boundary current intensity is time-lagged by 7 years at the onset of the convective period, for later to be almost in phase with overturning strength.

The oscillations are explained as follows: Initially, the increasing overturning strength is brought about by the geostrophic currents at the

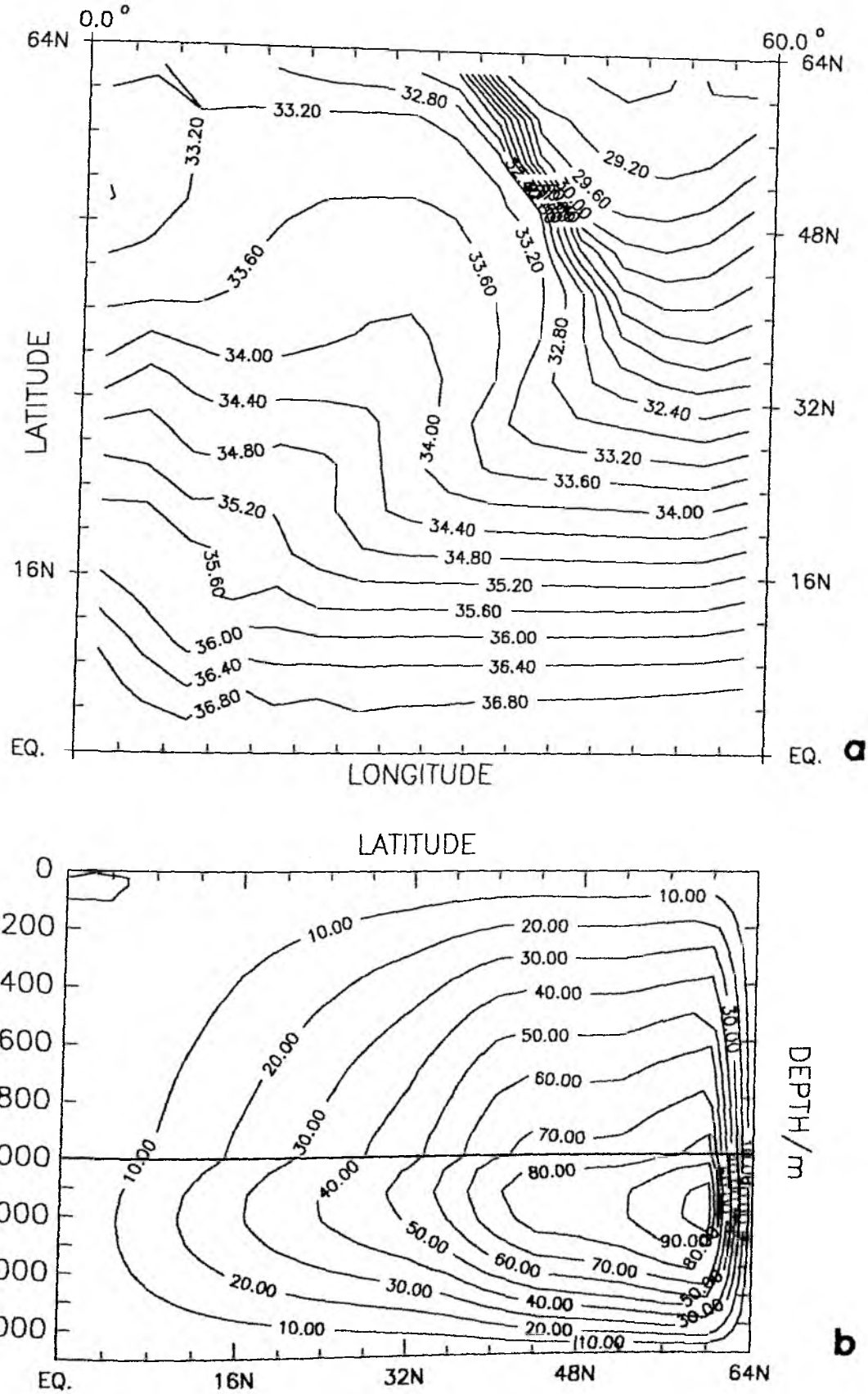

Fig. 4.12: Surface salinity in psu (a) and meridional stream function in Sv (b), at year 6959 of experiment NW3 (9 years after the state displayed in Fig. 4.11). The circulation is clockwise.

halocline. It takes several years until the interior fields have adjusted to the increased deep water formation rate. The deep western boundary current transports dense water from the northern deep water formation sites to the mid-latitudes. Since isopycnals are almost vertical at middle and high latitudes, pressure gradients are not only brought about by surface density gradients, as is usually the case, but are to a large extent determined by the deep water density contrasts. The large west-east variation at mid-latitudes gives rise to a maximum in overturning strength of more than 200 Sv.

This situation, however, is not a stable one: The surface western boundary current transports heat northward, pushing the 10^0-isotherm all the way to the northern boundary (Fig. 4.14a). Fig. 4.14b shows that the gyre heat transport reaches almost 4 PW during this period. Eventually, the water transported northward is too warm and light to sink considerably, deep water formation stops and likewise the supply with dense water of the deep western boundary region. As penetrative convection continues in the eastern part of the basin, densities there become larger than in the west, resulting in a reversal of the thermohaline circulation, with a maximum of the inverse cell of more than 80 Sv.

The east-west density gradient is now reversed again: Cooling starts in the northwestern corner due to the reduced intensity of the boundary current. Since the strong gyre heat transport had been accompanied by northward salinity transport, a density maximum is created which propagates downward through convection and then is advected southward. Thus, the strong positive circulation is re-established, and the cycle starts again. At last the deep ocean is cooled sufficiently and the system settles at a state of moderately high overturning strength (about 30 Sv), for finally to undergo a transition similar to the instability of the spin-up state (Fig. 4.13), which again results in a sluggish, inverse circulation.

The further time history is explored by continuing the asynchronous integration for another 14,000 years. Fig. 4.15a displays a high-resolution (the mean over one hundred time steps is sampled) time series of the basin

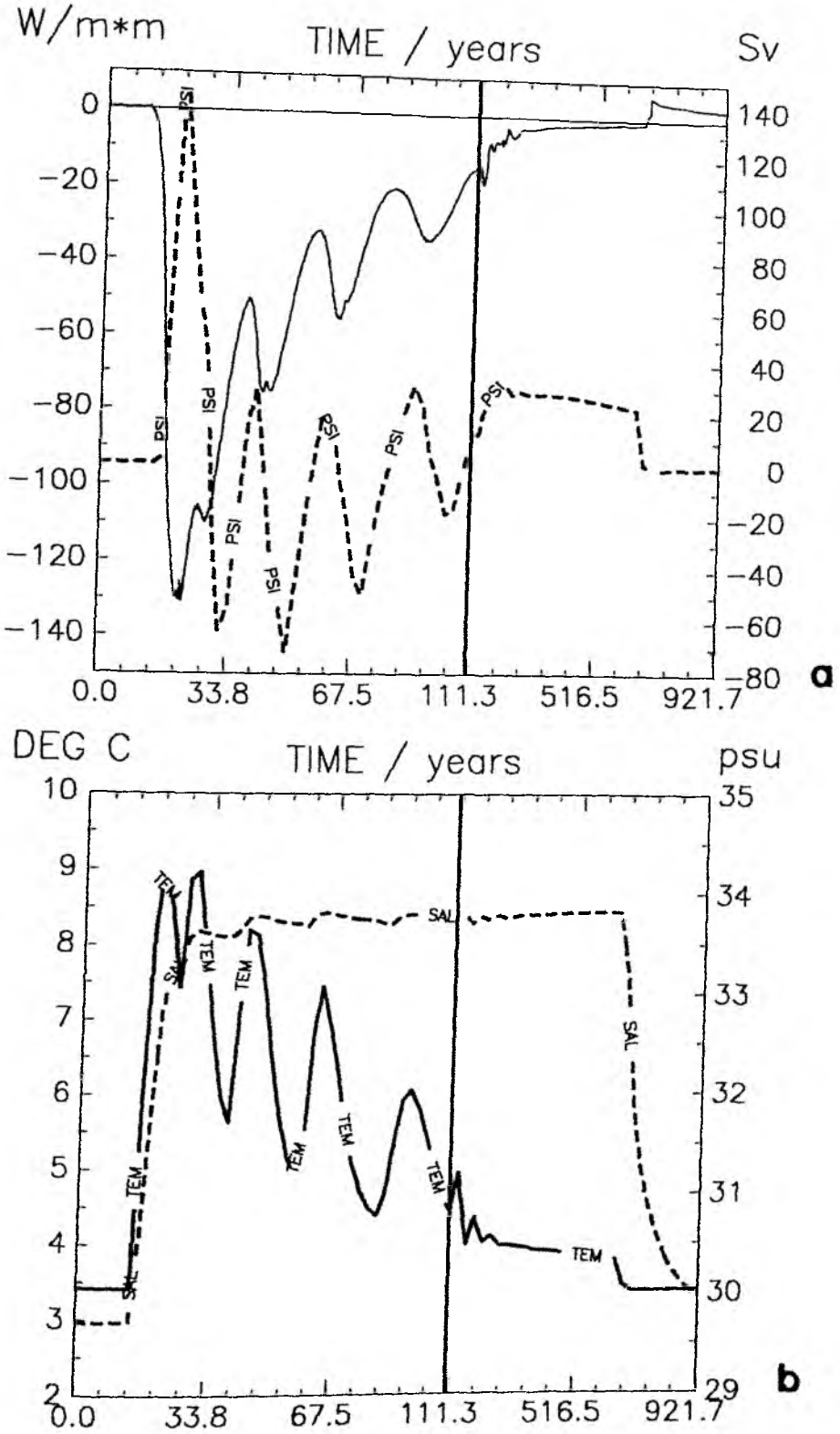

Fig. 4.13: Time series from experiment NW3 during the strongly convective phase. The bold vertical line marks a transition from synchronous to asynchronous integration. Fig. 4.12 is at year 9 of the time axis.
(a) Basin averaged heat uptake (solid curve) in W/m^2 and meridional stream function in Sv at 56°N, 1250m depth (dashed curve).
(b) Zonally averaged surface temperature in °C (solid curve) and zonally averaged surface salinity in psu (dashed curve), at 54°N.

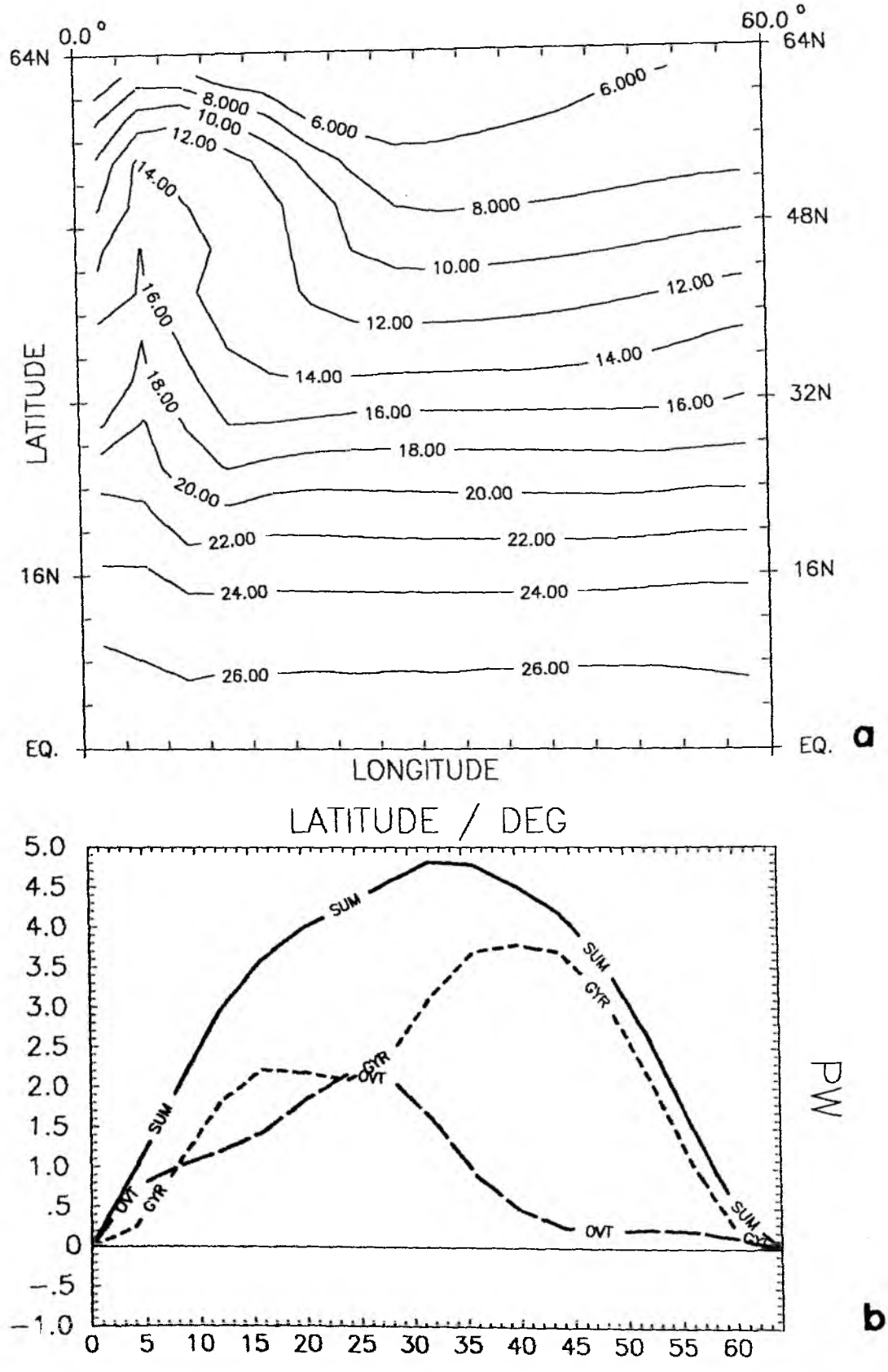

Fig. 4.14: Experiment NW3, year 28 of Fig. 4.13, surface temperature in °C (a) and northward heat transport in PW (b). SUM: total transport, OVT and GYR: overturning and gyre parts, respectively.

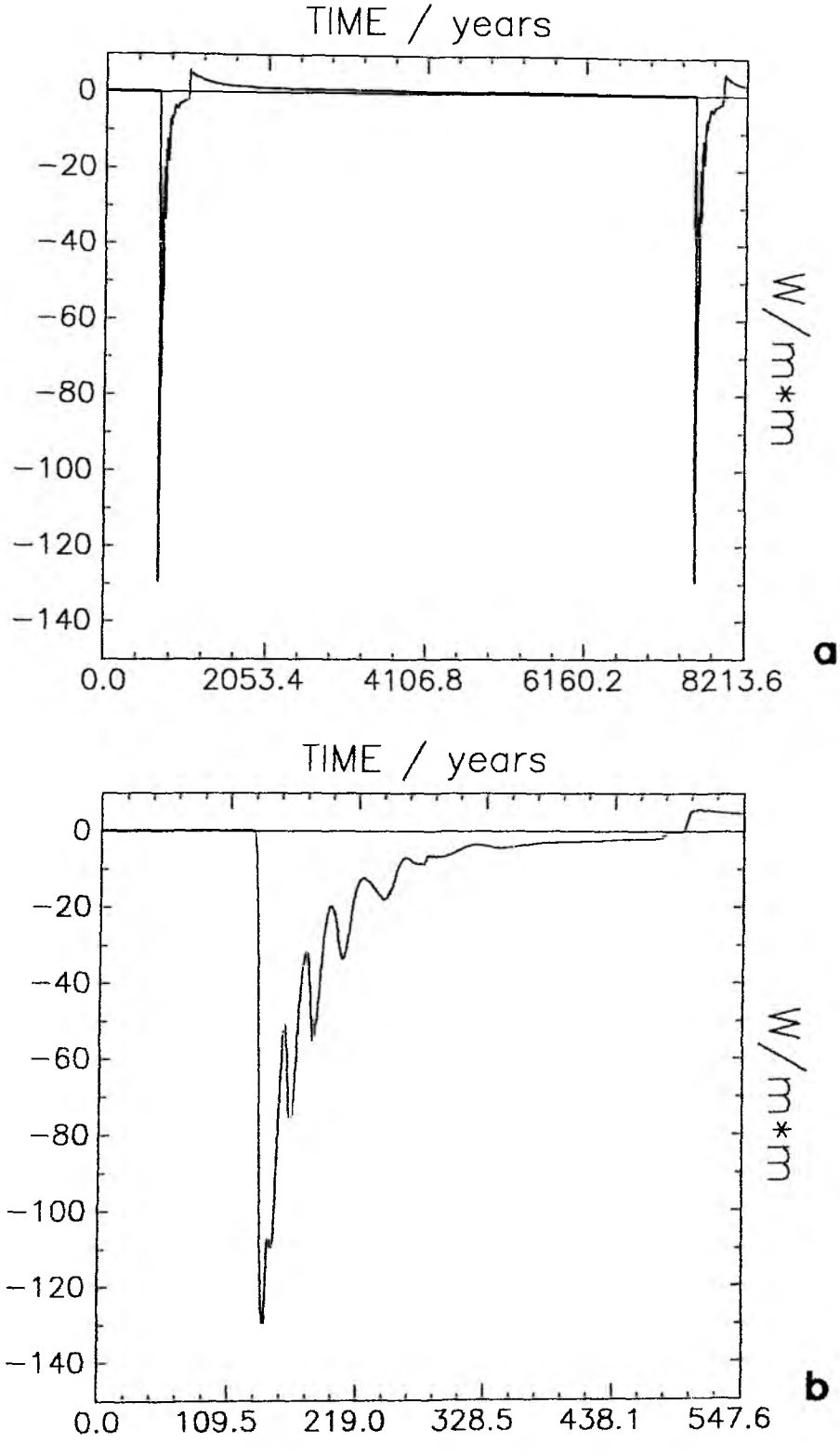

Fig. 4.15: Experiment NW3, time series of basin averaged heat uptake in W/m^2. (a) Starting 5988 years after the end of Fig. 4.13, (b) the first event of 4.15a, shown with a stretched time axis.

averaged heat uptake, during the last 8214 years of the integration. The strong convection returns twice, about 6500 years apart. The details are very similar to the first occurrence (compare Figs. 4.13a and 4.15b), and the two events of Fig. 4.15a are indistinguishable. Like for the 2-D case with convective adjustment, the system is in the inverse state for most of the time, although this is not an equilibrium. The sudden cooling of the deep ocean occurs regularly, and one concludes that no stable solution of the one-hemisphere 3-dimensional model without wind has been found.

5. GLOBAL GFDL MODEL

5.1 Introduction

MANABE and STOUFFER (1988) showed that the coupled GFDL ocean-atmosphere model has two different steady states, one with a relatively warm and salty northern North Atlantic and one with a cold and fresh one. Only in the former case there is a substantial thermohaline circulation in the Atlantic, with sinking at high northern latitudes and an overturning strength of approximately 12 Sv. MAIER-REIMER and MIKOLAJEWICZ (1989) spun up the global Hamburg ocean model with LEVITUS' (1982) surface data for temperature and salinity. Under mixed boundary conditions, an additional freshwater input of 0.011 Sv through the St. Lawrence River caused the Atlantic thermohaline circulation of the spin-up to collapse after 100 years. It remained sluggish and partially reversed thereafter and thus represented a second equilibrium.

The existence of multiple steady states of the global thermohaline circulation is seen to be well confirmed, but no systematic exploration of the possible equilibria of a global 3-D ocean model has hitherto been done. To achieve this is the aim of Chapter 5, "global" meaning here the geometrically simplest 3-D generalization of the two-basin box model depicted in Fig. 2.4. The results from the preceding chapters are used as hints at which equilibria are likely to exist even in the more complex model.

In the box models, each hemisphere of each ocean basin may have two flow directions, yielding a total of 16 equilibria for the global model. Chapter 4 showed how the transition period between two steady states is determined by convective activity in a three-dimensional model. Moreover, Chapter 4 demonstrated that wind influence rules out the inverse circulation for the case symmetric about the equator, at least for a realistic order of magnitude of the freshwater forcing.

Chapter 5 is organized as follows: In Section 5.2, the model configuration is described, and the influence of including the Antarctic Circumpolar Current is discussed in detail. Section 5.3 describes which different

steady states of the global 3-D model could be obtained. Section 5.4 discusses the stability behaviour of some steady states. The sensitivity both to variations in the surface freshwater fluxes and to salinity perturbations is investigated. The response of one global model eqilibrium (with sinking in both Northern Hemispheres) to changes in (P-E) was studied by MEAD (1988), but he did not investigate perturbations that led to a qualitatively different steady state.

5.2 Model Configuration and Spin-up State

The novel feature appearing is the Antarctic Circumpolar Current (ACC) which introduces a fundamental asymmetry between Northern and Southern Hemispheres. Besides, symmetry is maintained as far as possible: The basins have equal width and meridional extension (Fig. 5.1), wind stress and apparent atmospheric temperature are equal in the two oceans and symmetric about the equator. In fact, they are chosen identical to the one-hemisphere case (see Fig. 4.1). I shall henceforth refer to the basin extending from 3.75^0 to 63.75^0 longitude as Pacific, the other as Atlantic, to be definite. It should always be kept in mind, however, that the two oceans are completely interchangeable in the model. In the channel region, periodic boundary conditions are imposed at the zonal boundaries. The width of the channel is specified somewhat arbitrarily to 16^0 latitude, providing for three meridional ocean velocity grid points. The model does not extend southward beyond the gap, so Antarctic Bottom Water is not represented.

To properly predict the zonal transport of the ACC one would have to include bottom topography and explicit representation of eddies (NOWLIN and KLINCK, 1986; WOLFF and OLBERS, 1989). With a flat bottom and coarse resolution, a model would overestimate the ACC transport, as simple scale analysis shows:

The zonal momentum equation (written in cartesian coordinates for simplicity)

$$\partial_t u - fv = -\frac{1}{\rho_0}\partial_x p + A_{MH}(\partial_{xx} + \partial_{yy})u + A_{MV}\partial_{zz}u \qquad (5.1)$$

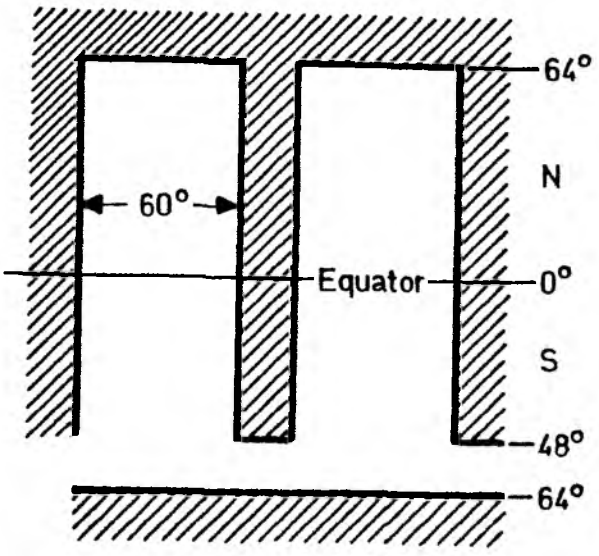

Fig. 5.1: Model domain of the "global" GFDL model.

yields after zonal averaging and vertical integration, for the steady states,

$$\partial_{yy} \langle U \rangle = - \frac{\tau_x}{\rho_0 A_{MH}} \qquad (5.2)$$

where < > denotes zonal average, U is the zonal transport and τ_x wind stress. The pressure term drops out because of cyclic continuity, the time derivative and <V> are trivially zero. (5.2) shows that with given wind stress the ACC transport is solely dependent on horizontal eddy viscosity, a parameter chosen on numerical and not physical grounds, and <U> is thus as uncertain as A_{MH}. A scale analysis of (5.2) with channel width as horizontal length scale and τ_x = 0.1 N/m^2 yields an ACC transport of over 2200 Sv. However, this is misleading, since <U> does not follow an exponential law and obeys homogeneous (no-slip) boundary conditions: Assuming constant τ_x, <U> takes on the form:

$$\langle U \rangle = \frac{\tau_x}{2\rho_o A_{MH}} y(L - y) \qquad (5.3)$$

Integration over the channel gives an additional factor of 1/12, compared to the scale analysis. Actually, MEAD (1988) obtained a factor of 1/6 in a model of similar design. That the reduction is not as strong as indicated by (5.3) may be due to the fact that the ACC is not completely confined to a narrow channel, and on zonal average horizontal dissipation is weaker than implied by (5.3).

One concludes that even with a clear concept of the dominant balance in the simplified model, the zonal transport is far from being well predictable. In order to avoid any additional complications it was decided to specify the ACC transport to a fixed value of 200 Sv. This is still too strong compared to the results from direct measurements, (WHITWORTH and PETERSON, 1985) or inverse models (OLBERS and WENZEL, 1989), both giving about 125 Sv, but within the range between the estimate (5.3) and the one deduced from MEAD (1988). It should be kept in mind that the purpose of including the ACC in this study is to provide for a connection between the two ocean basins, for sake of zonal homogenization. It is clear that ACC dynamics can by no means be represented properly, so the additional error by prescribing its transport is insignificant.

However, one question remains: If normally the transport around the island Antarctica is determined by the model, does a specification of this value render the problem of finding the external mode stream function ill-posed? Actually, this is not the case: The stream function Ψ is calculated by inverting the (elliptic) equation (4.9) for the time rate of change of vorticity, which in turn is obtained by integrating the horizontal equations of motion vertically and taking the curl. If no islands are present, the boundary condition $\Psi = 0$ is employed. The transport around an island, however, is part of the solution of the model and determined by integrating the vertically integrated equation of motion (4.1) around each island (BRYAN, 1969; COX, 1984). In the standard model, the value obtained by this procedure is used as boundary condition in the inversion, but instead we

replace it by an arbitrary value. Thus the inversion of the vorticity equation is still well-posed and properly done, whereas we do not fulfill the momentum equation.

Analogous to the one-hemisphere case, a spin-up was run with Newtonian conditions on both temperature and salinity, the restoring values being identical in the two basins and symmetric about the equator, and again following a cosine law in latitude with amplitudes 27°C and 2.5 psu, respectively (Fig. 4.1).

The spin-up not only serves as initial state for most subsequent experiments, but has some interesting aspects in itself: The aim of this study is to find as many equilibria of the thermohaline circulation as possible, the hypothesis being that there is a maximum of 16 (Section 2.4). Chapter 4 showed that the states including the symmetric inverse circulation (i.e., including a -- in one basin, in the notation introduced in Chapter 2. Remember that + means that surface flow is directed poleward on zonal average, and - that surface flow is equatorward) are ruled out by wind influence, because the inverse circulation is too weak to match wind-driven transports. The number of possible equilibria is thus reduced to nine (see, e.g., Fig. 2.6), five of which have circulations symmetric about the equator, at least in one basin (++++, -+++, +++-, +-++, ++-+), and are therefore likely to have little stability (F. BRYAN, 1986a,b, Chapters 2 and 3).

Due to the ACC it is even less probable that there exist any equatorially symmetric equilibria. Figs. 5.2a-5.2e show that it is difficult to even assign to the spin-up any of the box model steady states: surface and zonally averaged tracer fields are almost completely symmetric (Figs. 5.2a,b), the thermohaline circulation not at all (Fig. 5.2c). Sinking at high northern latitudes is strengthened by 35% compared to the 1-hemisphere case, whereas a hemisphere-wide overturning cell is absent in the south. Consequently, heat transport is weak in the Southern Hemispheres, it is accomplished by diffusion in the ACC and by the wind-driven cell at low latitudes. The cross-equatorial heat transport amounts to 0.37 PW for both basins combined. The seeming discrepancy between tracer and overturning

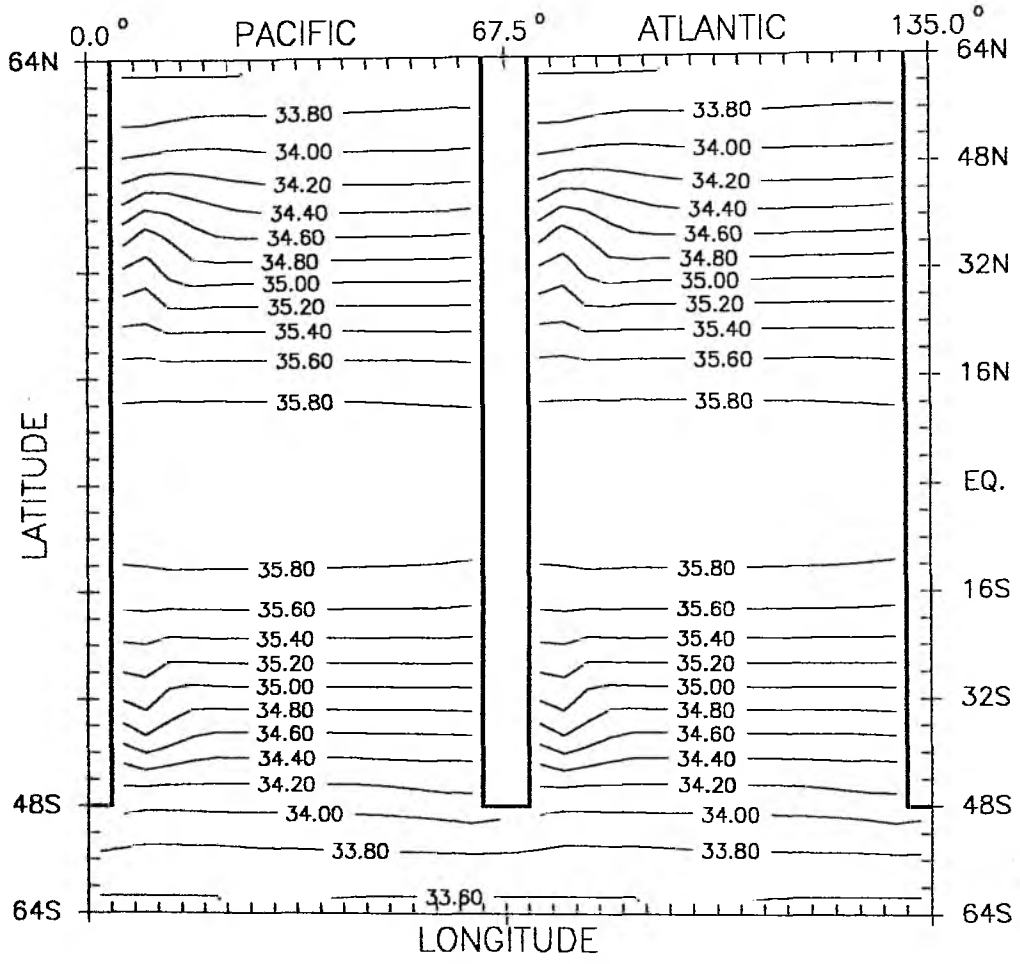
0.0°
PACIFIC
67.5°
ATLANTIC
135.0°
64N
48N
32N
16N
EQ.
16S
32S
48S
64S
LATITUDE
LONGITUDE
33.80
34.00
34.20
34.40
34.60
34.80
35.00
35.20
35.40
35.60
35.80
a

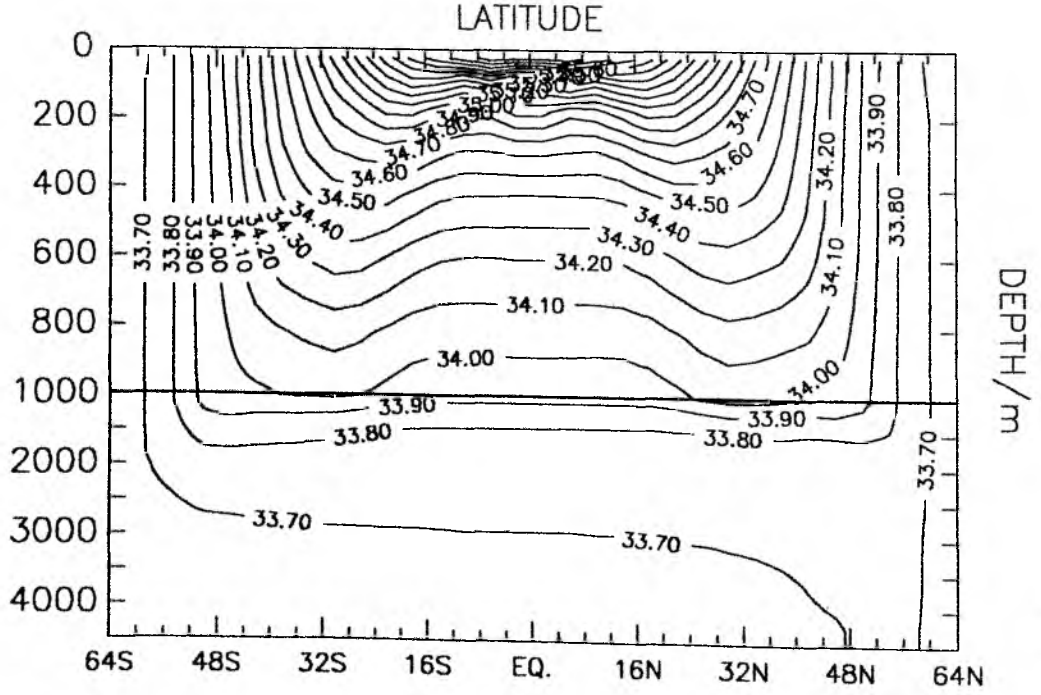
LATITUDE
0
200
400
600
800
1000
2000
3000
4000
64S
48S
32S
16S
EQ.
16N
32N
48N
64N
DEPTH/m
33.70
33.80
33.90
34.00
34.10
34.20
34.30
34.40
34.50
34.60
34.70
b

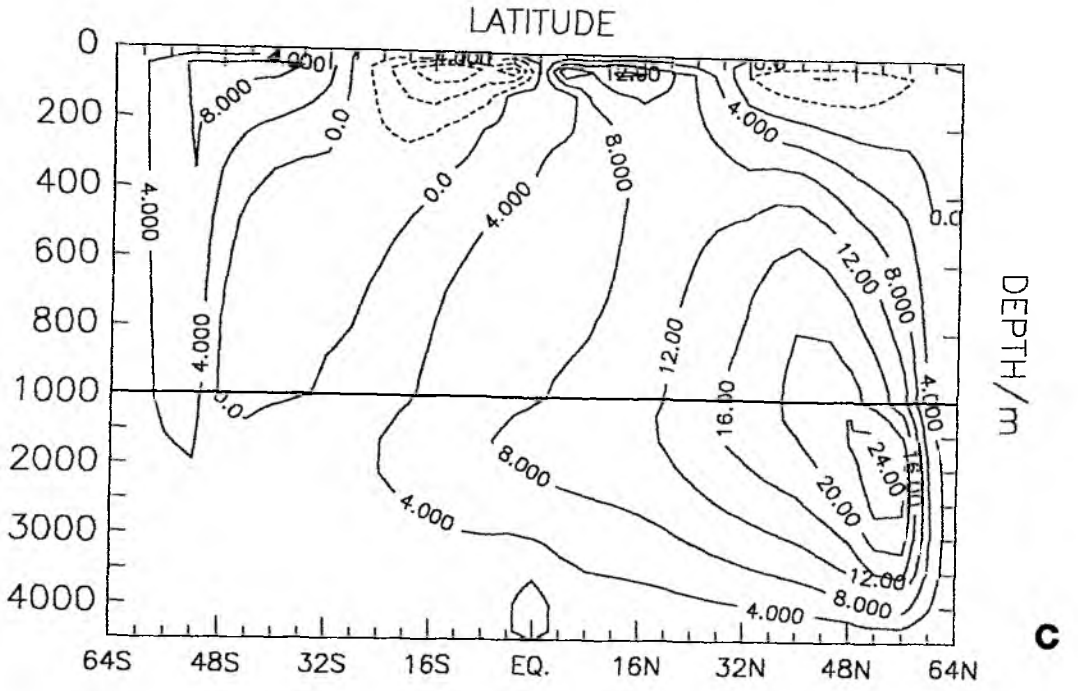

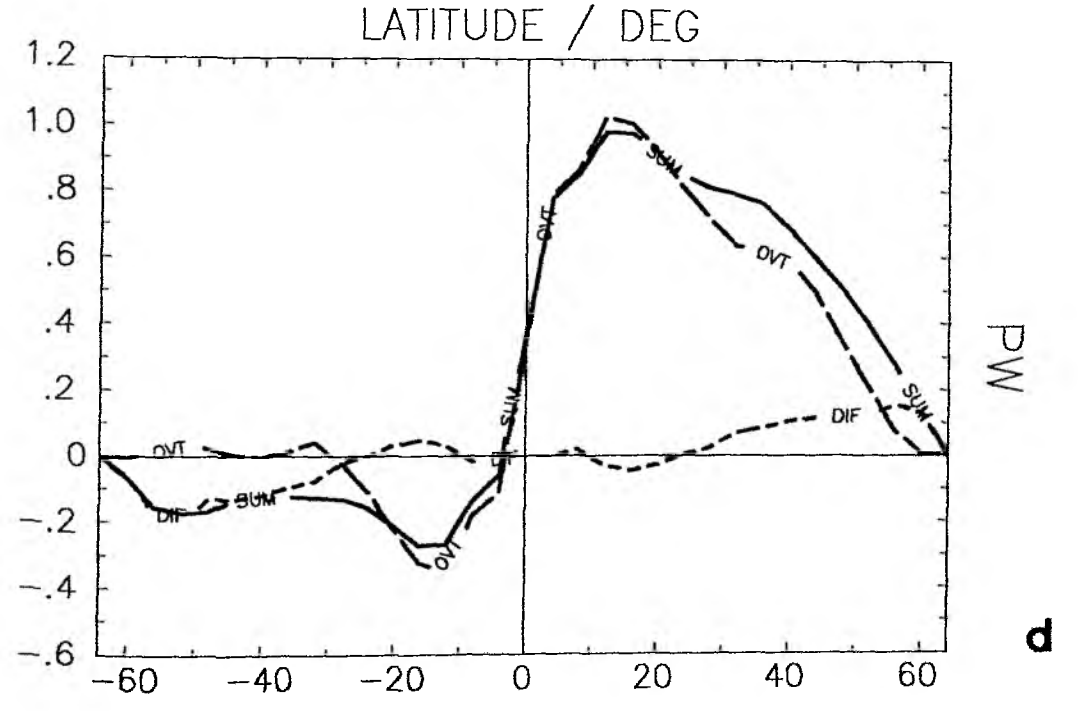

Fig. 5.2a-e: Spin-up steady state of the global GFDL model. Surface salinity in psu (a), zonally averaged salinity in psu (b), meridional stream function in Sv, both basins combined (c), northward heat transport in PW, both basins combined, SUM: total transport, OVT: overturning part, DIF: diffusive part (d).

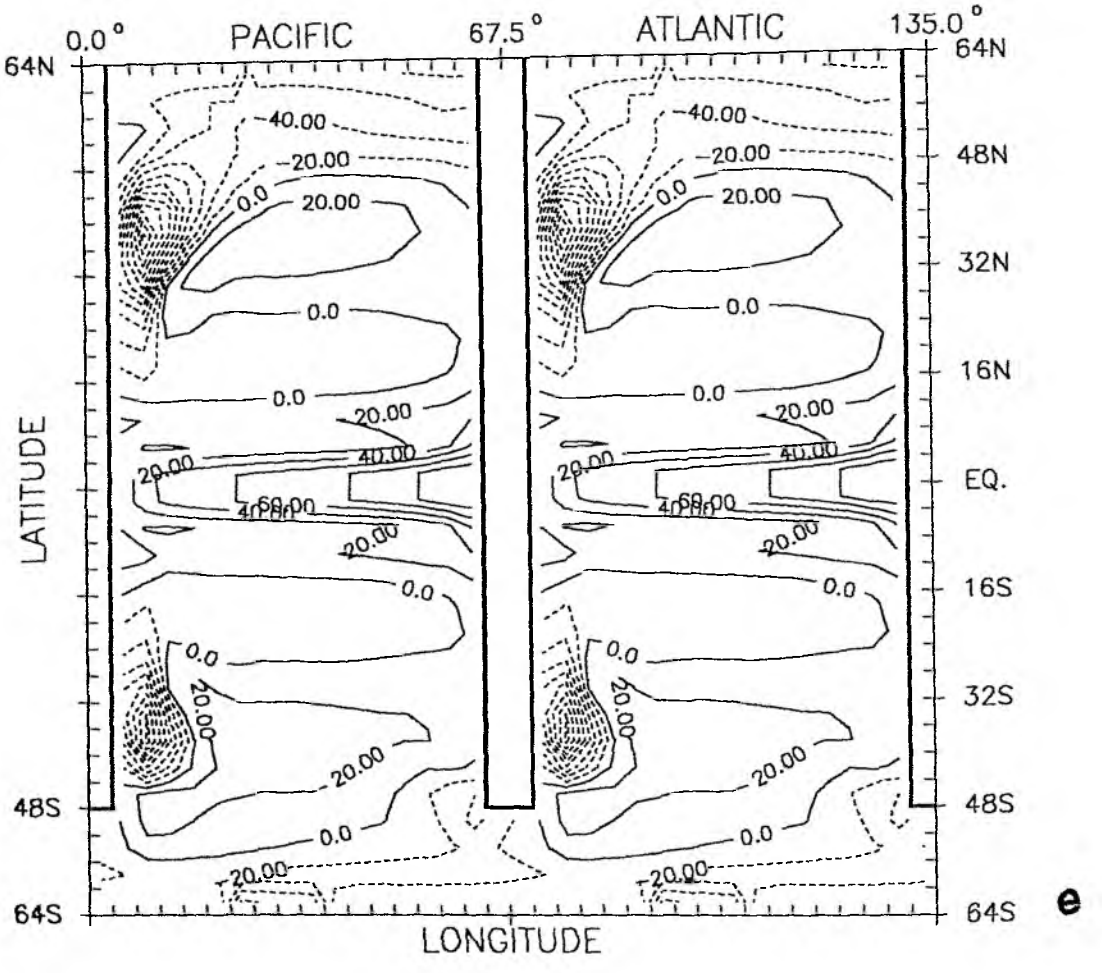

Fig. 5.2 (contd.): Ocean surface heat uptake in W/m^2 (e).

symmetry properties also occurs in COX' (1989) idealized World Ocean model, the thermohaline circulation (Fig 5.2c) is similiar in structure to MEAD's (1988) 2°-resolution model. To reconcile Figs. 5.2b and 5.2c it is necessary firstly to consider the ACC dynamics more closely.

GILL and BRYAN (1971) found that in a 1-hemisphere model including the ACC the wind-driven cell associated with the westerlies extends to much greater depths than without a channel; in Fig. 5.2c the 4 Sv-line reaches down to 2000 m depth, compared to 150 m of the -4 Sv-line in the Northern Hemisphere.

GILL and BRYAN (1971) attribute this to the fact that due to cyclic continuity no pressure difference between eastern and western boundaries can geostrophically balance the mean meridional flow, so the latter is greatly reduced. Part of it compensates the surface Ekman transport in the presence of zonal barriers, in the ACC complete compensation is achieved only at great depths. The poleward meridional flow north of the channel cannot proceed further and must therefore sink and return equatorwards, at relatively shallow depths. The circulation in and south of the ACC is thus rather efficiently decoupled from the rest of the ocean (GILL and BRYAN, 1971; BRYAN and LEWIS, 1979; COX, 1989).

A simple scale analysis supports this concept: Firstly one notes that with a transport of 200 Sv, the zonally and meridionally averaged, barotropic zonal velocity is 2.5 cm/s. The stationary zonal momentum balance reads under periodic boundary conditions:

$$-f\langle v\rangle = A_{MH}\,\partial_{yy}\langle u\rangle + A_{MH}\,\partial_{zz}\langle u\rangle \qquad (5.4)$$

The second term on the r.h.s. is important only in the Ekman layer, integration over the top model layer gives a northward Ekman velocity of 2 cm/s and a maximum transport of 10 Sv. Below the Ekman layer (5.4) yields

$$\langle v\rangle = -\frac{A_{MH}}{f}\,\partial_{yy}\langle u\rangle \qquad (5.5)$$

We assume that, at all depths, $\langle u\rangle$ has a meridional structure similar to its barotropic part (see 5.2 and 5.3), i.e., its absolute value will first grow and then be reduced, starting from the southern boundary. Thus, it has an intermediate maximum or minimum, dependent on $\langle u\rangle$ being positive or negative at a certain depth, and $\langle v\rangle$ has the opposite sign of $\langle u\rangle$, since f is negative in the ACC region.

Whether $\langle u\rangle$ changes sign with depth depends on the relative strength of the shear, compared to the barotropic part. Zonally averaged potential density varies by at most 0.1 kg/m^3 over 500 km in the top 1500 m, causing a vertical shear of

$$\langle u\rangle(z=0) - \langle u\rangle(z=-D) = -\frac{g}{f\rho_0}\,\partial_y \langle\rho\rangle \cdot D \sim 3 \text{ cm/s}$$

Since the barotropic part of <u> amounts to 2.5 cm/s, we conclude that in the channel the zonal flow ranges from 1-4 cm/s, i.e., is eastward at all depths, and the meridional transport is thus southward at all depths below the surface level.

We see from the difference in meridional overturning in the Northern and Southern Hemispheres that we may regard the thermohaline circulation as a secondary one, being indirectly caused by meridional density gradients: The latter induce eastward geostrophic currents, which build up west-east pressure gradients, and these in turn balance poleward flow. Although it is hard to cast this notion in an analytical form, it seems justified by Figs. 5.2b and 5.2c: Salinities (and temperatures) are practically identical in the two hemispheres, but the lack of zonal barriers in the ACC regions prevents the build-up of a zonal pressure gradient, and the thermohaline meridional circulation remains weak. Fig. 5.2e displays that, in accordance with reduced overturning strength, convective activity and thus heat loss is weaker in the Southern Ocean. The diminished rate of deep water formation in the south allows the Northern Deep Water to penetrate southward across the equator.

5.3 Multiple Steady States of the Global Model

The experiments with the global GFDL model are divided into three groups, the first of which is listed in Table 3. It contains the experiments that yield multiple equilibria of the global model. Under identical forcing, different steady states are achieved by starting from different initial conditions. Since the preparation of the initial states was the critical part of the experiments, it is also described in Table 3.

In Table 3, SG means the spin-up of the global model. HSSP is the set of freshwater fluxes diagnosed from SG. A second (P-E) field, HSAV, was constructed from the 1-hemisphere model by taking the zonal mean of the freshwater fluxes (i.e., <HS1>, see Table 2 and Fig. 4.5a) and mirroring

about the equator. In the channel, the values were reduced to account for the larger area in the Southern Ocean, compared to corresponding latitudes in the Northern Hemisphere. Under steady state conditions, no freshwater transport occurs across the equator, since freshwater gain and loss exactly balance over each hemisphere. The reason for using two different (E-P) fields will become apparent later.

Table 3: Global Model Equilibria

Exp.	Initial State	E-P from	S'/psu	(E-P)' in m/y	Integration time/years
GE1a	SG	HSAV	0	A:+0.18 P:-0.18 $\phi > 44^0$N	493 a
GE1b	GE1a	HSAV	0	0	985 a
GE2	SG	HSAV	0	0	1643 b
GE3a	SG	HSSP	-0.5 $\phi > 44^0$N	0	739 a
GE3b	GE3a	HSAV	0	0	1561 a
GE4a	SG	HSSP	0	A:+0.18 P:-0.18 $\phi > 44^0$N	821 a
GE4b	GE4a	HSSP	0	0	1479 a

SG : global model spin-up
HSSP : freshwater flux diagnosed from global model spin-up
HSAV : freshwater flux diagnosed from 1-hemisphere model, zonally averaged and mirrored about equator
S' : Initial salinity perturbation
(E-P)' : Perturbation in (E-P)
A : Atlantic
P : Pacific
a : asynchronous integration, time step 1 day
b : asynchronous integration, time step 5 days

Experiment GE1 starts from the spin-up state, the freshwater fluxes, obtained from HSAV, are perturbed by 0.18 m/y north of 44°N, such that there is excess evaporation over the Atlantic and excess precipitation over the Pacific. This amounts to an atmospheric water transport of 0.04 Sv from Atlantic to Pacific, which is at the lower end of the estimate given by WARREN (1983). Due to the additional freshwater input, the Pacific overturning collapses within thirty years, in accordance with the results from Chapter 4. Then sinking sets in north of the ACC region in the Pacific, simultaneously the Atlantic circulation is strengthened. This transition is completed within another 100 years. After 493 years of integration with the perturbed freshwater fluxes, the preparation of the initial state is completed and the water flux anomaly is switched off. The integration is continued for another 985 years, when a new equilibrium is reached.

Figs. 5.3a-f show that with boundary conditions identical for Atlantic and Pacific, the states in the two oceans are completely different. Surface salinities are more than 1 psu higher in the North Atlantic than in the North Pacific (Fig. 5.3a). Associated is NADW formation at a rate of 25 Sv, twice the strength of the spin-up overturning in one basin. About 10 Sv of deep water are exported from the Atlantic and return as thermocline water (Fig. 5.3b). The Pacific, however, forms no deep water in the north, and has a generally much weaker thermohaline circulation, with a maximum of 7 Sv at about 40°S. Deep water is imported at a rate of 6 Sv (Fig. 5.3c). The global circulation corresponds to the -+-+ state from the box models.

The circulation patterns are mirrored in the zonally averaged salinity fields: Strong convective activity persists in the North Atlantic and determines the deep ocean salinity. The deep North Pacific, however, is shielded from the surface by the low salinities at shallow depths. In the Southern Hemisphere, warm, salty water originating from the subtropics extends to greater depths in the Pacific than in the Atlantic, where wind-driven circulation in the ACC region and thermohaline circulation north of it collaborate to bring very fresh water up to 200 m depth at 16°S (Figs. 5.3d,e).

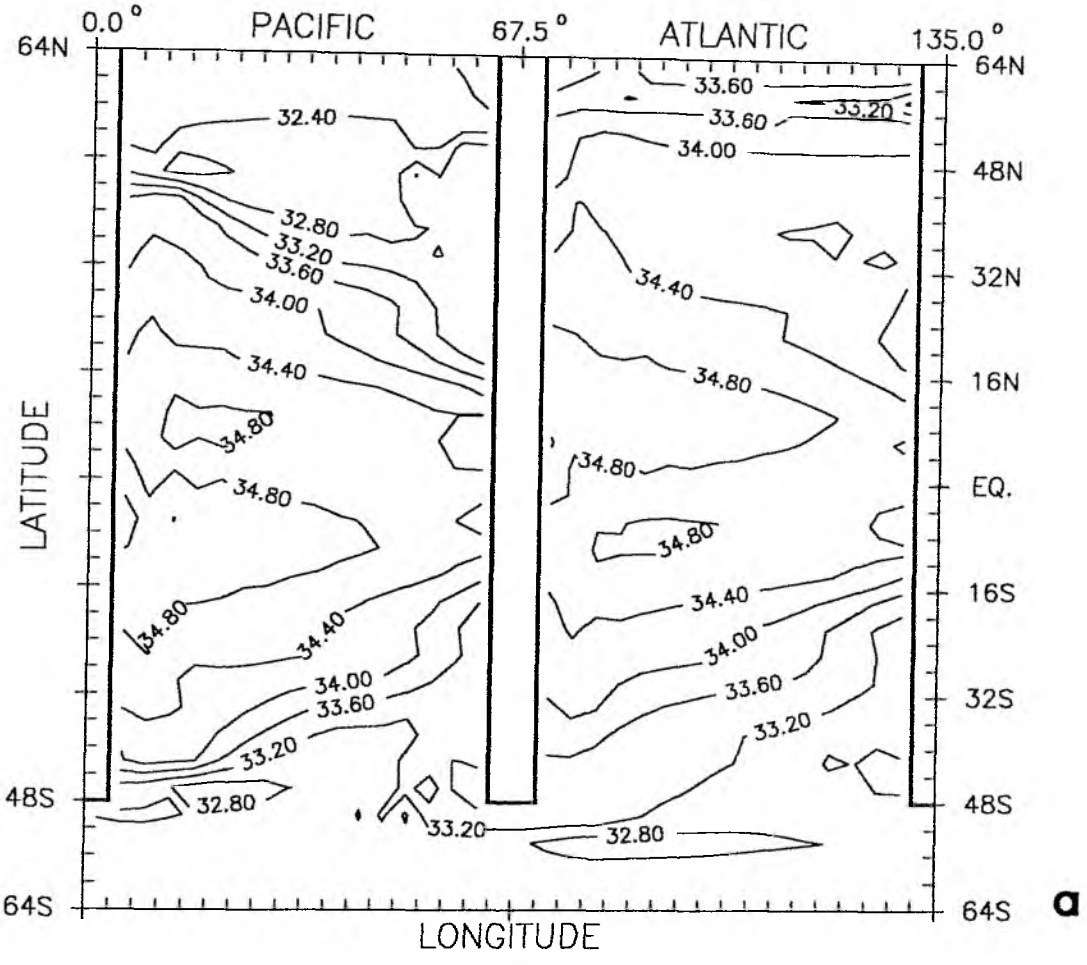

Fig. 5.3a-f: Equilibrium of experiment GE1b (-+-+, P-E symmetric about the equator and zonally invariant). Surface salinity in psu (a).

Meridional heat transports are displayed in Fig. 5.3f. Atlantic transport is 0.6 PW northward across the equator and has its maximum at 15°N with 0.9 PW. This is almost three times the value from the 1-hemisphere model, showing the importance of modelling the correct global thermohaline circulation pattern. Heat transport in the Pacific reaches less than half of the Atlantic's strength and is not as markedly asymmetric. Combined the two oceans transport 0.35 PW northward across the equator.

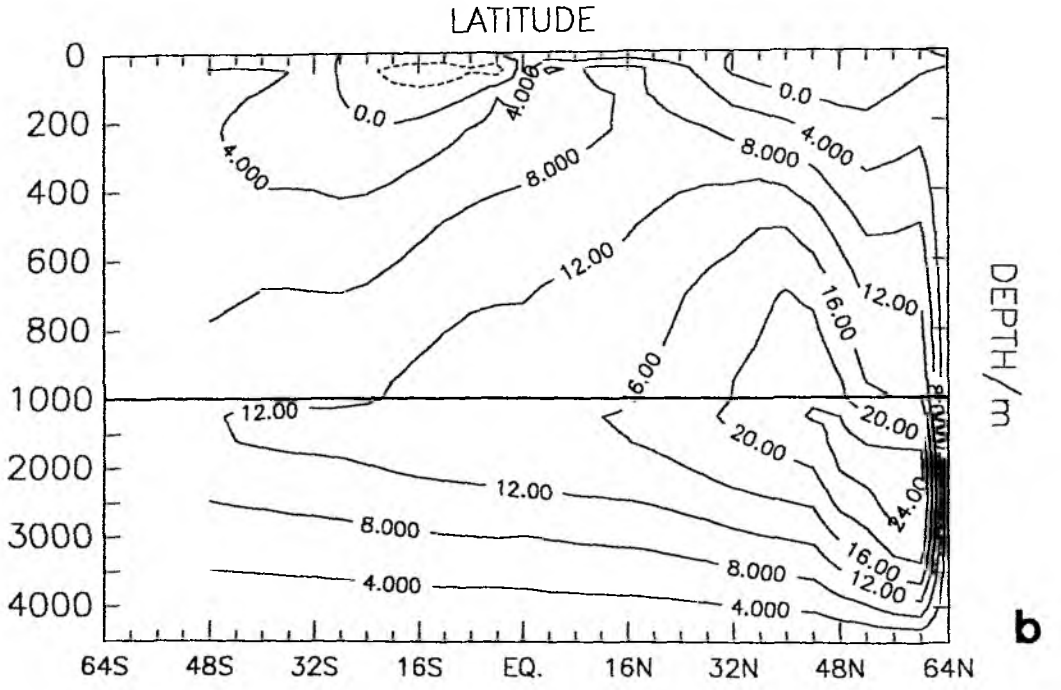
LATITUDE
0
200
400
600
800
1000
2000
3000
4000
64S
48S
32S
16S
EQ.
16N
32N
48N
64N
DEPTH/m
0.0
4.000
8.000
12.00
16.00
20.00
24.00
6.00
b

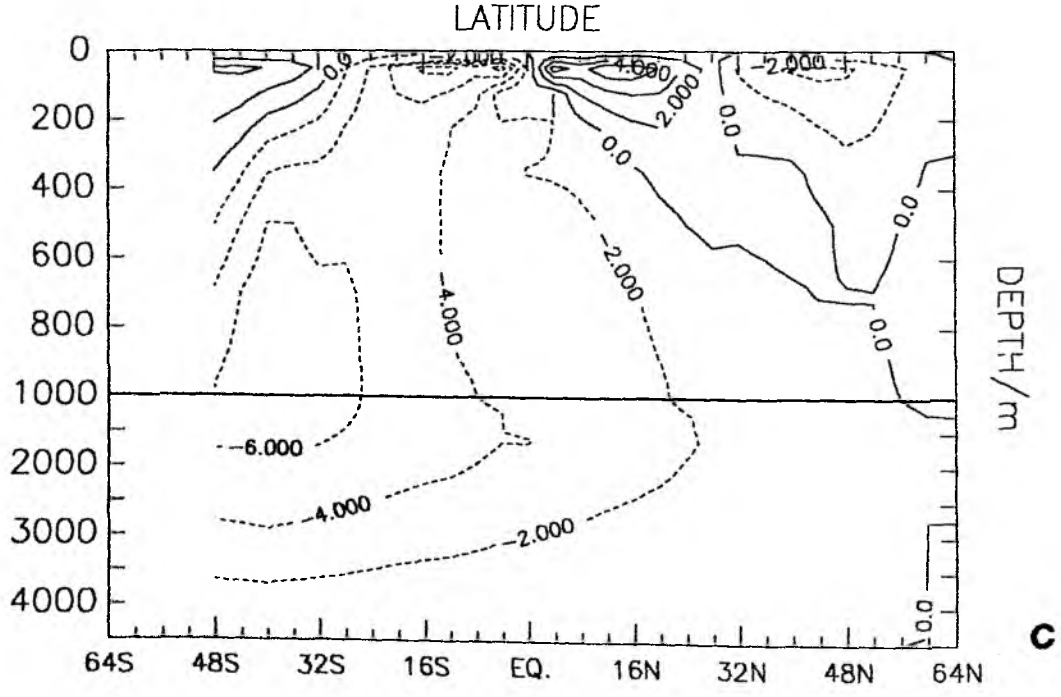
LATITUDE
0
200
400
600
800
1000
2000
3000
4000
64S
48S
32S
16S
EQ.
16N
32N
48N
64N
DEPTH/m
0.0
2.000
4.000
6.000
c

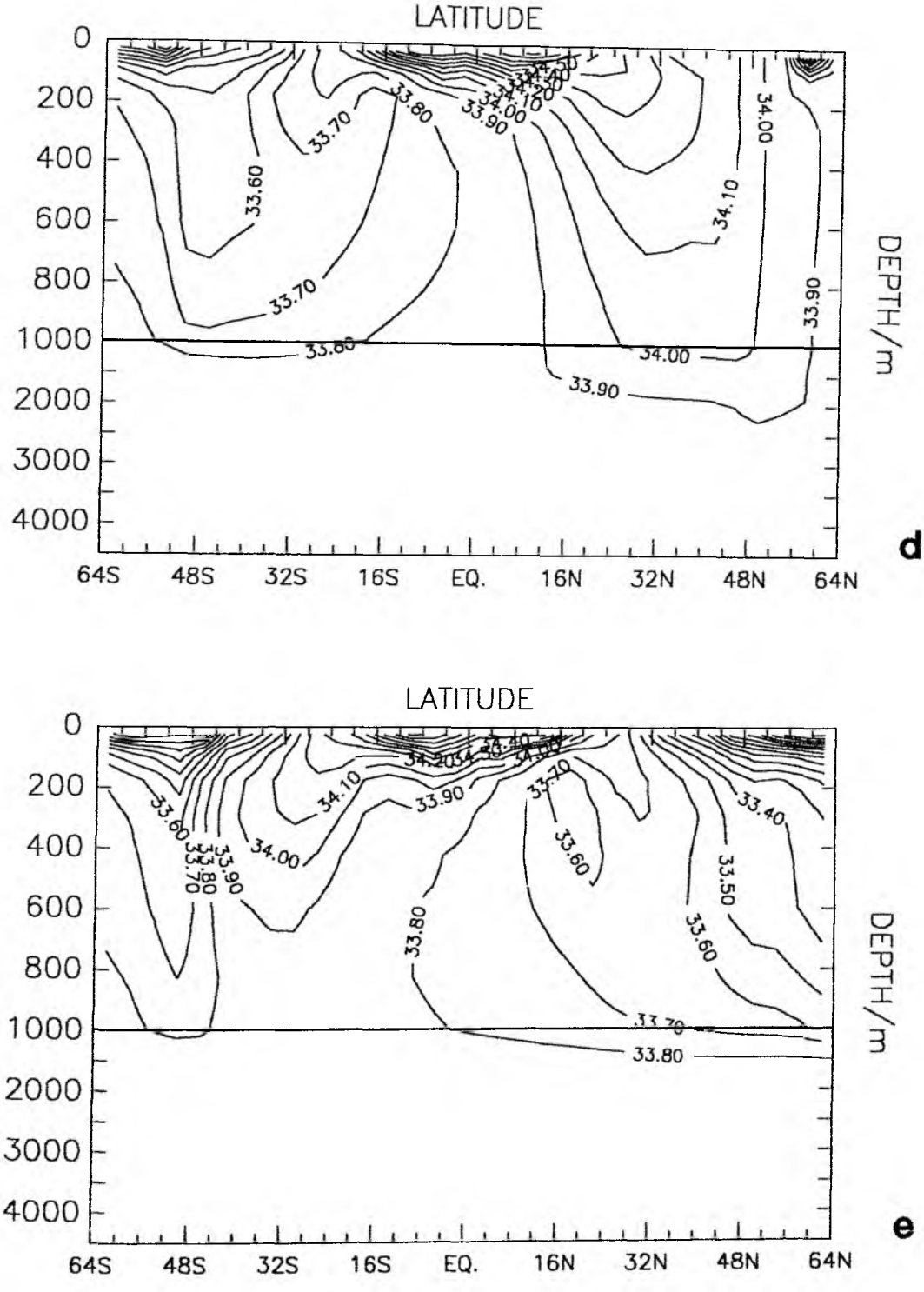

Fig. 5.3 (contd.): Equilibrium of experiment GE1b. Atlantic meridional stream function in Sv (b), Pacific meridional stream function in Sv (c), Atlantic zonally averaged salinity in psu (d), Pacific zonally averaged salinity in psu (e).

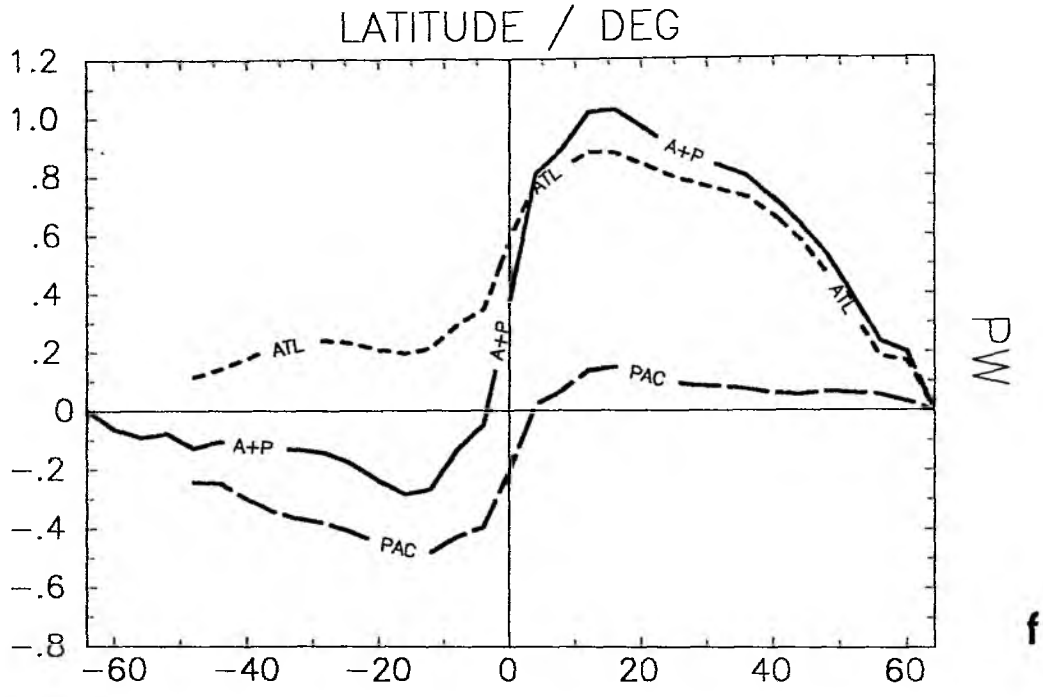

Fig. 5.3 (contd.): Equilibrium of experiment GE1b. Northward heat transport in PW for Atlantic (ATL), Pacific (PAC) and the two basins combined (A+P) (f).

The different circulations and heat transports are maintained while SST still is practically identical in the two basins, due to the Newtonian cooling law. In reality and in coupled ocean-atmosphere models, the enhanced Atlantic heat transport warms both surface water and air. We see that these higher temperatures have to be considered a consequence of the asymmetric thermohaline circulation, rather than being the fundamental cause for its maintenance, as assumed by WARREN (1983) and BROECKER (1987).

Taking exactly the spin-up as initial state, i.e., simply shifting over to mixed boundary conditions (Experiment GE2, Table 3), leads to the state with deep water formation in both Northern Hemispheres, i.e., the +--+ state. Figs. 5.4a-d show that in the final state, after 1643 years, both oceans are similar to the Atlantic from experiment GE1, though not as pronounced. Surface salinities are very similar (Fig. 5.4a), but maximum overturning

strength is 18 Sv in each basin (Fig. 5.4b), compared to 25 Sv. Accordingly, the meridional heat transport is vigorous, with a total of 0.8 PW across the equator and almost 1.4 PW at its maximum (Fig. 5.4d), but both values are less than twice the Atlantic transports of GE1 (0.6 PW and 0.9 PW, respectively). Opposed to the spin-up, also the zonally averaged salinity field shows a marked north-south asymmetry (Fig. 5.4c), so the notion of regarding the spin-up as the symmetric state (++++) is justified, despite its asymmetric circulation.

As will be discussed in detail in the next section, the state with sinking in both Northern Hemispheres is clearly preferred, if the symmetric, zonally invariant (P-E) field HSAV is applied. Thus it required several attempts to find the starting point that finally would lead to the equilibrium forming no Northern Deep Water at all (-++-). At last, the steady state of experiment GE3a with freshwater fluxes diagnosed from the spin-up was chosen as initial condition, since it already had the desired circulation pattern. After an adjustment period of about 100 years the state displayed in Figs. 5.5a-d emerged in experiment GE3b. Both oceans resemble the Pacific from run GE1, especially in the Northern Hemispheres, but there are deviations in the south. Salinities are higher in the Southern Ocean in the -++- case and total overturning strength shows an almost fourfold increase compared to the Pacific from GE1, demonstrating again that the coupling of the two oceans is essential for predicting the correct circulation. Meridional heat transports, however, are only slightly increased (compare Pacific heat transports in Figs. 5.5d and 5.3f), since the main differences in overturning strength are at depths where no substantial vertical temperature variations occur.

Somewhat surprising are the inter-basin asymmetries visible in Fig. 5.5a. From the southern edges of the continents to northern mid-latitudes, surface salinities in the Atlantic are higher than in the Pacific, the difference reaching up to 0.4 psu. The salinity contrast between equator and Southern Ocean is also higher in the Atlantic, and consequently the thermohaline circulation is weaker by 2 Sv (not shown). Higher salinity contrast and weaker overturning in the Atlantic result in identical freshwater transports for the two oceans (not shown) and slightly weaker Atlantic heat transport (Fig. 5.5d).

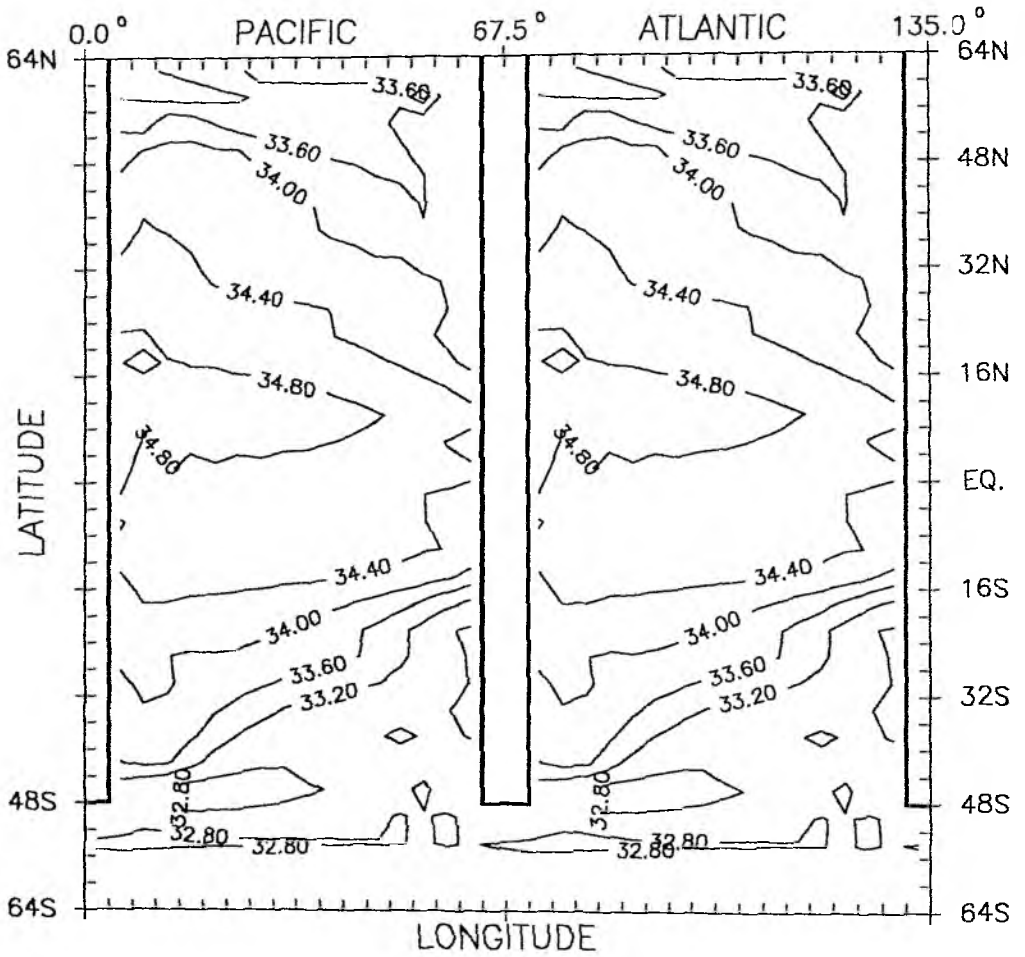
0.0°
PACIFIC
67.5°
ATLANTIC
135.0°
64N
48N
32N
16N
EQ.
16S
32S
48S
64S
LATITUDE
LONGITUDE
33.60
34.00
34.40
34.80
33.20
32.80
a

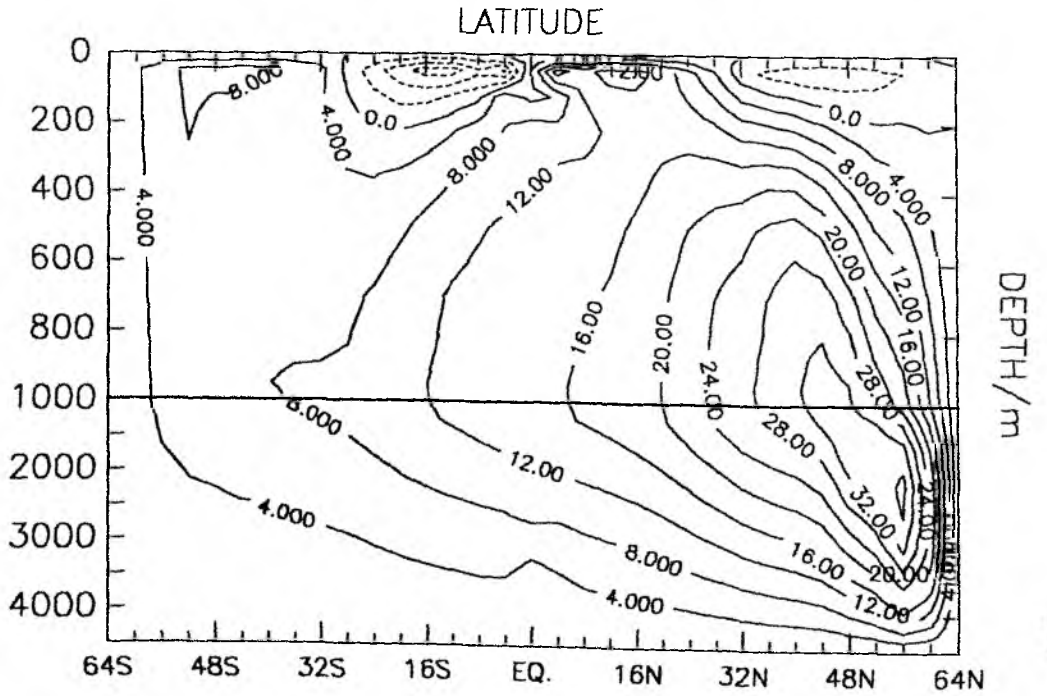
LATITUDE
0
200
400
600
800
1000
2000
3000
4000
64S
48S
32S
16S
EQ.
16N
32N
48N
64N
DEPTH/m
8.000
4.000
0.0
12.00
16.00
20.00
24.00
28.00
32.00
b

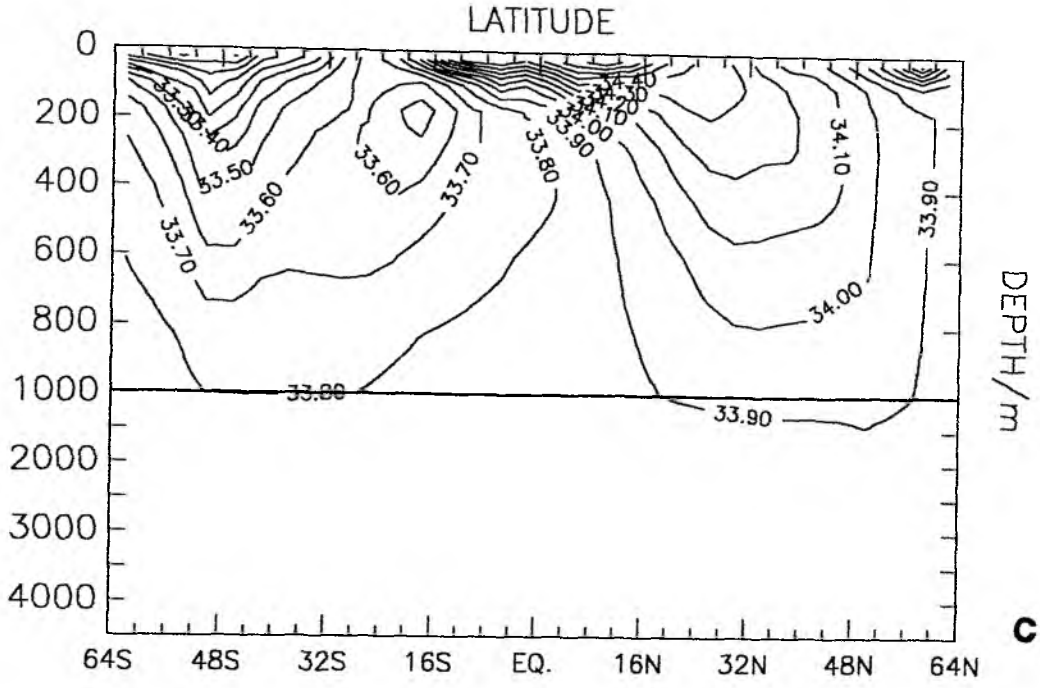

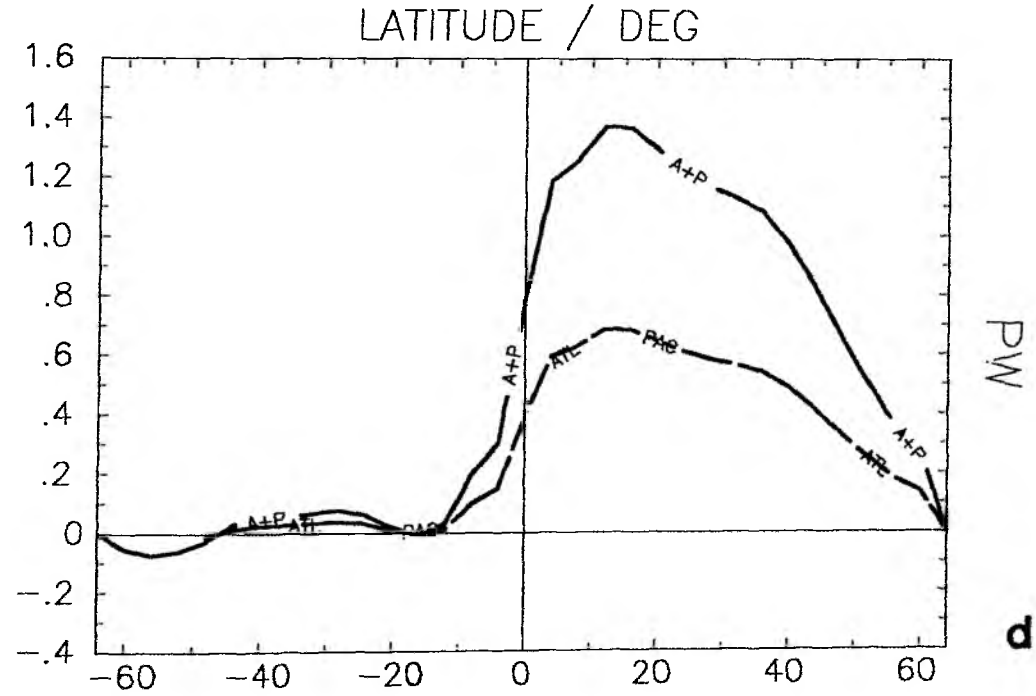

Fig. 5.4a-d: Steady state of experiment GE2 (+--+, P-E symmetric about the equator and zonally invariant). Surface salinity in psu (a), meridional stream function in Sv, both basins combined (b), zonally averaged salinity in psu (c), northward heat transport in PW for Atlantic (ATL), Pacific (PAC) and the two basins combined (A+P) (d).

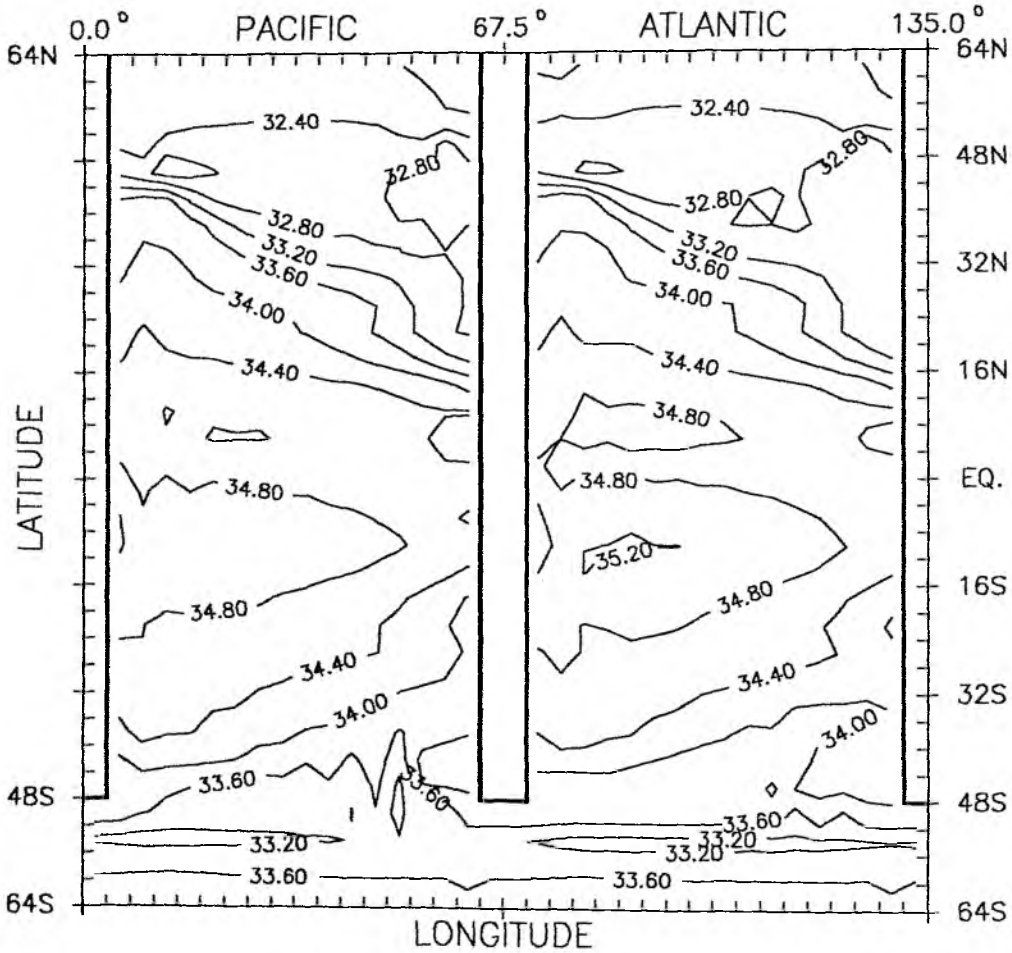
0.0°
PACIFIC
67.5°
ATLANTIC
135.0°
64N
48N
32N
16N
EQ.
16S
32S
48S
64S
LATITUDE
LONGITUDE
32.40
32.80
33.20
33.60
34.00
34.40
34.80
35.20
a

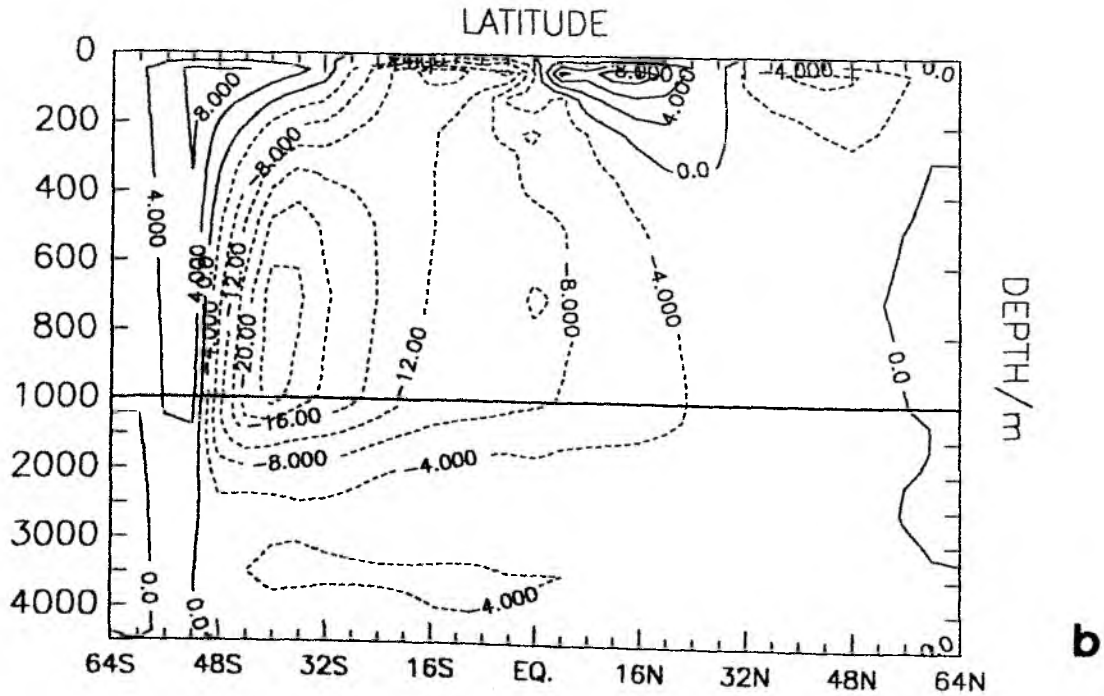
LATITUDE
0
200
400
600
800
1000
2000
3000
4000
DEPTH/m
64S
48S
32S
16S
EQ.
16N
32N
48N
64N
8.000
4.000
0.0
-4.000
-8.000
-12.00
-16.00
-20.00
b

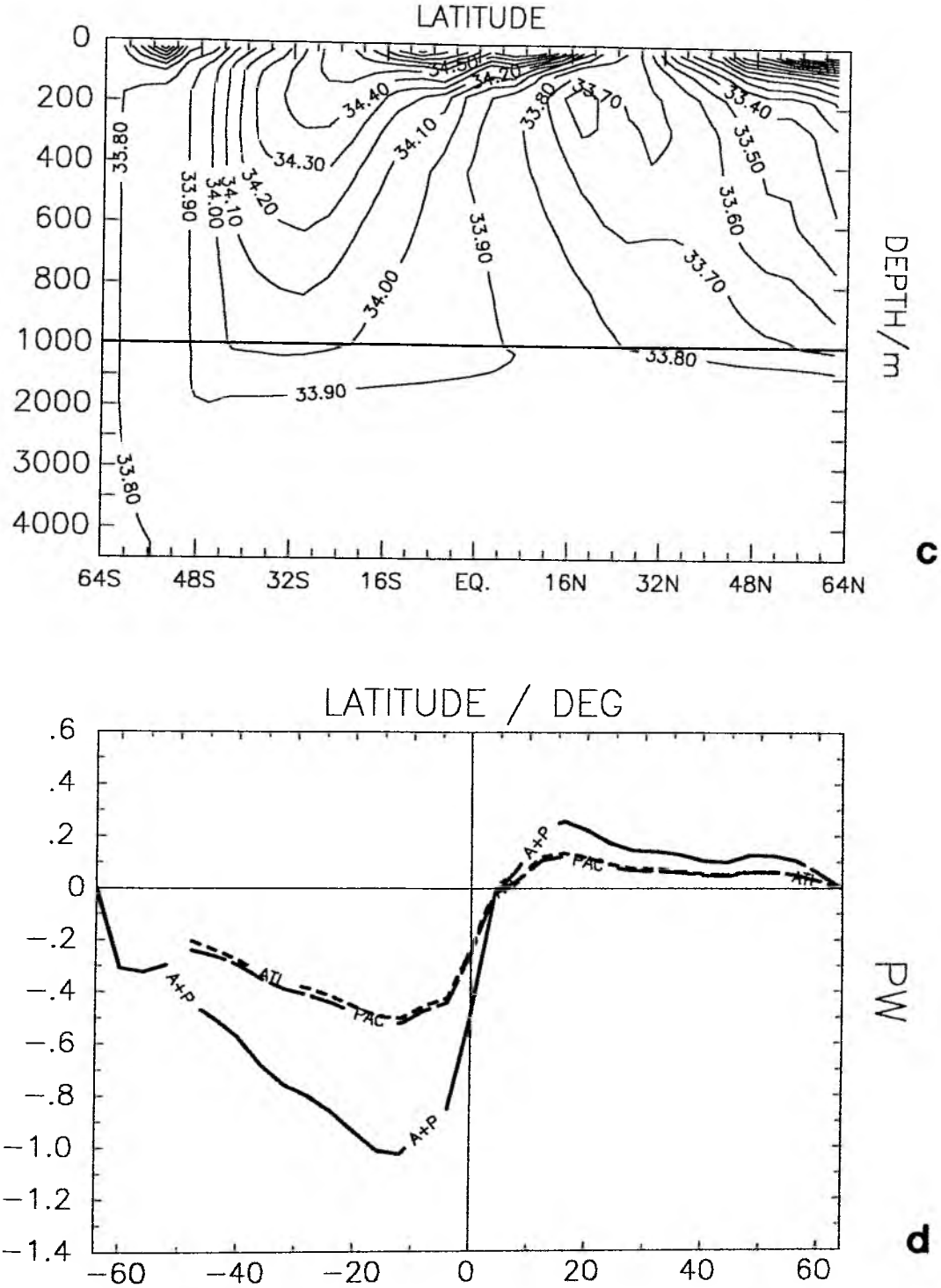

Fig. 5.5a-d: Steady state of experiment GE3b (-++-, P-E symmetric about the equator and zonally invariant). Surface salinity in psu (a), meridional stream function in Sv, both basins combined (b), zonally averaged salinity in psu (c), northward heat transport in PW for Atlantic (ATL), Pacific (PAC) and the two basins combined (A+P) (d).

The differences between the oceans stem from oscillations that arise spontaneously during the adjustment at the beginning of experiment GE3b. They have a period of about 10 years and are associated with changing convective activity in and around the Southern Ocean and oscillatory behaviour of the difference in overturning strength between Atlantic and Pacific. This kind of oscillation also occurred in a different experiment, with greater regularity, and will be discussed in detail in Chapter 6. Suffice it to state here that the differences between the basins are quantitative rather than qualitative, and that it is unclear whether they would disappear during a continued integration. This might happen because Figs. 5.5a-d do not show a complete equilibrium: the basin averaged heat uptake is 0.1 W/m^2, reflecting that due to the relatively shallow thermohaline circulation the deep ocean temperature and salinity fields adjust only slowly.

No further qualitatively different equilibria of the global thermohaline circulation have been found. We conclude that of the 16 global box model steady states at least four exist even for the global GFDL model, three of which are essentially different (Fig. 5.6):

1. +--+ both oceans form Northern Deep Water (experiment GE2)
2. -++- no ocean forms Northern Deep Water, sinking occurs in the south (experiment GE3)
3. -+-+ the conveyor belt, NADW is formed, but no "NPDW" (experiment GE1)
4. +-+- equivalent to 3., since the basins are interchangeable

All these states are obtained under identical freshwater fluxes, which are the ones from the one-hemisphere spin-up S1, zonally averaged and mirrored about the equator (HSAV, Table 3).

Note that the spin-up (++++), which is an equilibrium state to the forcing with the freshwater fluxes HSSP, is not included among the steady states listed above. Experiment GE2, which starts from exactly the spin-up, shows that it is unstable if the freshwater fluxes HSAV are applied. Experiment GE4, included in Table 3, will likewise be described in the next section.

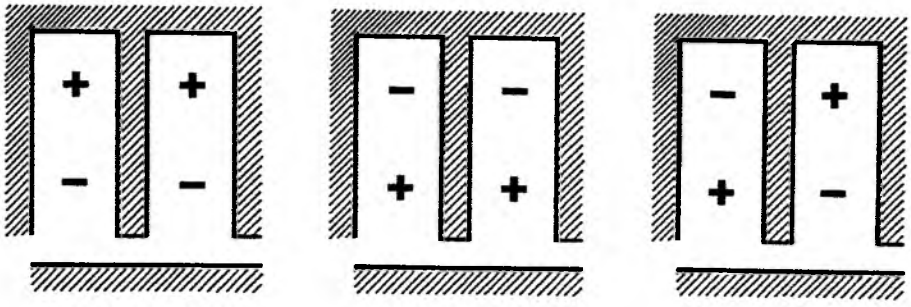

Fig. 5.6: Scheme of the three essentially different steady states of the global GFDL model. + denotes sinking and deep water formation in the respective hemisphere, - the absence of it. The third equilibrium, -+-+, corresponds to the "conveyor belt".

5.4 Stability of the Global Model Equilibria

Section 5.3 demonstrated that four different steady states of the global thermohaline circulation exist under identical boundary conditions: no ocean forms Northern Deep Water or both do, or either one of the Atlantic and Pacific but not the other. Two questions remain: how likely is each state to be obtained, and under what conditions is a transition from one equilibrium to another possible?

The same questions were addressed using the global box model (Section 2.4), and from the discussion there it is clear that a complete answer cannot be given for a 3-D model, even for the idealized one employed here. Again, one would have to vary the (E-P) field systematically and to try a large number of initial conditions. Since a typical experiment with the global model requires 10-20 hours CPU on a CRAY-XMP, some long-term runs even more, any systematic exploration of the phase space is infeasible. Nevertheless it is possible to draw some conclusions about how sensitive the preference of the equilibria is to the choice of the freshwater fluxes. Besides, some tests are performed on the stability of run GE1.

The experiments that tested the preference and sensitivity of the steady states are listed in Table 4. The initial and final states are characterized according to Fig. 5.6. Only the freshwater fluxes were perturbed, not the initial salinities.

Table 4: Sensitivity of the Global Model Equilibria

Experiment	Initial State	(E-P) from	(E-P)' in m/y	Final state
GE2	SG (++++)	HSAV	0	+--+
GS1	SG (++++)	HSAV	A,P:-0.18 ϕ> 44°N	+--+
GS2	rest	HSAV	0	+--+
GS3	rest	HSAV	A,P:-0.18 ϕ> 44°N	+--+
GS4	SG (++++)	HSSP	0	-++-
GS5	SG (++++)	HSSP	A,P:+0.18 ϕ> 44°N	-++-
GS6	SG (++++)	HSSP	A,P:+0.9 ϕ> 32°N	-+-+
GS7	GE1b (-+-+)	HSAV	A:-0.18 P:+0.18 ϕ> 44°N	+--+
GS8	GE4b (-+-+)	HSSP	A:-0.18 P:+0.18 ϕ> 44°N	-++-
GS9	GE1b (-+-+)	HSAV	A:-0.36 P:+0.36 ϕ> 44°N	+-+-

As already mentioned in the preceding section, experiment GE2 which starts from exactly the spin-up and uses HSAV as freshwater fluxes (no perturbation) yields the state with sinking in both Northern Hemispheres (+--+) as final state. To test the notion that +--+ is preferred under the freshwater fluxes HSAV, experiments GS1, GS2 and GS3 were performed. In GS1 a bias

toward inhibiting deep water formation in Northern Hemispheres is introduced. Precipitation is enhanced by 0.18 m/y north of 44°N, in both oceans, but still +--+ emerges as final state.

It can be argued (MEAD, 1988) that the asymmetric meridional circulation of the spin-up introduces a bias by the initial northward salinity flux across the equator, favouring sinking in the north. This bias is removed in experiments GS2 and GS3, which start from a state of rest. GS2 uses exactly HSAV as freshwater fluxes, in GS3 these are perturbed by the same excess of precipitation as in GS1, i.e., 0.18 m/y , north of 44°N, in both oceans. Still only the +--+ state was obtained, so we conclude that this equilibrium is by far preferred, if the freshwater fluxes HSAV, which are zonally invariant and symmetric about the equator, are used. Under equilibrium conditions no freshwater is transported across the equator, i.e., no bias is introduced by HSAV. Thus we can regard the preference of the +--+ state as one more manifestation of the fact that the asymmetric geometry of the model favours deep water formation in the north. Remember that this was already evident from the meridional overturning of the spin-up, which is asymmetric despite the symmetric tracer distributions (Figs. 5.2b,c).

The surface freshwater fluxes from the spin-up, HSSP, produce a freshwater transport southward across the equator of slightly more than 0.1 Sv in each basin. Compared to the (E-P) field HSAV, this means a difference in the surface fluxes of less than 0.1 m/y, averaged over one hemisphere. Fig. 5.7 shows that the zonal means of the two fields do not differ qualitatively.

Still, the excess precipitation over the Northern Hemispheres, as diagnosed from the spin-up, so efficiently inhibits Northern Deep Water formation that preference of the equilibria completely changes. Starting from the spin-up both no anomaly (GS4) and symmetric +0.18 m/y (E-P) anomaly north of 44°N (GS5) produced the equilibrium with sinking only in the Southern Hemispheres. No state with sinking in both Northern Hemispheres (+--+) has been found, the most violent attempt, with excess evaporation of 0.9 m/y over both oceans north of 32°N, resulted in a "spontaneous symmetry breaking": Gradually a -+-+ state emerged. The -++- state is clearly

favoured to the other equilibria, so one concludes that the (E-P)-asymmetry with respect to the equator easily outweighs the one induced by the geometry (Section 5.2). Experiments GE2 and GS4 show that the spin-up is unconditionally unstable under both set of freshwater fluxes used here. It should be mentioned that using the zonally averaged freshwater fluxes, won from the spin-up, showed no different behaviour for the two experiments designed according to GS4 and GS5.

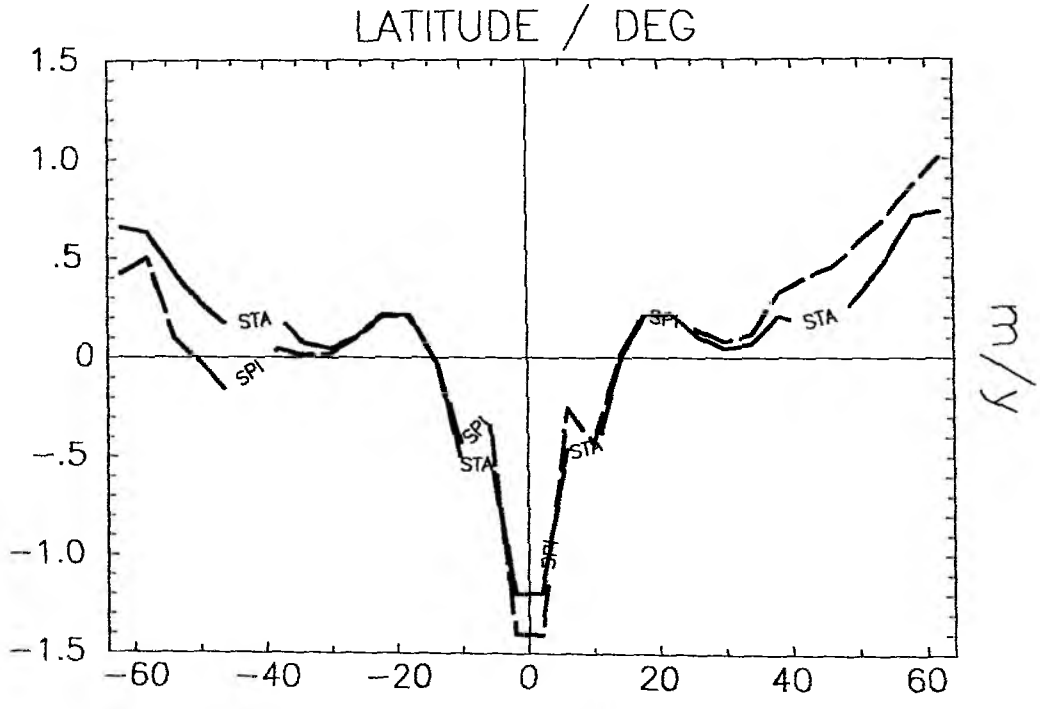

Fig. 5.7: Zonally averaged surface freshwater fluxes (P-E) in m/y, for HSAV, i.e., P-E symmetric about the equator and zonally invariant (STA), and HSSP, i.e., P-E taken from the global spin-up (SPI).

Actually, during the course of the experiments the -++- state was inadvertently produced again and again, at the attempt to obtain the conveyor belt. Only the intermediate introduction of (E-P)-differences

between North Atlantic and North Pacific (0.18 m/y, north of 44°N, experiment GE4a, Table 3) produced a -+-+ state, which then persisted even after the water flux perturbation was switched off (GE4b). Figs. 5.8a-d display the most characteristic features of the final state GE4b.

Surface salinities vary over a much greater range than in the case of symmetric (E-P), and like in the 1-hemisphere case, the northeastern parts are markedly depleted of salt. The resemblance is most pronounced for the North Atlantic (compare Figs. 5.8a and 4.10a). The zonal salinity gradient again results in a strengthening of the meridional overturning north of 48°N, for the other latitudes, the Atlantic circulation is weaker than in experiment GE1b (Figs. 5.3b, 5.8b), whereas it is relatively more vigorous in the Pacific (Figs. 5.3c, 5.8c). As a consequence, Atlantic and total northward heat transports are reduced, and there is a combined transport of only 0.1 PW across the equator (Fig. 5.8d).

Still the two -+-+ equilibria GE1b and GE4b are qualitatively equivalent, so being faced with having to choose one of them as the initial state of a, say, climate change experiment would be a painstaking situation. The states are very much alike, and yet due to the (E-P) differences their stability behaviours are completely different (experiments GS7 and GS8, Table 4). Imposing (E-P) anomalies opposite to the ones at the beginning of the experiments, i.e., 0.18 m/y with excess evaporation over the Pacific and excess precipitation over the Atlantic, results in a reversal of the Pacific circulation for GS7, starting from GE1b (yielding +--+), and a reversal of the Atlantic in the case GS8, starting from GE4b (causing -++-).

Apart from the existence of the multiple equilibria, the sensitivity of the model results to minor changes in the freshwater fluxes is perhaps the most important result of this study. MEAD (1988) used water fluxes that were zonally invariant and symmetric about the equator, but adapted the fields from BAUMGARTNER and REICHEL (1975), which have only half the amplitude of the distribution used here. In this case, excess precipitation of 0.25 m/y over the Pacific did not produce the conveyor belt, but a +--+ circulation with weakened Pacific overturning, which is most likely due to the generally reduced salinity influence on the thermohaline circulation.

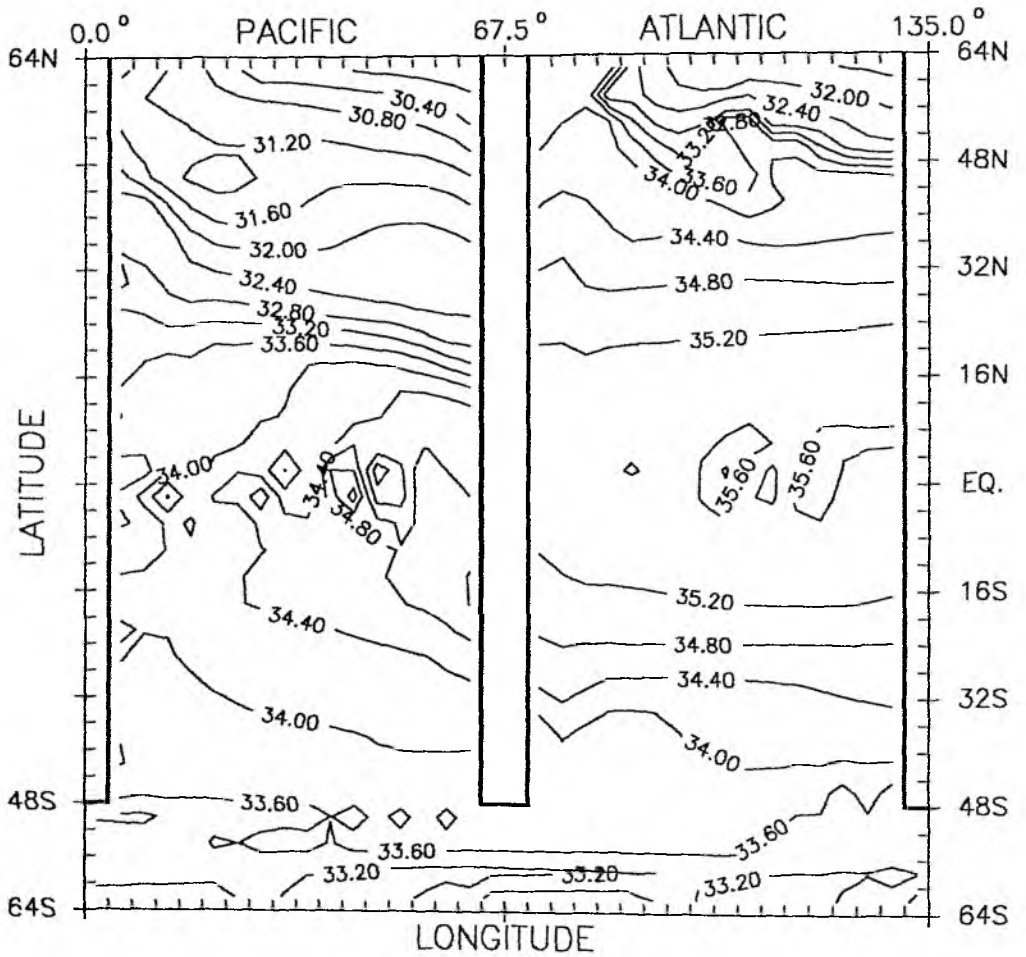
0.0°
PACIFIC
67.5°
ATLANTIC
135.0°
64N
48N
32N
16N
EQ.
16S
32S
48S
64S
LATITUDE
LONGITUDE
30.40
30.80
31.20
31.60
32.00
32.40
32.80
33.20
33.60
34.00
34.40
34.80
35.20
35.60
a

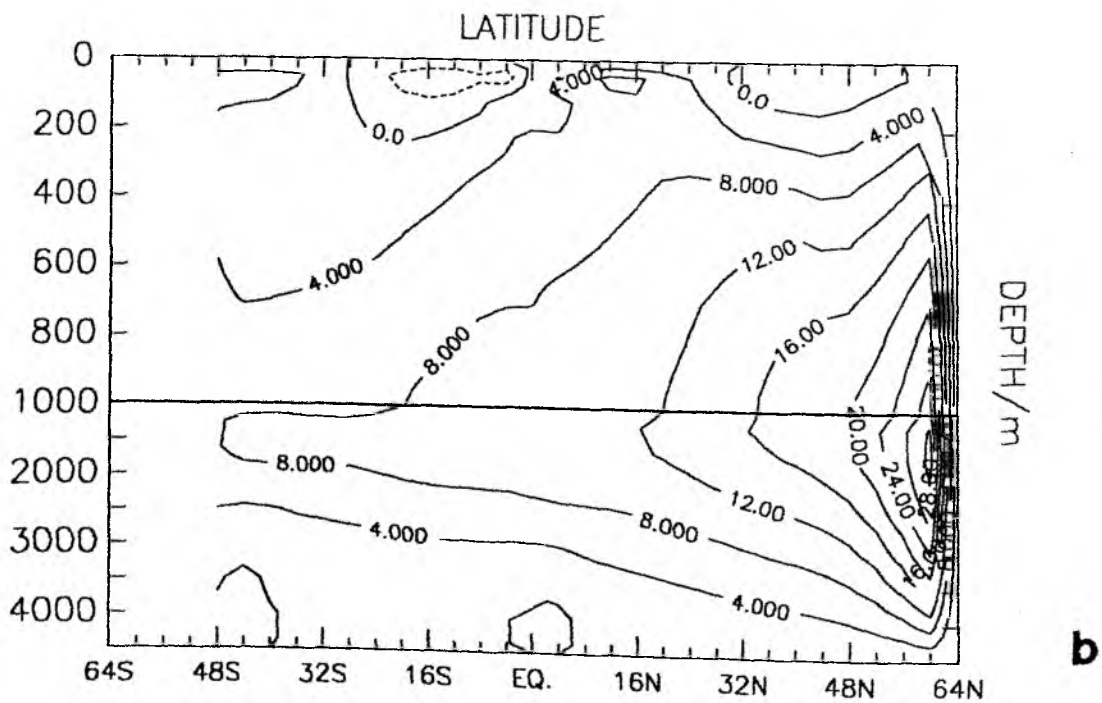
LATITUDE
0
200
400
600
800
1000
2000
3000
4000
DEPTH/m
64S
48S
32S
16S
EQ.
16N
32N
48N
64N
0.0
4.000
8.000
12.00
16.00
20.00
24.00
b

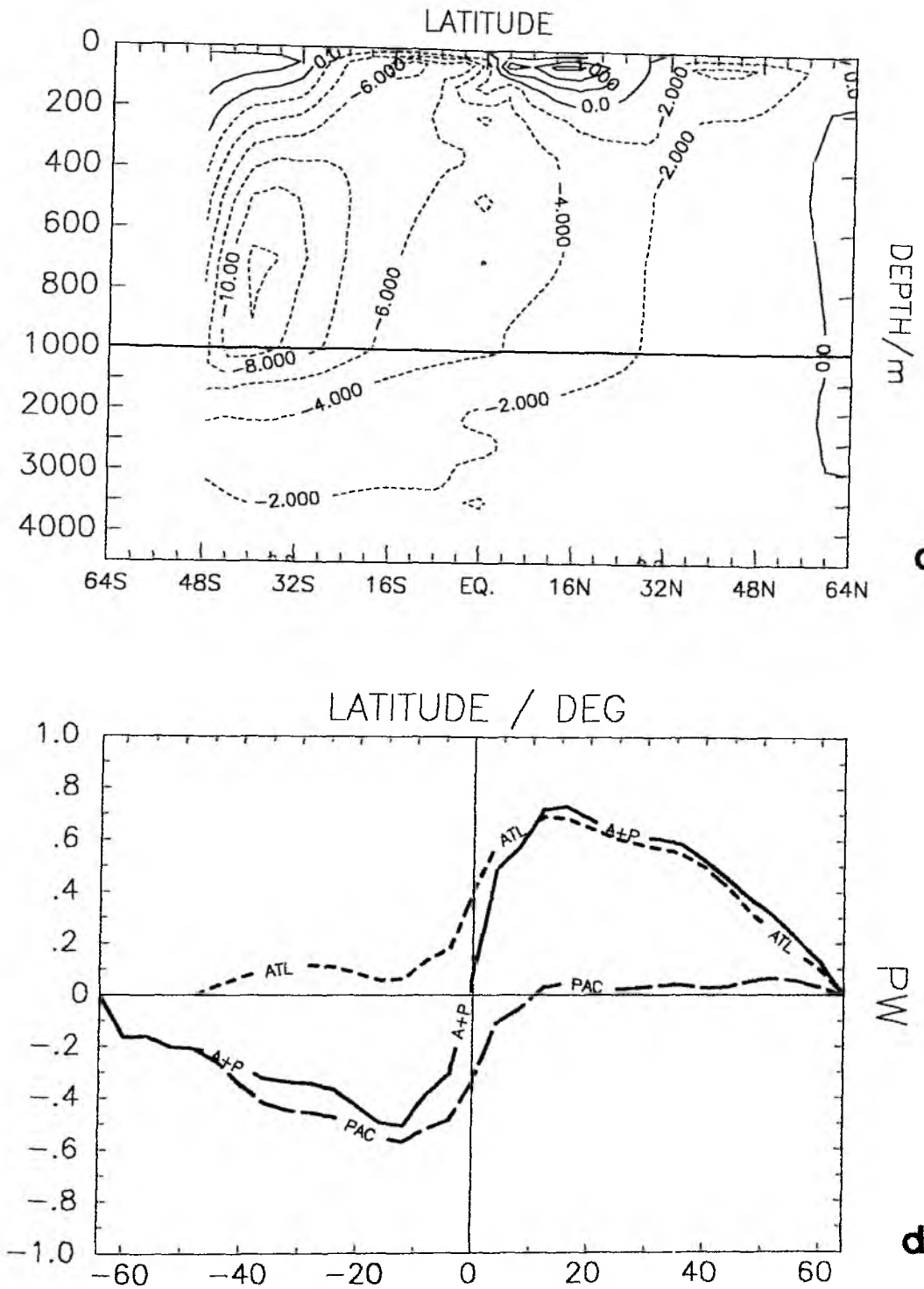

Fig. 5.8a-d: Final state of experiment GE4b with P-E taken from the global spin-up. Surface salinity in psu (a), Atlantic meridional stream function in Sv (b), Pacific meridional stream function in Sv (c), northward heat transport in PW for Atlantic (ATL), Pacific (PAC) and the two basins combined (A+P) (d).

Experiment GS9 starts from the steady state GE1b and uses HSAV as freshwater fluxes. Imposing an (E-P) anomaly of twice the strength of the one from GS7 (0.36 m/y excess evaporation over the Pacific, 0.36 m/y excess precipitation over the Atlantic, both north of 44°N), causes both oceans to flip to the opposite state, along the lines speculated about by BROECKER et al. (1985). The cessation of NADW formation occurs within 25 years, the build-up of "NPDW" formation takes about 100 years.

From all results described in Chapters 4 and 5 it is clear that any reliable perturbation experiment (or coupled ocean-atmosphere model run) should start not from a spin-up won with a Newtonian law for surface salinity, but from a reference state obtained with mixed boundary conditions. This avoids any of the initial adjustment processes like the shift of convective activity to smaller scales, or, even worse, the drift away to a completely different steady state, which could falsely be attributed to a "CO_2-effect" whereas it might just reflect an inherent ocean model instability.

However, despite the fact that such a drift occurred in all model runs described here, and in F. BRYAN's (1986a, b), except when he took measures to avoid it, an initial drift does not happen necessarily. MAIER-REIMER and MIKOLAJEWICZ (1989) report that in the global Hamburg ocean model a spin-up driven by LEVITUS' (1982) surface data, remained stable or not, dependent on additional freshwater input through the St.-Lawrence-River being less or larger than 0.011 Sv. This enhanced stability is most likely due to the different (E-P) fields diagnosed from the spin-up, which already corresponds to the -+-+ state. The Atlantic transports freshwater northward across the equator at a rate of about 0.1 Sv (MIKOLAJEWICZ, 1989, pers. comm.).

After having dwelt upon the vainness of such a venture, I shall nevertheless present the result of a "realistic" perturbation experiment. HSAV is applied as (E-P) field, starting point is the equilibrium GE1b, displayed in Figs. 5.3a-f, because I feel that it shows the closest resemblance with today's ocean: Not only are the tracer fields acceptable (Figs. 5.3d,e), but in absence of precise knowledge of freshwater fluxes the least structured (and thus bias-free) field should be used, which is the one that is zonally invariant and symmetric about the equator.

The aim of the synchronous integration is to study the ocean's response to a salinity anomaly which is similar to the "Great Salinity Anomaly" of the seventies, described by DICKSON et al. (1988). It was a negative anomaly that amounted to an equivalent salt deficit of $7 \cdot 10^{13}$ kg salt and was advected through the subpolar gyre. Distributed over the two northernmost gridpoints across an entire basin and in the top 50 metres this corresponds to a negative anomaly of -0.5 psu. Since this would mean a very strong inhibition of convective activity, a smaller anomaly was applied. -0.2 psu in the Atlantic and the Pacific brings about little change in the North Pacific, but a collapse of the thermohaline circulation in the Atlantic within 10 years (Fig. 5.9). Low salinity north of 48°N inhibits NADW formation and causes a more sluggish, and at depths below 3000 m reversed deep water flow (Fig. 5.10), with the deep western boundary current being directed to the north.

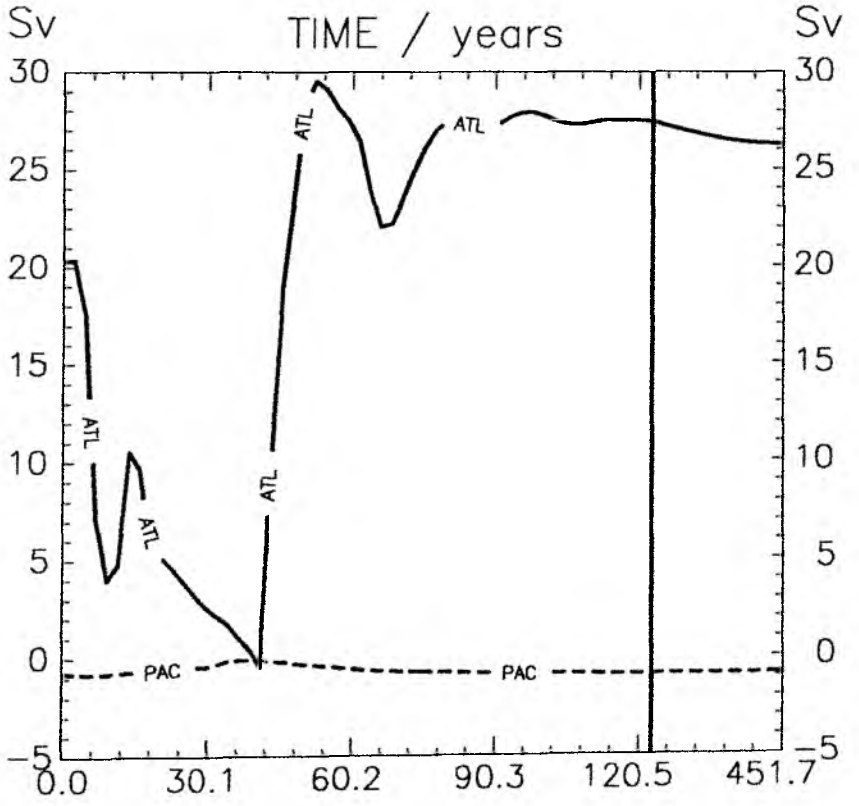

Fig. 5.9: Time series of Atlantic and Pacific meridional stream functions at 52°N, 1250 m depth, starting from the final state of experiment GE1b. A salinity anomaly of -0.2 psu has been added to the top layer of the northernmost 800 km of Atlantic and Pacific. The bold vertical line marks the transition to asynchronous integration.

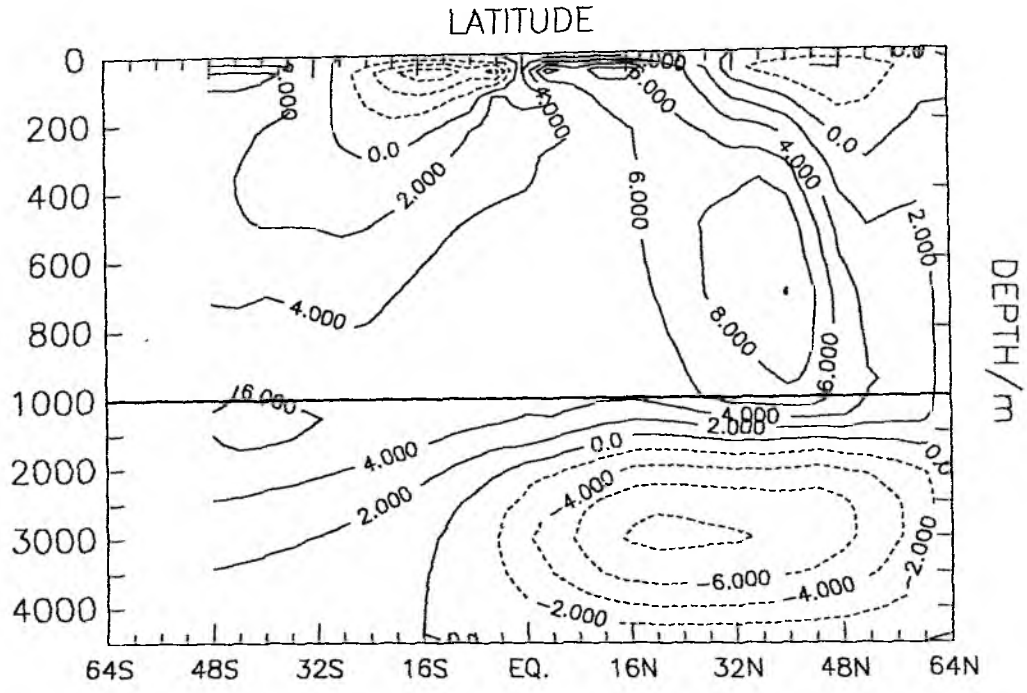

Fig. 5.10: Atlantic meridional stream function in Sv at year 27 of Fig. 5.9.

Northward salinity transports in the western parts of the North Atlantic cause sudden re-establishment of convection in the northwest, along the lines described in Sections 4.4 and 4.5. The resulting zonal surface salinity gradient is accompanied by northward geostrophic currents which transport salinity back to the north. We conclude that major temporary changes in the Atlantic thermohaline circulation due to a massive salinity perturbation like the "Great Salinity Anomaly" are possible. However, model deficiencies (no bottom topography and thus, in connection with too low resolution, no proper representation of boundary currents) and lacking knowledge of the forcing fields, especially (E-P), moreover the regional confinement of deep water formation sites and the observed salinity anomaly, make it impossible to definitely state a connection with indicated, observed low-frequency variability in the deep western boundary current (A. LIPPERT, 1989, pers. comm.).

6. CONVECTIVE ADJUSTMENT, MIXED BOUNDARY CONDITIONS AND HEAT-SALT OSCILLATIONS

6.1 Basic Principles

All models described in this study that were subject to mixed thermohaline surface boundary conditions and included a convective adjustment procedure, i.e., removal of static instability, displayed oscillations of various time scales and intensities, some of which I present in this chapter. Emphasis is laid on the basic physical mechanisms acting, and on how the precise formulation of convective adjustment in a numerical ocean model influences the oscillations.

The prototype of a convective heat-salt oscillator was described by WELANDER (1982), and is displayed in a further simplified version. The model consists of a well-mixed water layer of fixed depth, overlying a water reservoir of given temperature T_0 and salinity S_0 (Fig. 6.1). The top layer is assumed isolated from the reservoir in the case of static stability, under static instability some rapid mixing occurs, the exact formulation of which is discussed below. Coupling to the atmosphere is achieved via a Newtonian law for temperature, while the salinity field is driven by a positive equivalent salinity flux (i.e., freshwater loss). If the apparent atmospheric temperature T_A is larger than T_0, the system will go into self-sustained oscillations (Fig. 6.2):

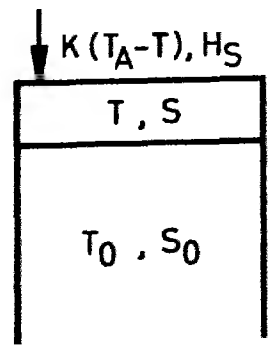

Fig. 6.1: Heat-salt oscillator after WELANDER (1982). See text for definitions.

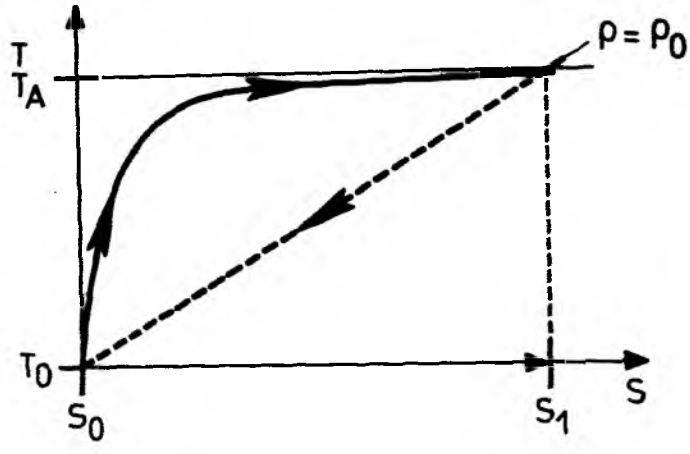

Fig. 6.2: Phase-space trajectory of the oscillator in Fig. 6.1, if complete mixing is assumed in the case of static instability.

Suppose the top layer to initially have the same properties as the reservoir, i.e. T_0 and S_0. Mixed layer temperature will then rise rapidly and asymptotically reach T_A. Meanwhile, salinity steadily increases until it arrives at the critical value S_1, at which surface density is equal to reservoir density ρ_0. If S is increased even further, static instability occurs and the top layer is mixed with the reservoir, assumed infinitely large.

The result of the mixing process is highly dependent on the details of its parameterization. If mixing is complete, i.e., the top layer takes on the reservoir values T_0, S_0, the cycle starts over again, in precisely the same manner as before. If, however, mixing is incomplete, which may be due to the numerical formulation, the top layer ends up at an arbitrary point along the mixing line. Temperature and salinity will rise again, and when the phase space trajectory now crosses the $\rho = \rho_0$ line its properties are slightly different from the first time. Likewise it will have different temperature and salinity after the mixing process.

6.2 Convective Adjustment in the GFDL Model

Any non-complete convective adjustment will result in irregular convective activity, both in strength and temporal behaviour. Despite their simplicity, these considerations also apply to the GFDL ocean model: It makes no principal difference if temperature and salinity are raised by surface fluxes or, e.g., poleward advection. Consequently, it must be investigated in how far convective overturning in an ocean model is, or should be, complete.

The hydrostatic approximation eliminates vertical accelerations and thus explicit representation of convection in a large-scale model. From a physical point of view, it would be attractive to model convective overturning as being smoothly dependent on the density difference between upper and lower layer: In a model, one compares mean potential densities over an area of (typically) 100 x 100 km^2, or even more, whereas the convection "chimmneys" have horizontal scale of 10 km or less (KILLWORTH, 1983). Taking short weather events into account, there will be spots of static instability in a grid cell whereas the mean density still is stably stratified, though weakly. Moreover, the vertical acceleration is likely to depend on the stratification.

However, the numerical implementation would introduce additional noise as can be seen from Fig. 6.2: Convection sets in as soon as a time step produces an unstable state. Changing the time step would also change the stratification, prior to the mixing, and the resulting state is highly dependent on which of these time steps has been chosen. Complete mixing has thus the advantage of producing a result which is better predictable, more regular and independent of the length of the time step. Given further how little is known about convection, it is still appropriate to parameterize it by instant mixing, as KILLWORTH (1983) concludes.

Convective adjustment in a general circulation model does not result in a simple replacement of upper layer properties by reservoir values, of course. Still, the above reasoning about the usefulness of complete vertical mixing is valid: Advective transports and surface fluxes smoothly change temperature

and salinity, so any complete mixing of a high-latitude surface box with the underlying water will create a well-determined result, which is going to be repeated regularly. The standard GFDL model, however, does not exhibit this regularity: F. BRYAN (1986a) reports on intermittent convective activity, which finally leads to a spontaneous freshening of surface water, after the model has failed to predict a convective event for too long a time, and this freshening in turn triggers the halocline catastrophe.

A closer inspection of the standard convection scheme in the GFDL model (COX, 1984) explains this irregularity: During one pass through the algorithm, boxes 1 and 2, 3 and 4 and so on are compared and mixed, if necessary. On the second pass, boxes 2 and 3, 4 and 5 and so on are checked (Fig. 6.3). The number of these double-pass iterations, N, is a freely variable parameter. Obviously it takes at least $K_{max}/2N$ time steps until any information about density input at the surface reaches the bottom, where K_{max} is the number of vertical layers. The unwanted dependence on N, especially under seasonally varying forcing and longer timesteps, has been pointed out by SMITH (1989).

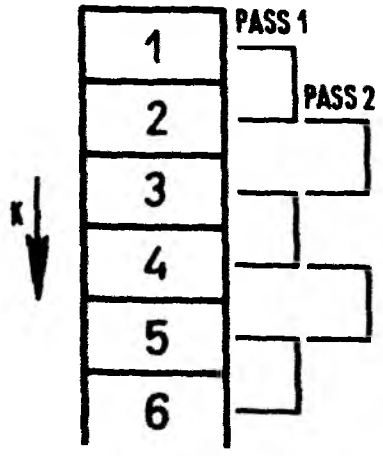

Fig. 6.3: Convective adjustment scheme of the GFDL model.

However, even under constant forcing the standard algorithm only asymptotically approaches a truly stable state: Suppose the column to be neutrally stratified initially, and a positive surface density input is imposed. Since always only two vertically adjacent boxes are checked and mixed, instability will never really disappear: Under convective adjustment, every box shares its density anomaly with its lower neighbour, so density decreases with depth. Any stabilization between boxes K and K+1 will be removed again, as soon as K+1 is mixed with K+2.

This effect, though small, has its consequences for the stability of the steady states. Firstly, they are dependent on time step length and N, the number of iterations in the convection scheme. The one-hemisphere model was spun up using wind stress, apparent atmospheric temperature and restoring salinity from Fig. 4.1. Using Δt = 5 days, N = 3, results in a "steady state" that has a basin-averaged heat uptake of 0.03 W/m^2, a value which could not be reduced by proceeding with the integration. Shifting over to either a larger N (N = 10) or a shorter time step (2 hours, i.e., synchronous integration) both rapidly raised the mean heat flux to about 0.5 W/m^2, under identical Newtonian boundary conditions for θ and S, indicating that for a different choice of parameters the model evolved towards a slightly different state.

Because of this drift it was decided to employ the convective adjustment scheme that had been used successfully in the 2-D model. The basic idea is that whenever two vertically adjacent boxes have been mixed, they are treated as a unit in all further iterations, at a specified time step. After K_{max}-1 iterations complete stability is guaranteed.

The results of this procedure are very satisfactory: After the same integration time of the spin-up as before (Experiment S1 from Table 1), the spatially averaged surface heat flux is as low as $0.5 \cdot 10^{-4}$ W/m^2, almost a factor of 1000 less. More importantly, no drift occurs when the time step is changed from 5 days to 2 hours, still under Newtonian boundary conditions for salinity as well. As already described in Section 4.4, the state remains stable even under mixed boundary conditions, if no anomaly is added.

One has to keep in mind, however, that these results are satisfactory from a numerical point of view: The noise level inherent in the model has been lowered, rendering it better predictable. From a physical point of view, noise is an essential part, especially of the forcing functions. As the spontaneously arising halocline catastrophe in F. BRYAN's (1986a,b) experiments shows, only little noise is sufficient to trigger an instability, demonstrating that noise should be included to identify equilibria that are only marginally stable. The advantage of the convective adjustment scheme used here is that it makes it easier to explicitly specify the noise level one wants to impose, instead of using model noise of unknown characteristics. Finally, note that the discussion about convective adjustment refers to the GFDL model only, the Hamburg model, for example, exchanges box properties in case of static instability (MAIER-REIMER, 1989, pers. comm.). The consideration presented here may be an improvement of the GFDL model, but any further comparison between different convection schemes is beyond the scope of this study.

6.3 Heat-Salt Oscillations in the GFDL Model

The time scale of the heat-salt oscillator described in Fig. 6.1 can be estimated as

$$\Delta t = \frac{\alpha(T_A - T_O)}{\beta S_O} \cdot \frac{D}{E - P} \qquad (6.1)$$

using Equ. (4.12), where D is the depth of the top layer and (E-P) given in m/y. Using D=50m, E-P=0.4 m/y and $T_A - T_O = 1°C$ yields a period of about one year. Under weaker thermal stratification this can be shorter, of course, but also much longer time scales are conceivable, e.g., if the freshwater loss is compensated by advection. Thus in a model with mixed boundary conditions oscillations on virtually all time scales can occur, dependent on the precise interplay between advective transport and surface fluxes.

The most spectacular oscillation (albeit in an unrealistic parameter range) was described in Section 4.5, where the inverse circulation of the

1-hemisphere model without wind stress was shown to regularly undergo periods of enormous convective activity, about 6500 years apart. During the convective phase, additional oscillations on a time scale of 20 years are observed. The coherence and strength of this phenomenon is provided for by large-scale advection and diffusion, shaping the specific background stratification. Nevertheless, the convective activity is started by a process as described here, since the first convective event is caused by slow salinity increase at the surface.

The other end of the spectrum is displayed in Fig. 6.4. It shows the time development of the anomaly experiment W2 (see Table 2) with the one-hemisphere model, where a small positive (+0.01 psu) salinity anomaly was added initially. From the time series of the meridional stream function at 56°N, 700 m depth one recognizes the initial amplification of the circulation, followed by the rapid collapse and the gradual re-establishment.

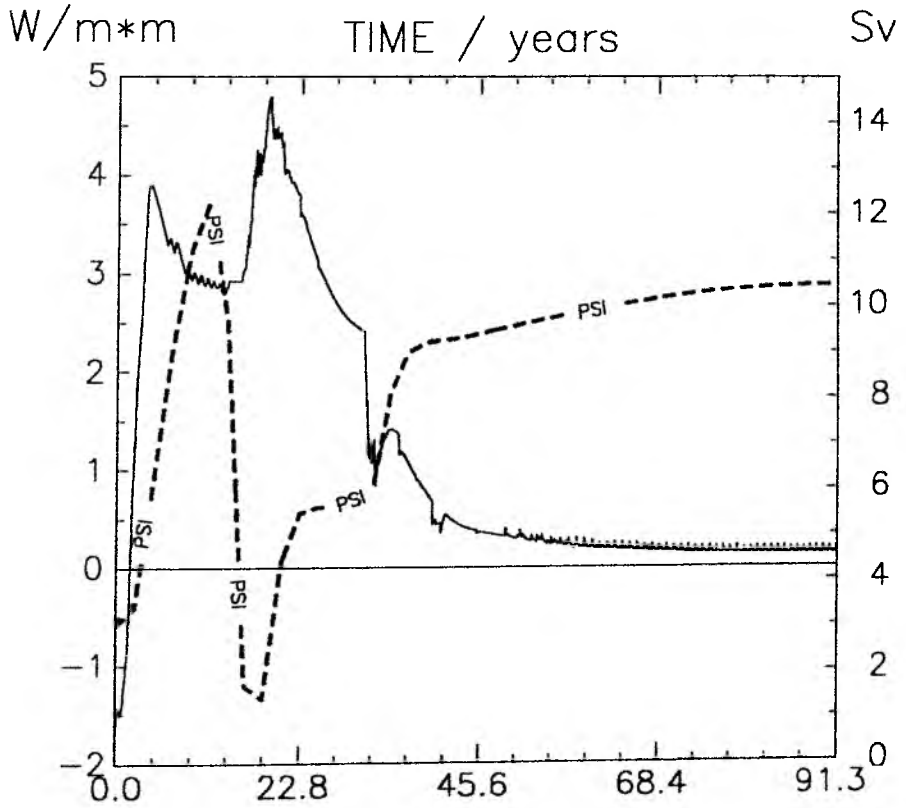

Fig. 6.4: One-hemisphere GFDL model, including wind stress (experiment W2). Time series of basin averaged heat uptake in W/m^2 (solid curve) and the meridional stream function in Sv at 56°N, 700 m depth (dashed curve) after a small positive salinity anomaly has been added to the spin-up state S1.

Also shown in Fig. 6.4 is a high-resolution (sampled is the mean over 100 time steps, i.e., about 8 days) time series of the basin-averaged heat uptake, displaying the very early enhanced convective heat loss, followed by reduced convective activity, associated with net heat gain. After 50 years regular oscillations start with a period of about one year, and an amplitude of somewhat less than 0.1 W/m^2 about a mean of 0.25 W/m^2.

These small regular oscillations did not occur in all experiments, and since they have no dynamical significance, i.e., no effect on the large-scale circulation, I shall not discuss them further. Suffice it to mention that they persist even after shifting over to asynchronous integration (with a time step of 5 days), but are likely to disappear when the system approaches its equilibrium.

In the global model an oscillation appears which is in amplitude and period in between the other two. It is present in the final "-+-+"-state (i.e., the one forming NADW but no Northern Deep Water in the Pacific), but only if the freshwater fluxes are the ones diagnosed from the spin-up. Fig. 6.5 shows the time series of total heat uptake and meridional overturning of Atlantic and Pacific combined, at 48^0S which is the southern edge of the continents. The integration was performed synchronously, and the surface heat flux sampled as a mean over 20 time steps, i.e., with 40 hours resolution. Note that this experiment is not identical with experiment GE4b (see Table 4), displayed in Figs. 5.8a-d, since again the (E-P) field contains the 5% deviation compared with the exact spin-up values, due to the code error already mentioned in Section 4.5. This difference is insignificant here, since the stability of the original state is not the topic.

The oscillations are fairly regular, with a period of 25-30 years, and maximum variations of 2 W/m^2 in the heat flux and 4 Sv in total transport. The latter is time-lagged by 4 years, which is just the advective time scale in the model ACC (note that its length is only about 9000 km, and zonal surface velocity is 7.5 cm/s on average, in the middle of the channel). The variation in meridional transport is split equally between Atlantic and Pacific.

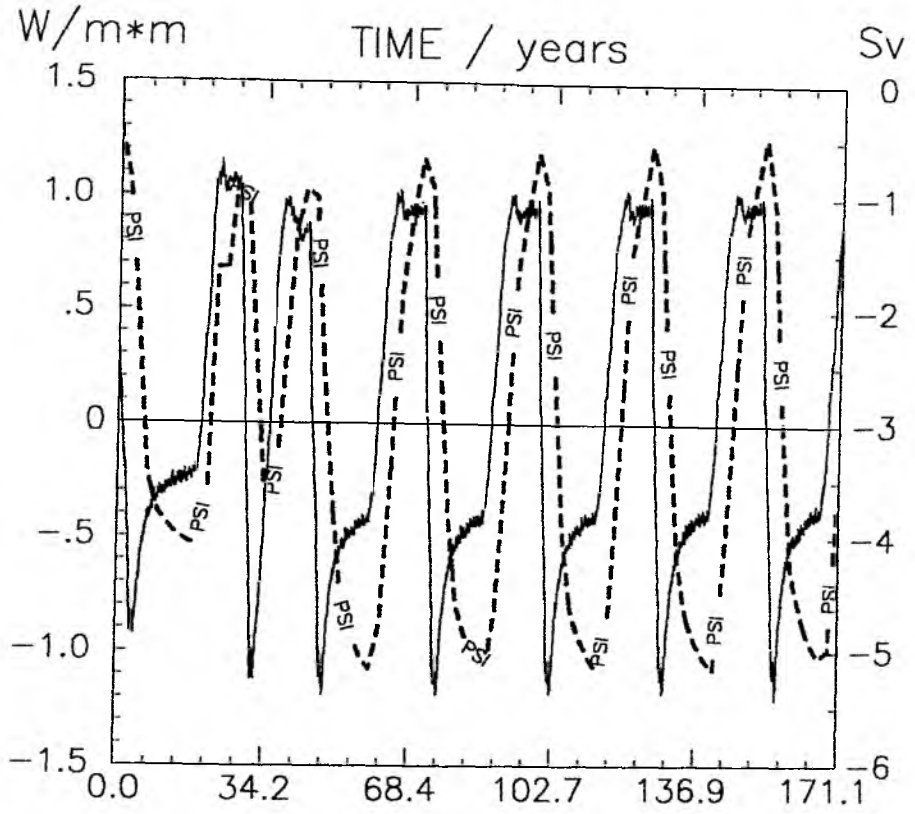

Fig. 6.5: Global GFDL model, P-E from global spin-up, plus 5% amplification, "−+−+"-state (the "conveyor belt"). Time series of basin averaged heat uptake in W/m^2 (solid curve) and the meridional stream function in Sv at 48°S, 1250 m depth (both basins combined, dashed curve).

The changes in net heat uptake are associated with varying convective activity which is most pronounced at 54°S. Figs. 6.6a-d show zonal temperature sections, which in this case are more instructive than salinity sections, during one cycle of the oscillation, starting at year 112 in the chronology of Fig. 6.5.

Convection reaches down to almost 2000 m, at greater depth both temperature and salinity are stably stratified (Fig. 6.6a). From the heat flux curve it is evident that at year 112 anomalous convective activity has lost about half its maximum strength, and the system seems to settle. However, low salinity surface water in the western Pacific region leads to interruption of convection (Fig. 6.6b). The pool of fresh water is rapidly spread over

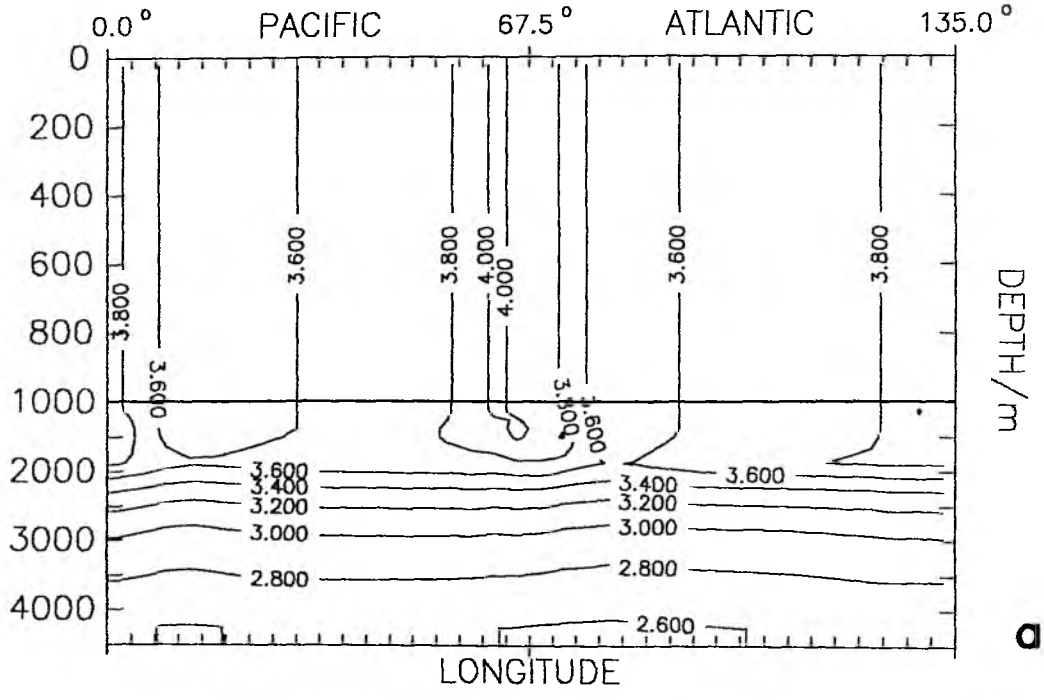
0.0 °
PACIFIC
67.5 °
ATLANTIC
135.0 °
0
200
400
600
800
1000
2000
3000
4000
DEPTH/m
LONGITUDE
3.800
3.600
4.000
3.400
3.200
3.000
2.800
2.600
a

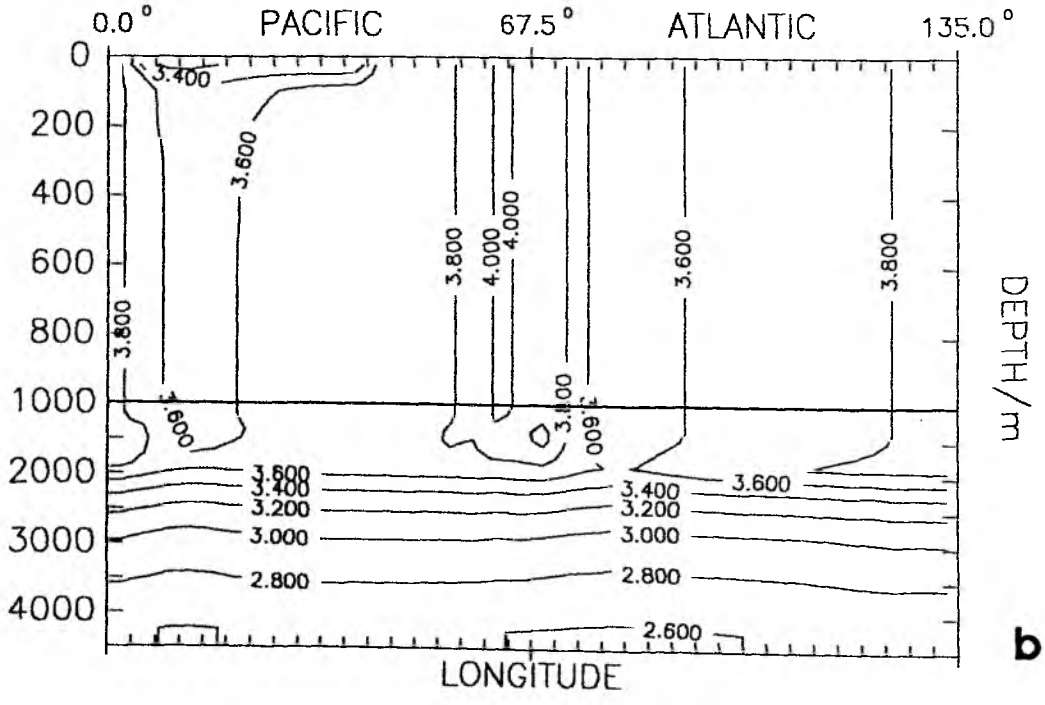
0.0 °
PACIFIC
67.5 °
ATLANTIC
135.0 °
0
200
400
600
800
1000
2000
3000
4000
DEPTH/m
LONGITUDE
3.400
3.600
3.800
4.000
3.200
3.000
2.800
2.600
b

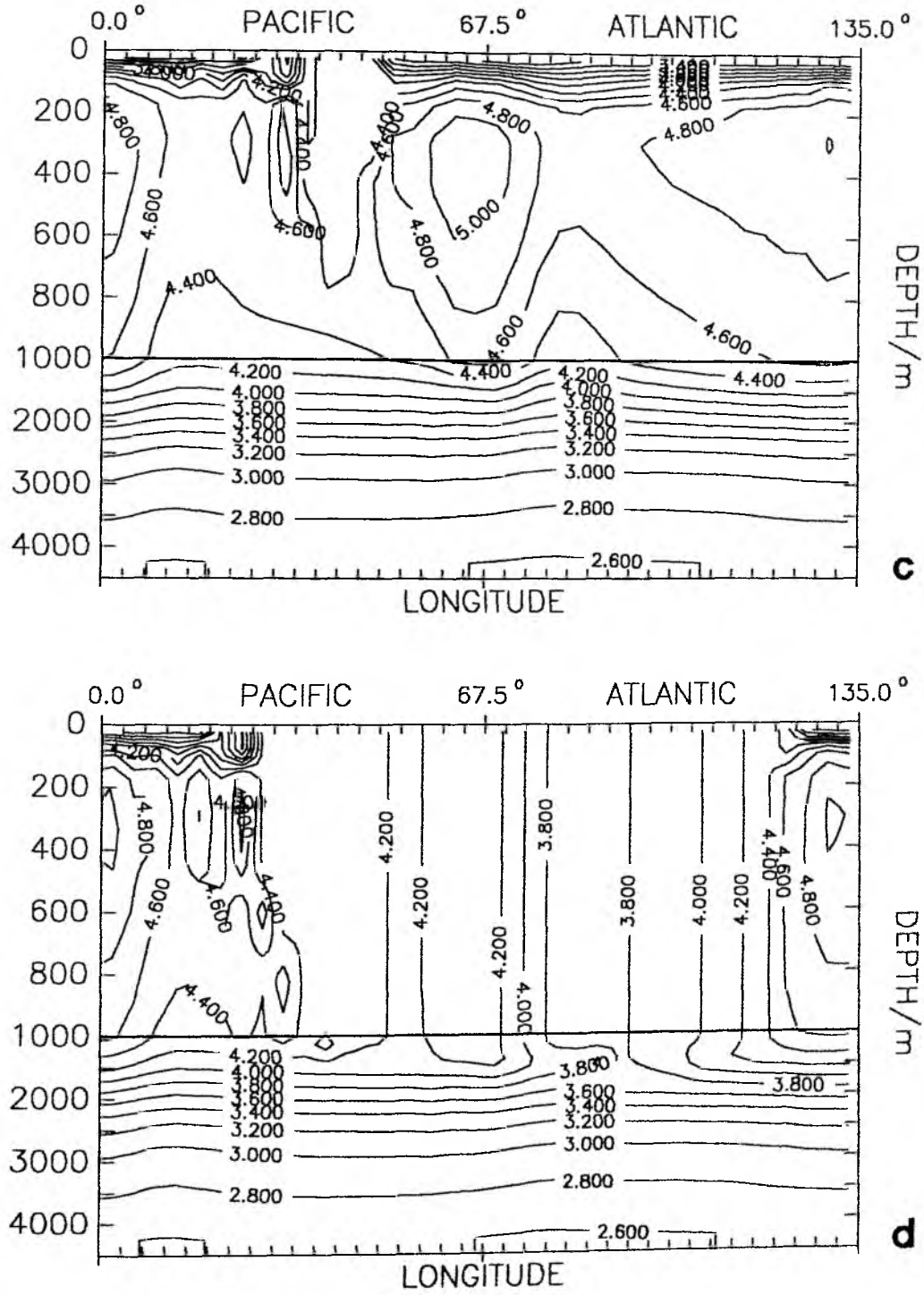

Fig. 6.6a-d: Global GFDL model, P-E from global spin-up, plus 5% amplification, "-+-+"-state (the "conveyor belt"). Zonal temperature sections across 54°S over one cycle of the oscillations visible in Fig. 6.5. Year 112 (a), year 114 (b), year 126 (c), year 128 (d), in the chronology of Fig. 6.5.

the whole latitude circle, and convection stops everywhere. Fig. 6.6c shows that surface temperatures have dropped, while the depths above 2000 m are warmed by more than 1°C, especially where southward directed currents are strong.

Again, this state is unstable: Slowly growing surface salinities between 20°E and 30°E finally lead to static instability (Fig. 6.6c), which rapidly propagates eastward (Fig. 6.6d), until the whole area is again vertically mixed down to 2000 m.

It has not been possible to give a complete account of the mechanisms driving the oscillation. Along 54°S there exist regions both with excess evaporation and excess precipitation (the freshwater flux has the same structure as the spin-up heat flux, see Fig. 5.2e). Convection is first interrupted where the mainly zonal current has transported a water parcel through an area with net water input, the opposite is true for the re-establishment of convection. However, it is not clear why these changes always start south of the Pacific. Also, the variations in meridional overturning can be explained only qualitatively: When convection stops, surface salinity and thus surface density decrease, likewise the zonal current and consequently southward flow in the channel (Section 5.2, Equ. 5.5). The Atlantic thermohaline circulation is directed northward at depths above 1500m (Fig. 5.8b), so weakened meridional flow in the ACC means enhanced Atlantic meridional overturning. The opposite reasoning applies for the Pacific, note that an increase in stream function value there means reduced meridional circulation.

Regarding how poorly the ACC is represented in this model, and how sensitive the existence of the oscillations is to the details of the (E-P)-forcing, it is not useful trying to connect them to any observed variability. Rather, they should be considered another manifestation of the system's ability to go into self-sustained oscillations of widely varying amplitudes and time scales, pointing at the large amount of inherent variability of an ocean model, and thus of the real ocean, even under constant forcing.

7. SUMMARY AND CONCLUSIONS

7.1 Summary of the Model Results

In this study I have tried to identify all possible, qualitatively different equilibria of the global thermohaline circulation, using idealized ocean models. The processes leading to a transition between different steady states were also investigated in detail. The variety of the models employed comprise box models, a two-dimensional, meridional-plane model and the general circulation model (GCM) developed at the Geophysical Fluid Dynamics Laboratory (GFDL) in Princeton.

The crucial feature common to all models is a coupling of the temperature and salinity fields to the atmosphere that is correct to lowest order: Whereas sea surface temperature (SST) is prescribed, or restored to prescribed values with a time constant of typically one month, a flux condition for salinity is formulated at the ocean surface (mixed boundary conditions). Thus the close coupling of SST anomalies to the surface heat flux and the independence of evaporation minus precipitation (E-P) of the surface salinity field are accounted for.

Box models display the basic mechanism that leads to the existence of multiple equilibria under identical boundary conditions: The net surface freshwater input at high latitudes can be transported to low latitudes by either vigorous circulation and small salinity differences, or sluggish flow and large salinity contrasts, the latter with two flow directions. There exist two stable solutions (STOMMEL, 1961): the fast circulation with poleward surface flow (positive circulation) and the sluggish circulation with equatorward surface flow (inverse circulation).

Using a six-box model of one ocean basin, I demonstrated that two different advective feedback mechanisms are present that may cause a transition to a different steady state. One of them is well-known and active in the two-box model (STOMMEL, 1961), the other one is new and associated with cross-equatorial instability. This causes a symmetric circulation with poleward surface flow in both hemispheres to undergo a transition to an asymmetric steady state, under symmetrical forcing. However, if north- and south-

equatorial regions are coupled strongly enough, the cross-equatorial instability is absent under infinitesimal perturbations.

Attributing a merely passive role to the Indian Ocean, as regards global thermohaline circulation, a global box model comprises the four hemispheres of the Atlantic and the Pacific, coupled through the Southern Ocean. This model principally allows for 16 stable equilibria, two in each hemisphere. The analysis of the stability to finite amplitude perturbations suggests that circulations asymmetric about the equator are favoured. Especially the symmetric state with positive circulation everywhere, i.e., surface flow directed polewards in all hemispheres, is not very likely to be realized.

The 2-D model demonstrates that the results from the very crude box models hold even under higher spatial resolution. The positive circulation symmetric about the equator is unstable to infinitesimal perturbations, and a single, pole-to-pole circulation cell emerges, with substantial cross-equatorial heat transport. The introduction of convective adjustment, i.e., removal of static instability, drastically increases the sensitivity of the model circulation to negative salinity anomalies: Interruption of convection in areas with excess (P-E) leads to longer residence time of water parcels at the surface and thus further freshening. This process is a powerful trigger for the advective feedback mechanisms that were identified by the use of the box models.

The GFDL GCM of one idealized ocean hemisphere was used to study the "polar halocline catastrophe" (F. BRYAN, 1986a,b) in detail. An equilibrium spun up with effectively prescribed surface temperatures and salinities is unstable to salinity anomalies as small as 0.01 psu: Within twenty years a strong halocline develops at high latitudes, deep water formation is inhibited and the thermohaline circulation collapses, in a wide variety of experiments. However, the positive circulation is re-established within another twenty years, if wind stress is present, because wind-induced northward salinity transports persist and prevent an even further freshening of high-latitude surface waters. The final state closely resembles the initial one, but convection is confined to much smaller areas than before.

The inverse state in one hemisphere (i.e., surface flow equatorward, on zonal average) is ruled out because of the dominant wind-driven near-surface transports. With thermohaline forcing only, the inverse circulation emerges as quasi-steady state after the initial collapse, with a warm, saline deep ocean. However, extremely strong convective events, 6500 years apart, lead to a complete cooling of the deep ocean within 100 years, associated with an enormous meridional flow (maximum more than 200 Sv). Subsequently, the system returns to the inverse mode.

To verify the existence of multiple equilibria of the global thermohaline circulation I used the GFDL model of an idealized system Atlantic-Pacific-Circumpolar Current, with two identical ocean basins. The spin-up, forced by effectively prescribed surface temperatures and salinities, has tracer fields symmetric about the equator, but a highly asymmetric meridional circulation due to the presence of the ACC. Under mixed boundary conditions, this state was found to be unconditionally unstable, with two different sets of freshwater fluxes.

With the global GFDL model, three essentially different steady states were found, under exactly the same boundary conditions. The latter were specified such that wind stress, SST and freshwater fluxes were identical in the model's Pacific and Atlantic. One of the equilibria corresponds to the observed global thermohaline circulation pattern: The Atlantic produces North Atlantic Deep Water, but no deep water is formed in the North Pacific. As a consequence of the meridional flow, model heat transports are purely northward in the Atlantic and almost purely southward in the Pacific.

The second equilibrium state forms Northern Deep Water in both oceans, the third no Northern Deep Water at all. Sinking occurs in the Southern Hemispheres, just north of the ACC. Since the basins are interchangeable in the model, a fourth steady state, with "North Pacific Deep Water" but no NADW, is equivalent to the first.

Which of the three essentially different equilibria is favoured depends strongly on the choice of the surface freshwater fluxes; relatively small variations in (E-P) completely change preference.

Transitions from one equilibrium to another are accomplished by (E-P)-differences between the two oceans that have the observed order of magnitude.

Under mixed boundary conditions, all models including convective adjustment displayed oscillations of various time scales and intensities. I presented some oscillations in detail, moreover, I showed that the convective adjustment scheme I employed in the 2-D and the 3-D models, which differs from the standard GFDL model procedure, reduces the noise level inherent in the model.

7.2 Conclusions

The existence of multiple steady states of the thermohaline circulation is a very robust phenomenon that occurs in all ocean models used in this study. The global box model suggests that there is a maximum of 16 equilibria of the global thermohaline circulation. Four of these could be shown to exist in the global GFDL model. Seven are eliminated because they contain inverse circulations (i.e., equatorward near-surface flow, on zonal average) symmetric about the equator. These states are ruled out by wind influence, as the one-hemisphere GFDL model shows. The remaining five equilibria contain positive circulations symmetric about the equator (i.e., sinking at both high latitudes of an ocean basin), which are highly unlikely to exist: They proved to be very sensitive to perturbations, in all models used. Therefore I conclude that there exist four different equilibria of the global thermohaline circulation.

The existence of multiple steady states and the demonstrated sensitivity of the circulation patterns to relatively small changes in (P-E) has far-reaching consequences for any attempt to realistically simulate the global thermohaline circulation and its changes. To properly predict which of the several stable modes of operation is actually chosen requires a much more precise knowledge of the freshwater fluxes than is currently available. This deficiency also affects coupled ocean-atmosphere models since they still predict precipitation rather poorly. Only if the hydrological cycle

is known much better than today, the global thermohaline circulation and especially its sensitivity to perturbations can be simulated with the desired degree of accuracy.

REFERENCES

BAUMGARTNER, A. and E. REICHEL, 1975: Die Weltwasserbilanz. Oldenbourg, München, 179 pp.

BENDER, C.M. and S.A. ORSZAG, 1978: Advanced Mathematical Methods for Scientists and Engineers. Mc Graw-Hill, Singapore, 593 pp.

BOYLE, E.A. and L. KEIGWIN, 1987: North Atlantic thermohaline circulation during the past 20,000 years linked to high-latitude surface temperature. Nature 330, 35-40.

BRASS, G.W., J.R. SOUTHAM and W.H. PETERSON: Warm saline bottom water in the ancient ocean. Nature 296, 620-623.

BROECKER, W.S. 1987: Unpleasant surprises in the greenhouse? Nature 328, 123-126.

BROECKER, W.S. and T.H. PENG, 1982: Tracers in the Sea. Lamont-Doherty Geological Observatory, Columbia University, Palisades, New York, 690 pp.

BROECKER, W.S., D.M. PETEET and D. RIND, 1985: Does the ocean-atmosphere system have more than one stable mode of operation? Nature 315, 21-26.

BRYAN, F., 1986a: Maintenance and variability of the thermohaline circulation. Ph.D. Thesis. Princeton University, 254 pp.

BRYAN, F., 1986b: High-latitude salinity effects and interhemispheric thermohaline circulation. Nature 323, 301-304.

BRYAN, F., 1987: Parameter sensivity of primitive equation ocean general circulation models. J. Phys. Oceanogr. 17, 970-985.

BRYAN, K., 1962: Measurements of meridional heat transport by ocean currents J. Geophys. Res. 67, 3403-3414.

BRYAN, K., 1969: A numerical method for the study of the circulation of the world ocean. J. Comput. Phys. 3, 347-376.

BRYAN, K., 1984: Accelerating the convergence to equilibrium of ocean-climate models. J. Phys. Oceanogr. 14, 666-673.

BRYAN, K. and M.D. COX, 1972: An approximate equation of state for numerical models of the ocean circulation. J. Phys. Oceanogr. 2, 510-514.

BRYAN, K. and L.J. LEWIS, 1979: A water mass model of the world ocean. J. Geophys. Res. 84, 2503-2517.

BRYAN, K. and M.J. SPELMAN, 1985: The ocean's response to a CO_2-induced warming. J. Geophys. Res. 90, 11,679-11,688.

BRYAN, K., S. MANABE and R. PACANOWSKI, 1975: A global ocean-atmosphere climate model. Part II: The oceanic circulation. J. Phys. Oceanogr. 5, 30-46.

COX, M.D., 1984: A primitive equation, 3-dimensional model of the ocean. GFDL Ocean Group Tech. Rep. No 1, GFDL/ Princeton University.

COX, M.D., 1989: An idealized model of the world ocean. Part I: The global-scale water masses. J. Phys. Oceanogr., 19, 1730-1752.

COX, M.D. and K. BRYAN, 1984: A numerical model of the ventilated thermocline. J. Phys. Oceanogr. 14, 674-687.

DAVEY, M.K., W.W. HSIEH and R.C. WAJSOWICZ, 1983: The free Kelvin wave with lateral and vertical viscosity. J. Phys. Oceanogr. 13, 2182-2191.

DICKSON, R.R., J. MEINCKE, S.A. MALMBERG, A. LEE, 1988: The "Great Salinity Anomaly" in the northern North Atlantic 1968-1982. Prog. Oceanogr. 20, 103-151.

DUPLESSY, J.C., N.J. SHACKLETON, R.G. FAIRBANKS, L. LABEYRIE, D. OPPO and N. KALLEL, 1988: Deepwater source variations during the last climatic cycle and their impact on the global deepwater circulation. Paleoceanogr. 3, 343-360.

GILL, A.E., 1982: Atmosphere-Ocean Dynamics. Academic Press, London, 662 pp.

GILL, A.E. and K. BRYAN, 1971: Effects of geometry on the circulation of a three-dimensional southern-hemisphere ocean model. Deep-Sea Res. 18, 685-721.

GORDON, A.L., 1986: Interocean exchange of thermocline water. J. Geophys. Res. 91, 5037-5046.

HALL, M.M. and H.L. BRYDEN, 1982: Direct estimates and mechanisms of ocean heat transport. Deep-Sea Res. 29, 339-359.

HANEY, R.L., 1971: Surface thermal boundary condition for ocean circulation models. J. Phys. Oceanogr. 1, 241-248.

HSIEH, W.W., M.K. DAVEY and R.C. WAJSOWICZ, 1983: The free Kelvin wave in finite-difference numerical models. J. Phys. Oceanogr. 13, 1383-1397.

HSIUNG, J., 1985: Estimates of global oceanic meridional heat transports. J. Phys. Oceanogr. 15, 1405-1413.

ISEMER, H.J., J. WILLEBRAND and L. HASSE, 1989: Fine adjustment of large scale air-sea energy flux parameterization by a direct estimate of ocean heat transport. J. Climate, 2, 1173-1184.

KAWASE, M. 1987: Establishment of deep ocean circulation driven by deep-water production. J. Phys. Oceanogr. 17, 2294-2317.

KILLWORTH, P.D., 1983: Deep convection in the world ocean. Rev. Geoph. Space Phys. 21, 1-26.

LEVITUS, S., 1982: Climatological atlas of the world ocean. NOAA Tech. Pap. 3, 173 pp.

LINGENBERG, R., 1976: Einführung in die Lineare Algebra. Bibliographisches Institut, Zürich, 237 pp.

MAIER-REIMER, E. and U. MIKOLAJEWICZ, 1989: Experiments with an OGCM on the cause of the Younger Dryas. Report No. 39, Max-Planck-Institut für Meteorologie, Hamburg. Reprinted from: Oceanography 1988 (Eds.: Ayala-Castanares, W. Wooster and A. Yanez-Arancibia), UNAM Press, Mexico D.F., 87-100.

MANABE, S. and R.J. STOUFFER, 1988: Two stable equilibria of a coupled ocean-atmosphere model. Journal of Climate 1, 841-866.

MAROTZKE, J., P. WELANDER and J. WILLEBRAND, 1988: Instability and multiple steady states in a meridional-plane model of the thermohaline circulation. Tellus 40A, 162-172.

MAROTZKE, J., 1989: Instabilities and multiple steady states of the thermohaline circulation. In: Oceanic Circulation Models: Combining Data and Dynamics (Eds. D.L.T. Anderson and J. Willebrand). Kluwer, Dordrecht, 501-511.

MEAD, C.T., 1988: Asymmetries of the oceanic thermohaline circulation and meridional heat transport. Ph.D. Thesis, University of Southampton, 253 pp.

MESINGER, F. and A. ARAKAWA, 1976: Numerical Methods Used in Atmospheric Models, Vol. 1. GARP Publications Series No 17, WMO, Geneva, 64 pp.

MITCHELL, J.F.B., 1989: The "Greenhouse" effect and climate change. Rev. Geophys. 27, 115-139.

MÜLLER, P. and J. WILLEBRAND, 1989: Equations for oceanic motions. In: Landolt-Börnstein, Group V, Oceanography, Volume 3b (Ed. J. Sündermann), Springer Verlag, Berlin, 1 - 14.

NOWLIN, W.D., Jr. and J.M.Klinck, 1986. The physics of the Antarctic Circumpolar Current. Rev. Geophys 24, 469-491.

OLBERS, D. and M. WENZEL, 1989: Determining diffusivities from hydrographic data by inverse methods with applications to the circumpolar current. In: Oceanic Circulation Models: Combining Data and Dynamics (Eds. D.L.T. Anderson and J. Willebrand). Kluwer, Dordrecht, 95-139.

ÖSTLUND, H.G. and M. STUIVER, 1980: GEOSECS Pacific radiocarbon. Radiocarbon 22, 25-53.

ROOTH, C., 1982: Hydrology and ocean circulation. Progr. Oceanogr. 11, 131-149.

SCHMITT, R.W., P.S. BOGDEN and C.E. DORMAN, 1989: Evaporation minus precipitation and density fluxes for the North Atlantic. J. Phys. Oceanogr. 19, 1208-1221.

SMITH, N.R., 1989: The Southern Ocean thermohaline circulation: A numerical model sensitivity study. J. Phys. Oceanogr. 19, 713-726.

STERN, M.E., 1975: Ocean Circulation Physics. Academic Press, New York, 209 pp.

STOMMEL, H., 1961: Thermohaline convection with two stable regimes of flow. Tellus 13, 224-230.

WAJSOWICZ, R.C. and A.E. GILL, 1986: Adjustment of the ocean under buoyancy forces. Part I: The role of Kelvin waves. J. Phys. Oceanogr. 16, 2097-2114.

WALIN, G., 1985: The thermohaline circulation and the control of ice ages. Palaeogeogr., Palaeoclimatol., Palaeoecol. 50, 323-332.

WARREN, B.A., 1981: Deep circulation of the world ocean. In: Evolution of Physical Oceanography, Scientific Surveys in Honor of Henry Stommel (Eds. B.A. Warren and C. Wunsch), MIT Press, Cambridge, Mass, 42-69.

WARREN, B.A., 1983: Why is no deep water formed in the North Pacific? J. Mar. Res. 41, 327-347.

WELANDER, P., 1982: A simple heat-salt oscillator. Dyn. Atmos. Oceans 6, 233-242.

WELANDER, P., 1986: Thermohaline effects in the ocean circulation and related simple models. In: Large-Scale Transport Processes in Oceans and Atmosphere (Eds. J. Willebrand and D.L.T. Anderson). D. Reidel Publ. Co., Dordrecht, 163-200.

WHITWORTH, T.,III, and R.G. Peterson, 1985: Volume transport of the Antarctic Circumpolar Current from bottom pressure measurements. J. Phys. Oceanogr. 15, 810-816.

WILLEBRAND, J., 1989: General circulation dynamics. In: Landolt-Börnstein, Group V, Oceanography, Volume 3b (Ed. J. Sündermann), Springer Verlag, Berlin, 123 - 150.

WOLFF, J.O. and D.J. OLBERS, 1989: The dynamical balance of the Antarctic Circumpolar Current, studied with an eddy resolving quasigeostrophic model. In: Mesoscale/Synoptic Coherent Structures in Geophysical Turbulence (Eds. J.C.J. Nihoul and B.M. Jamart). Elsevier Science Publ., Amsterdam, 435-458.

WUNSCH, C., 1984: An eclectic Atlantic Ocean circulation model. Part I: The meridional flux of heat. J. Phys. Oceanogr. 14, 1712-1733.

DANKSAGUNG

Ich danke meinem Doktorvater Prof. Dr. J. Willebrand für die Betreuung dieser Arbeit, für die vielen Anregungen und stete Diskussionsbereitschaft sowie für die freundschaftliche Unterstützung, die mich während der gesamten Promotionszeit begleitet hat. Prof. Dr. P. Welander danke ich für die Anregungen, die zu der Entwicklung des in Kapitel 3 beschriebenen Modells geführt haben, und Prof. Dr. F. Schott für Hinweise, die sehr zur Verbesserung des Manuskripts beitrugen. Für die Überlassung des GFDL-Modells bin ich dem verstorbenen Herrn M. Cox sehr zu Dank verpflichtet.

Diese Arbeit entstand in der Abteilung Theoretische Ozeanographie des Kieler Instituts für Meereskunde, und ich danke allen Kolleginnen und Kollegen für das sehr angenehme und motivierende Betriebsklima. Namentlich erwähnen möchte ich Dr. Aike Beckmann, Dr. Rüdiger Gerdes, Prof. Dr. Rolf Käse, Dr. J. Kielmann und Dr. Reiner Onken, die durch ihr Interesse und ihre Hilfsbereitschaft zum Gelingen beigetragen haben. Herrn Guntram Seiß danke ich für die Mithilfe bei der Erstellung des Manuskripts und Frau Annegret Schurbohm für die Erstellung vieler Zeichnungen. Mein ganz besonderer Dank gilt Frau Sabine Trier, die in unermüdlichem Einsatz die Arbeit in die endgültige Form gebracht hat.

Die letzten Jahre wurden insbesondere dadurch zu einer angenehmen Zeit, daß ich durch die Teerunde in der "Alten Botanik" viele Kollegen und Freunde kennengelernt habe. Für Tee, Kekse, zahlreiche Gespräche und fröhliche Feiern danke ich Andreas "El Turbo" Schiller, Dr. Michael Schröder, Detlef Stammer, Dr. Thomas Viehoff, Marek Zwierz und ganz besonders Frau Birgit Klein, die als Büronachbarin alle Erfolgserlebnisse und Frustrationen miterlebte und mir stets als kompetente Gesprächspartnerin zur Verfügung stand.

Meinen Eltern danke ich für die menschliche und materielle Unterstützung, die sie mir während meiner gesamten Ausbildung haben zukommen lassen, und meiner Freundin Kirsten für alles, was sie in den letzten Monaten für mich getan hat.

BERICHTE AUS DEM INSTITUT FÜR MEERESKUNDE

Verzeichnis der veröffentlichten Arbeiten

1	(1973)	FECHNER, H.	Orthogonale Vektorfunktionen zur stetigen Darstellung von meteorologischen Feldern auf der Kugeloberfläche
2	(1974)	SPETH, P.	Mittlere Meridionalschnitte der verfügbaren potentiellen Energie für jeden Januar und Juli aus dem Zeitraum 1967 bis 1972
3	(1974)	SPETH, P.	Mittlere Horizontalverteilungen der Temperatur und der verfügbaren potentiellen Energie und mittlere Meridionalschnitte der Temperatur für jeden Januar und Juli aus dem Zeitraum 1967 bis 1972
4	(1974)	DEFANT, Fr.	Das Anfangstadium der Entwicklung einer baroklinen Wellenstörung in einem baroklinen Grundstrom
5	(1974)	FECHNER, H.	Darstellung des Geopotentials der 500 mb-Fläche der winterlichen Nordhalbkugel durch natürliche Orthogonalfunktionen
7	(1974)	SPETH, P.	Die Veränderlichkeit der atmosphärischen Zirkulation, dargestellt mit Hilfe energetischer Größen
8	(1975)	SKADE, H.	Eine aerologische Klimatologie der Ostsee. Teil I - Textband
9	(1975)	SKADE, H.	Eine aerologische Klimatologie der Ostsee. Teil II - Abbildungsband
10	(1975)	MÖLLER, H.	Bestimmungstafeln für die Fischparasiten der Kieler Bucht
11	(1975)	KEUNECKE, K.H., KOHN, H., KRAUSS, W., MIOSGA, G., SCHOTT, F., SPETH, P., WILLEBRAND, J., ZENK, W.	Baltic 75 - Physikalischer Teil Messungen des IfM, der FWG und der DFVLR
13	(1975)	RUMOHR, H.	Der Einfluß von Temperatur und Salinität auf das Wachstum und die Geschlechtsreife von nutzbaren Knochenfischen (Eine Literaturstudie)
14	(1975)	PULS, K.E., MEINCKE, J.	General Atmospheric Circulation and Weather Conditions in the Greenland-Scotland Area for August and September 1973
15	(1975)	MÖLLER, H.	Bibliography on parasites and diseases of marine fishes from North Sea and Baltic Sea
16	(1975)	LÖBE, D.	Schwermetall-Kontamination von Phytoplankton unter natürlichen Verhältnissen und in Laborkulturen
17	(1976)	BEHR, H.D.	Untersuchungen zum Jahresgang des atmosphärischen Wärmehaushalts für das Gebiet der Ostsee. Teil I - Textband
18	(1976)	BEHR, H.D.	Untersuchungen zum Jahresgang des atmosphärischen Wärmehaushalts für das Gebiet der Ostsee. Teil II - Abbildungsband
19	(1976)	BROCKMANN, Ch., MEINCKE, J., PETERS, H., SIEDLER, G., ZENK, W.	GATE - Oceanographic Activities on FRG-Research Vessels
20a 20b	(1977)	WILLEBRAND, J., MÖLLER, P., OLBERS, D.J.	Inverse Analysis of the Trimoored Internal Wave Experiment (IWEX) Part 1 Part 2
21	(1976)	MÖLLER, H.	Die Biologie des Flachwassers vor der westdeutschen Ostseeküste und ihre Beeinflussung durch die Temperatur - eine Literaturstudie
22	(1976)	PETERS, H.	GATE - CTD Data measured on the F.R.G. Ships Shipboard Operations-Calibration-Editing
23	(1976)	KOLTERMANN, K.P., MEINCKE, J., MÖLLER, T.	Overflow '73 - Data Report 'Meteor' and 'Meerkatze 2'
24	(1976)	LIEBING, H.	Grundlagen zur objektiven Ermittlung eines Bodenluftdruckfeldes für ein begrenztes Gebiet (Ostsee)
25	(1976)	SIMONS, T.J.	Topographic and Baroclinic Circulations in the Southwest Baltic
26	(1976)	KIELMANN, J., HOLTORFF, J., REIMER, U.	Data Report Baltic '75
27	(1976)	BEHRENDT, J.	Der Zusammenhang zwischen wahrem und geostrophischem Wind über der Ostsee während "Baltic '75"

28	(1977) DEFANT, Fr., SPETH, P.	Zwischenbericht der Arbeitsgruppe "Diagnose Empirischer Felder der Allgemeinen Atmosphärischen Zirkulation" im Schwerpunkt "Energiehaushalt und Zirkulation der Atmosphäre" der Deutschen Forschungsgemeinschaft
29	(1977) MEINCKE, J.	Measurements of Currents and Strafication by FRV "Anton Dohrn" during the GATE Equatorial Experiment
30	(1977) SANFORD, Th.	Design Concepts for a Shallow Water Velocity Profiler and a Discussion of a Profiler Based on the Principles of Geomagnetic Induction
31	(1977) MÖLLER, H.	Indexed bibliography on parasites and diseases of marine fish from North Sea and Baltic Sea (2nd edition)
32	(1977) BROCKMANN, Ch., HUGHES, P., TOMCZAK, M.	Data Report on Currents, Winds and Stratification in the NW African Upwelling Region during early 1975
33	(1977) SIERTS, H.W.	Meteorologische Einflüsse auf das Auftriebsgebiet vor Nordwest-Afrika
34	(1977) CUBASCH, U.	Spektren des Windes über Land und über Meer im Periodenbereich von 1 Minute bis 1 Tag
35	(1977) KAMINSKI, U.	Klassifikation der Wetterlagen über dem Wetterschiff - C - durch vertikale natürliche Orthogonalfunktionen
36	(1977) JECKSTRÖM, W.	Eine Entwicklung des Geopotentialfeldes der 500 mb-Fläche im Winter der Nordhalbkugel in natürliche Orthogonalfunktionen und eine Interpretation der Ergebnisse im Zusammenhan mit tatsächlichen synoptischen groß-skaligen Wetterlagen
37	(1977) CLAUSS, E., HESSLER, G., SPETH, P., UHLIG, K.	Datendokumentation zum meteorologischen Meßprojekt 1976
38	(1977) KIRK, E.	Objektive Analysen meteorologischer Parameter über der Kieler Bucht
40	(1978) OSTHAUS, A., SPETH, P.	Large-scale horizontal fluxes of sensible energy and of momentum caused by mean standing eddies for each January and July of the period 1967 until 1976
41	(1978) SPETH, P.	Mean meridional cross-sections of the available potential energy for each January and July of the period 1973 until 1976
42	(1978) SPETH, P.	Mean meridional cross-sections of the available potential energy for each April and October of the period 1967 until 1976
43	(1978) SPETH, P.	Mean horizontal fields of temperature available potential energy and mean meridional cross-sections of temperature for each January and July of the period 1967 until 1976
44	(1978) FECHNER, H.	Darstellung meteorologischer Felder mit endlichem Definitionsgebiet durch Reihen orthogonaler Funktionen
45	(1978) RIECKE, W.	In der Meteorologie benutzte objektive horizontale Analysenverfahren im Hinblick auf die Anwendung bei wissenschaftlichen Untersuchungen
46	(1978) OSTHAUS, A.	Die Struktur der stehenden Temperatur- und Geopotentialwellen im Januar und Juli und die durch sie hervorgerufenen Transporte von sensibler Energie und Drehimpuls
47	(1978) CORNUS, H.-P.	Untersuchungen zu Deckschichtänderungen und zur Anwendbarkeit eindimensionaler Deckschichtmodelle im äquatorialen Atlantik während GATE 1974
48	(1978) WÖRNER, F.G., KOHN, A.	Liste der Mikronekton- und Zooplanktonfänge der Deutschen Antarktis-Expedition 1975/76
49	(1978) DETLEFSEN, H.	Wasseroberflächentemperaturen und Luftdruckdifferenzen im Auftriebsgebiet vor Nordwest-Afrika von 1969-1976
50	(1978) MENGELKAMP, H.-T.	Wind-, Temperatur- und Feuchteprofile über der Ostsee während des Meßprojektes "Kieler Bucht" 1976
51	(1978) BROCKMANN, C., FAHRBACH, E., URQUIZO, W.	ESACAN - Data report
52	(1978) STROFING, R.	Die Struktur der atmosphärischen Temperatur- und Geopotentialwellen und die durch sie hervorgerufenen Transporte von sensibler Energie und Drehimpuls während eines vierteljährigen Winterzeitraums November 1967 - Januar 1968
53	(1978) SPETH, P.	Mean horizontal fields of temperature and geopotential height for each January, April, July and October for the period 1967 - 1976
54	(1978) KREY, J.(+), BABENERD, B., LENZ, J.	Beobachtungen zur Produktionsbiologie des Planktons in der Kieler Bucht: 1957-1975 - 1. Datenband
55	(1978) PAULY, D.	A preliminary compilation of fish length growth parameters
56	(1978) WITTSTOCK, R.-R.	Vergleich der aus Temperatur- und Dichtefluktuationen berechneten Vertikalgeschwindigkeit im GATE-Gebiet

57	(1978)	STRUVE, S.	Transport und Vermischung einer passiven Beimengung in einem Medium mit einem vorgegebenen Geschwindigkeitsfeld
58	(1978)	MÜLLER, H.	Effects of Power Plant Cooling on Aquatic Biota - An Indexed Bibliography -
59	(1978)	JAMES, R., WÜRNER, F.G.	Results of the Sorting of the Mikronekton and Zooplankton Material sampled by the German Antarctic Expedition 1975/76
60	(1978)	WÜRNER, F.G.	Liste der Mikronekton- und Zooplanktonfänge der 2. Deutschen Antarktis-Expedition 1977/78
61	(1978)	SCHWEIMER, M.	Physikalisch-ozeanographische Parameter in der westlichen Ostsee - Eine Literaturstudie -
62	(1979)	MÜLLER, T.J., MEINCKE, J., BECKER, G.A.	Overflow '73: The Distribution of Water Masses on the Greenland-Scotland Ridge in August/September 1973 - A Data Report -
63	(1979)	PAULY, D.	Gill size and temperature as governing factors in fish growth: a generalization of von Bertalanffy's growth formula
64	(1979)	WÜBBER, C.	Die zweidimensionalen Seiches der Ostsee
65	(1979)	KILS, U.	Schwimmverhalten, Schwimmleistung und Energiebilanz des antarktischen Krills, Euphausia superba - Ergebnisse der zweiten deutschen Antarktis-Expedition des "FFS Walther Herwig" im Südsommer 1977/78
66	(1979)	KREMLING, K., OTTO, C., PETERSEN, H.	Spurenmetall-Untersuchungen in den Förden der Kieler Bucht - Datenbericht von 1977/78
67	(1979)	RHEINHEIMER, G.	Mikrobiologisch-ökologische Untersuchungen in verschiedenen Flüssen Schleswig-Holsteins - Daten -
68	(1979)	KNOLL, M.	Zur Wärmebilanz der ozeanischen Deckschicht im GATE-Gebiet
69	(1979)	ZENK, W., SCHAUER, U., PETERSOHN, U., MITTELSTAEDT, R.U.	Bodenströmungen und Schichtungsverhältnisse in der nördlichen Kieler Bucht im März 1978
70	(1979)	REDELL, R.-D.	Winderzeugte Trägheitsbewegungen und Energiekorrelationen interner Wellen im tropischen Atlantik
72	(1979)	HERRMANNSEN, U.	Energiespektren von Temperatur, Geopotential und Wind an ausgewählten Gitterpunkten des DWD-Gitternetzes der Nordhalbkugel
73	(1979)	PERKUHN, J.	Spektrale Betrachtung der groß-skaligen Transporte von sensibler Energie und Drehimpuls an ausgewählten Gitterpunkten des DWD-Gitternetzes der Nordhemisphäre
74	(1979)	VOGL, Ch.	Die Struktur der stehenden Temperatur- und Geopotentialwellen im April und Oktober und die durch sie hervorgerufenen Transporte von sensibler Energie und Drehimpulse
75	(1980)	NIELAND, H.	Die Nahrung von Sardinen, Sardinellen und Maifischen vor der Westküste Afrikas
76	(1980)	DAMM, U.	Langfristige Veränderungen in der Verbreitung von Nordseefischen, untersucht durch Korrelations- und Varianzanalyse
77	(1980)	DAUB, P.	Wind-, Temperatur- und Feuchteprofile über der Kieler Bucht im Zeitraum April bis Oktober 1977
78	(1980)	EBBRECHT, H.-G.	Die verfügbare potentielle Energie des Planetarischen Wirbels und ihre jährliche Variation
79	(1980)	WOSNITZA-MENDO, C.	Zur Populationsdynamik und Ökologie von Tilapia rendalli (Blgr.) im Lago Sauce (Peru)
80	(1981)	ZEITZSCHEL, B., ZENK, W.	ANTARKTIS 80/81, Beobachtungen und erste Ergebnisse der "Meteor"-Reise 56 aus der Scotia-See und der Bransfield-Straße im November/Dezember 1980 (ANT I): ein nautischer und wissenschaftlicher Bericht
81	(1981)	STRUNK, H.A.	Die kinetische Energie des planetarischen Wirbels und ihre jährliche Variation
82	(1981)	PETERS, H.	Zur Kinematik eines stochastischen Feldes interner Wellen in einer Scherströmung
83	(1981)	WILLEBRAND, J.	Zur Erzeugung großräumiger Ozeanischer Strömungsschwankungen in mittleren Breiten durch veränderliche Windfelder
84	(1981)	STRAMMA, L.	Die Bestimmung der Dynamischen Topographie aus Temperaturdaten aus dem Nordostatlantik
85	(1981)	BAUERLE, E.	Die Eigenschwingungen abgeschlossener, zweigeschichteter Wasserbecken bei variabler Bodentopographie
86	(1981)	MÜLLER, H.	Feldführer zur Diagnose der Fischkrankheiten und wichtigsten Fischparasiten in Nord- und Ostsee
87a	(1981)	KIELMANN, J.	Grundlagen und Anwendung eines numerischen Modells der geschichteten Ostsee - Teil 1 -
87b	(1981)	KIELMANN, J.	- Teil 2 - (Anhang, Literatur, Abbildungen)

88	(1981)	WOODS, J.D.	The GATE Lagrangian Batfish Experiment - Summary Report -
89	(1981)	LEACH, H., MINNETT, P.J.	The GATE Lagrangian Batfish Experiment - Data Report -
90	(1981)	MOLLER, T.J.	Current and temperature measurements in the North-East Atlantic during NEADS - a data report
91	(1981)	LUPATSCH, J., NELLEN, W.	Der Zustand der Fischbestände in der Schlei und die Entwicklung der Fischerei im Zeitraum 1962 - 1981
92	(1981)	HESSLER, G.	Untersuchung bodennaher Temperatur- und Windfelder im Übergangsbereich Land-See am Beispiel der Kieler Bucht
93	(1981)	STEINHAGEN-SCHNEIDER, G.	Fucus vesiculosus als Schwermetall-Bioakkumulator - Der Einfluß von Temperatur, Salzgehalt und Metallkombination auf die Inkorporationsleistung
94	(1982)	RIEGER, K.-W.	Die räumliche und zeitliche Veränderlichkeit des meridionalen Transportes sensibler Energie im 850 und 200 mb-Niveau während eines Jahre (1975) - Teil 1 - Textband - Teil 2 - Abbildungsband
95	(1982)	MYDLA, B.	Longitudinale und zeitliche Veränderlichkeit des durch stehende und wandernde Wellen getätigten meridionalen Transportes von relativem Drehimpuls im 200 und 500 mb-Niveau in der Breitenzone von 20° bis 60°N während des Jahres 1975 - Teil 1 - Textband - Teil 2 - Abbildungsband
96	(1982)	WILLENBRINK, E.	Wassermassenanalyse im tropischen und subtropischen Nordostatlantik
97	(1982)	HORCH, A., MINNETT, P., WOODS, J.D.	CTD Measurements Made From F.S. POSEIDON During JASIN 1978 - A Data Report -
98	(1982)	ASTHEIMER, H.	Die Variabilität der Phytoplanktonschichtung in driftenden Wasserkörpern. Untersuchungen aus dem Skagerrak, Kattegat und Bornholm-Becken im März 1979
99	(1982)	QUADFASEL, D.	Über den Monsunresponse der Zirkulation im westlichen äquatorialen Indischen Ozean
100	(1982)	LEACH, A.	Spektrale Untersuchungen des Geopotentials und des Geostrophischen Windes im 200 mb-Niveau und Parametrisierung von großturbulentem meridionalen Drehimpulstransport
101	(1982)	SIEDLER, G.	SI-Einheiten in der Ozeanographie
102	(1982)	STRUVE-BLANCK, S.	Die Strömungen in der Kieler Bucht
103	(1982)	KÄSE, R., RATHLEV, J.	CTD-Data from the North Canary Basin - "Poseidon" Cruise 86/2 - 26 March - 13 April, 1982
104	(1982)	KRAUSS, W., WÖBBER, Ch.	A detailed description of a semispectral model on the ß-plane
105	(1982)	SCHAUER, U.	Zur Bestimmung der Schubspannung am Meeresboden aus der mittleren Strömung
106	(1983)	HORSTMANN, U.	Distribution patterns of temperature and watercolour in the Baltic Sea as recorded in satellite images: Indicators for phytoplancton growth
107	(1982)	WITTSTOCK, R.-R.	Zu den Ursachen bodennaher Strömungsschwankungen in der nordöstlichen Kieler Bucht
108	(1982)	SCHRÖDER, M.	Das statische Verhalten von Einpunktverankerungen bei Anströmung
109	(1982)	BREITENBACH, J., SCHRÖDER, M.	Anleitung für Benutzer des Rechenprogramms STASIP (statics of single-point moorings)
110	(1983)	BAUERFEIND, E., BOJE, R., FAHRBACH, E., LENZ, J. MEYERHÖFER, M., ROLKE, M.	Planctological and chemical data from the Atlantic at 22°W obtained in February to June 1979 ("FGGE-Equator '79")
111	(1983)	SY, A.	Warmwassersphäre - Handling and Processing of Hydrographic Data - - Technical Report -
112	(1983)	KETZLER, C.	Zur Kinematik der Gezeiten im Rockall-Gebiet
113	(1983)	FAHRBACH, E.	Transportprozesse im zentralen äquatorialen Atlantik und ihr Einfluß auf den Wärmeinhalt
114	(1983)	MÖLLER, T.J., ZENK, W.	Some Eulerian current measurements and XBT-sections from the North East Atlantic - October 1980 - March 1982 - A Data Report -
115	(1983)	VIEHOFF, Th.	Bestimmung der Meeresoberflächentemperatur mittels hochauflösender Infrarot-Satellitenmessungen
116	(1983)	MILLER, W., KÄSE, R.H.	Objective analysis of hydrographic data sets from mesoscale surveys

117	(1983)	PRICE, J.M.	Historic hydrographic and meteorological data from the North Atlantic and some derived quantities
118	(1983)	FAHRBACH, E., KRAUSS, W.,	Nordostatlantik '81 - Data Report -
119	(1983)	MEINCKE, J., SY, A.	Nordostatlantik '82 - Data Report -
120	(1983)	HORCH, A., BARKMANN, W., WOODS, J.D.	Die Erwärmung des Ozeans hervorgerufen durch solare Strahlungsenergie
121	(1983)	SINN, M.	Berechnung der solaren Bestrahlung einer Kugel sowie des menschlichen Körpers aus Werten der Global- und Himmelsstrahlung
122	(1984)	ASMUS, H.	Freilanduntersuchungen zur Sekundärproduktion und Respiration benthischer Gemeinschaften im Wattenmeer der Nordsee
123	(1984)	BREY, Th.	Gemeinschaftsstrukturen, Abundanz, Biomasse und Produktion des Makrozoobenthos sandiger Böden der Kieler Bucht in 5 - 10 m Wassertiefe
124	(1984)	KREMLING, K., WENCK, A.	Chemical Data from the NW African Upwelling Region ("Auftrieb '75" and "Ostatlantik-Biozirkel 1983")
125	(1984)	STRAMMA, L.	Wassermassenausbreitung in der Warmwassersphäre des subtropischen Nordostatlantiks
126	(1984)	JÄGER, T., NELLEN, W., SELL, H.	Beleuchtete Netzgehegeanlagen zur Aufzucht von Fischbrut bis zur Setzlingsgröße - Eine Bauanleitung und Aufzuchtbeschreibung -
127	(1984)	MÖLLER, T.J.	Eulerian Current Measurements from the North East Atlantic - March 1982 - October 1983 - A Data Report -
128	(1984)	WOODS, J.D.	The Warmwatersphere of the Northeast Atlantic - A Miscellany -
128	(1987)	WOODS, J.D.	The Warmwatersphere of the Northeast Atlantic - A Miscellany - (second, expanded edition)
129	(1984)	FINKE, M.	Messungen zum Widerstandsbeiwert von Verankerungskomponenten
130	(1984)	GERLACH, S.A.	Oxygen Depletion 1980 - 1983 in Coastal Waters of the Federal Republic of Germany. First Report of the Working Group "Eutrophication of the North Sea and the Baltic"
131	(1984)	ASMUS, R.	Benthische und pelagische Primäproduktion und Nährsalzbilanz Eine Freilanduntersuchung im Watt der Nordsee
132	(1984)	BAUER, J., WOODS, J.D.	Isopycnic Atlas of the North Atlantic Ocean - monthly mean maps and sections -
133	(1984)	KNOLL, M.	Feinstrukturen in der jahreszeitlichen Sprungschicht im JASIN-Gebiet
134	(1984)	FAHRBACH, E., KRAUSS, W., MEINCKE, J., SY, A.	Nordostatlantik '83 - Data Report -
135	(1984)	SAURE, G.	Verhalten der Freifallprofilsonde FPS
136	(1984)	FIEDLER, M., TEMMING, A., WEIGELT, M.	Eine Analyse der fischereibiologischen und fischereilichen Verhältnisse in einem für die Ölförderung genutzten Offshore-Bereich des deutschen Ostseegebietes
137	(1985)	BÖNING, C.	Eine Untersuchung der Dynamik der windgetriebenen ozeanischen Zirkulation mit einem wirbelauflösenden barotropen Modell
138	(1985)	WEIGELT, M.	Auswirkungen des Sauerstoffmangels 1981 auf Makrozoobenthos und Bodenfische in der Kieler Bucht
139	(1985)	BREITENBACH, J., ZENK, W., DASCH, W., WITTSTOCK, R.-R., SCHLOSSER, P.	A compilation of hydrographic data from the Canary Basin, October to November 1983
140	(1985)	LENZ, J., SCHNEIDER, G., ELBRÄCHTER, M., FRITSCHE, P., JOHANNSEN, H., WEISSE, T.	Hydrographic, chemical, and planktological data from the North-West-African upwelling area, obtained from february to april 1983 (OSTATLANTIC-BIOZIRKEL)
141	(1985)	OSTERROHT, C., WENCK, A., KREMLING, K., GOCKE, K.	Chemical planktological and microbiological investigations at an anchor station in Kiel Bight during 1981/82

142	(1985)	ENNENGA, U.	Objektive Analyse aktueller Wind- und Druckfelder über dem Nordatlantik
143	(1985)	BAUER, J., FISCHER, J., LEACH, H., WOODS, J.D.	SEA ROVER Data Report I - North Atlantic Summer 1981 - NOA '81 -
144	(1985)	WEISSE, Th.	Die Biomasse und Stoffwechselaktivität des Mikro- und Mesozooplanktons in der Ostsee
145	(1985)	NIESSLBECK, P., VOIGT, M., KIM, S.J., BOLMS, G., HOPPE, H.-G.	Auswirkungen von Salzgehalts- und Temperaturänderungen auf die Extrazelluläre Enzymaktivität marin-pelagischer Mikroorganismen
146	(1985)	FAHRBACH, E., KRAUSS, W., MEINCKE, J., SY, A.	Nordatlantik '84 - Data Report -
147	(1985)	PAULY, D.	Zur Fischereibiologie tropischer Nutztiere - Eine Bestandsaufnahme von Konzepten und Methoden -
148	(1985)	BABENERD, B., ZEITZSCHEL, B.	Trends für eintragsrelevante Faktoren und für die Nährsalzkonzentrationen im Wasser der Kieler Bucht - Ein Beitrag zur Erforschung der Eutrophierung der Nord- und Ostsee -
149	(1986)	BREY, T., PAULY, D.	Electronic Length Frequency Analysis - A User's Guide to ELEFAN 0, 1 AND 2 (Revised and Expanded Version)
150	(1985)	LIPPERT, A.	Erzeugung niederfrequenter ozeanischer Variabilität durch fluktuierende Windfelder
151	(1986)	ZARKESCHWARI, N.	Fische als Fischräuber, dargestellt an der Nahrung demersaler Fische der Nordsee
152	(1986)	STIENEN, Ch.	Die Phytoplanktonentwicklung in Abhängigkeit von der Nährsalzkonzentration Ein Vergleich zwischen Kieler Förde und Kieler Bucht
153	(1986)	BAUER, E.	Isopyknische und diapyknische Ausbreitungsvorgänge im tropischen und subtropischen Nordatlantik
154	(1986)	AMBAR, I. et al. (TOPOGULF GROUP)	TOPOGULF - A joint programme initiated by IFREMER, Brest (France) - IFM, Kiel (W.Germany) - Data Report -
155	(1986)	DICKE, M.	Vertikale Austauschkoeffizienten und Porenwasserfluß an der Sediment/Wasser-Grenzfläche
156	(1986)	ONKEN, R.	Numerische Simulation der Erzeugung und Instabilität mesoskaliger Fronten Numerical Simulation of the Generation and Instability of Mesoscale Fronts
157	(1986)	WENZEL, M.K.CH.	Die mittlere Zirkulation des Nordatlantik auf der Grundlage klimatologischer hydrographischer Daten
158	(1986)	BARTHEL, K.-G.	Die Stellung dominanter Copepoden-Arten im Nahrungsgefüge typischer Wasserkörper der Grönland-See
159	(1986)	WOBBER, Ch.	Ein numerisches Modell zur Untersuchung barokliner Rossby-Wellen im Nordatlantik
160	(1987)	ISEMER, H.-J.	Optimierte Parametrisierungen der klimatologischen Energie- und Impulsflüsse an der Oberfläche des Nordatlantik
160a	(1987)	ISEMER, H.-J.	The Bunker Climate Atlas of the North Atlantic Ocean - a technical description of the data tape -
161	(1987)	SCHLOSSEL, P.	Infrarotfernerkundung von Oberflächentemperaturen sowie atmosphärischen Temperatur- und Wasserdampfstrukturen
162	(1987)	VIEHOFF, Th.	Bestimmung mesoskaliger Variabilitäten der Oberflächentemperatur und der Attenuation im Nordatlantik aus Satellitenmessungen
163	(1986)	KILS, U.	Verhaltensphysiologische Untersuchungen an pelagischen Schwärmen Schwarmbildung als Strategie zur Orientierung in Umwelt-Gradienten Bedeutung der Schwarmbildung in der Aquakultur
164	(1987)	FISCHER, J.	Struktur und Dynamik einer mesoskaligen Front im Wirbelfeld des Nordatlantischen Stromes
165	(1987)	STAMMER, D. WOODS, J.D.	Isopycnic Potential Vorticity Atlas of the North Atlantic Ocean - monthly mean maps -
166	(1987)	MOLLER, T.J., FINKE, M., DASCH, W., WITTSTOCK, R.-R.	Hydrographic and current measurements in the North-East Atlantic Ocean Data Report F.S. Meteor Cruises 69/5 and 69/6 October to November 1984
167	(1987)	BECKMANN, A.	Die Modellierung mesoskaliger quasigeostrophischer Instabilität
168	(1987)	ROLKE, M.	Ein Verfahren zur Auswertung von Zooplanktonfeldproben mittels der quantitativen automatischen Bildanalyse am Beispiel von Material der "Meteor-Äquatorexpedition 1979"

169	(1987)	STEGMANN, P.M.	Untersuchungen zur Varibilität der sonnenlichtangeregten Fluoreszenz von Phytoplankton in der Ostsee im Hinblick auf Fernerkundung
170	(1987)	MOLLER, T.J.	Analyse niederfrequenter Strömungsschwankungen im Nordostatlantik
171	(1987)	BARKMANN, W.	Der Einfluß der Wärmebilanz auf die Struktur der saisonalen Grenzschicht
172	(1988)	FINKE, M.	Zirkulation und Rossbywellen im Kanarenbecken
173	(1987)	SIEDLER, G. SCHMICKLER, H. MOLLER, T.J. SCHENKE, H.W. ZENK, W.	Forschungsschiff METEOR, Reise Nr. 4 Kapverden-Expedition, Oktober - Dezember 1986
174	(1987)	SCHNEIDER, G. LENZ, J.	Die Bedeutung der Größenstruktur und des Stoffumsatzes des Zooplanktons für den Energietransfer im pelagischen Ökosystem der Auftriebsregion vor NW-Afrika
175	(1987)	LEACH, H. DIDDEN, N. FIEKAS, V. FISCHER, F. HORCH, A. WOODS, J.	SEA ROVER Data Report II - North Atlantic Summer 1983 - NOA '83 -
176	(1987)	WEIGELT, M.	Auswirkungen von Sauerstoffmangel auf die Bodenfauna der Kieler Bucht
177	(1988)	BREY, TH. SORIANO, M. PAULY, D.	Electronic length frequency analysis. A rivised and expanded user's guide to elefan 0, 1 and 2 (2nd Edition)
178	(1988)	HALBEISEN, H.-W.† In der Überarbeitung von SCHÖFER, W.	Bestimmungsschlüssel für Fischlarven der Nordsee und angrenzender Gebiete
179	(1988)	GERDES, R.	Die Rolle der Dichtediffusion in numerischen Modellen der nordatlantischen Zirkulation
180	(1988)	LENZ, J. SCHNEIDER, G. EL WAG, A.G.D. GRADINGER, R. FRITSCHE, P. MOIGIS, A. PILLEN, T. ROLKE, M. WEISSE, T.	Planktological data from the central Red Sea and the Gulf of Aden (R.V. "Meteor", cruise No. 5/2, January - March 1987)
181	(1988)	SIEDLER, G. BLÖBAUM, H KOY, U. MEYER, P. ZENK, W. ZWIERZ, M.	Schwankungen des Wärmeinhalts der Warmwassersphäre im Nordatlantik, Meßprogramm 1984 - 1986
182	(1988)	HÖTTEL, M.	Zur Bedeutung der Macrofauna für die Nährsalzprofile im Wattsediment
183	(1988)	ABELE, D.	Carotinoide als biogene Marker für benthische Makroalgen im Sediment der Kieler Bucht
184	(1988)	MOLLER, T.J. SIEDLER, G. ZENK, W.	Forschungsschiff METEOR Reise Nr. 6. ATLANTIK 87/88, Fahrtabschnitte Nr. 1 - 3, Oktober - Dezember 1987
185	(1988)	BUCHHOLZ, F.	Zur Lebensweise des antarktischen und des nordischen Krills, Euphausia superba und Meganyctiphanes norvegica.
186	(1988)	BREY, TH.	Der EinfluB physikalischer und biologischer Faktoren auf Struktur und Dynamik der Sublitoralen Macoma-Gemeinschaft der Kieler Bucht.
187	(1989)	STRASS, V.	Physikalisch kontrollierte saisonale und horizontale Variabilität von Chlorphyllprofilen. - Ergebnisse hydrographisch-optischer Schnitte zwischen den Azoren und Grönland.
188	(1989)	ABTEILUNG MARINE MIKROBIOLOGIE INSTITUT FÜR MEERESKUNDE	Forschungen der Abteilung Marine Mikrobiologie des Instituts für Meereskunde an der Universität Kiel 1964 - 1989
189	(1989)	TEMMING, A.	Biologie und Populationsdynamik der Kliesche (Limanda limanda L.) in der Ostsee
190	(1989)	HACKE, G.	Ableitung der Bodenalbedo aus METEOSAT-Daten
191	(1990)	SICH, H.	Die benthische Ciliatenfauna bei Gabelsflach (Kieler Bucht) und deren Beeinflussung durch Bakterien - Eine Studie über Menge, Biomasse, Produktion, Bakterieningestion und Ultrastruktur von Mikroorganismen -
192	(1990)	PASSOW, U.	Vertikalverteilung und Sedimentation von Phytoplanktonarten in der mittleren Ostsee während des Frühjahres 1986

193 (1990) EVERSBERG, U. Abbau und Akkumulation von organischer Substanz in den Sedimenten der Kieler Bucht

194 (1990) MAROTZKE, J. Instabilities and Multiple Equilibria of the Thermohaline Circulation